

Metal Oxide supported noble metal catalyst:

Powders, Thin films and Nanostructures

Thesis Submitted to AcSIR

For the Award of the Degree of

DOCTOR OF PHILOSOPHY

In

Chemical Sciences



By

Sunil Sekhar A C

Registration Number: 10CC12J26003

Under the Guidance of

Dr. Vinod C Prabhakaran

CSIR- National Chemical Laboratory


Pune- 411008, India

CERTIFICATE

This is to certify that the work incorporated in this Ph.D. thesis entitled “*Metal oxide supported noble metal catalyst: Powders, Thin films and Nanostructures*” submitted by **Mr. Sunil Sekhar A. C.** to Academy of Scientific and Innovative Research (AcSIR) in fulfilment of the requirements for the award of the Degree of *Doctor of Philosophy* in *Chemical Sciences*, embodies original research work under my supervision. I/We further certify that this work has not been submitted to any other University or Institution in part or full for the award of any degree or diploma. Research material obtained from other sources has been duly acknowledged in the thesis. Any text, illustration, table etc., used in the thesis from other sources, have been duly cited and acknowledged.



Research student
Sunil Sekhar A C



Research Guide
(Name & Signature)
Dr. Vinod. C. Prabhakaran

DECLARATION

I hereby declare that the work described in the thesis entitled “*metal oxide supported noble metal catalyst: Powders, Thin films and Nanostructures*” submitted for the degree of *Doctor of Philosophy in Chemical Sciences* to the Academy of Scientific and Innovative Research (AcSIR), New Delhi, has been carried out by me at the Catalysis and Inorganic Chemistry Division, CSIR-National Chemical Laboratory, Pune-411008, India under the supervision of **Dr. Vinod. C. Prabhakaran**. I further declare that the material obtained from other sources has been duly acknowledged in this thesis. The work is original and has not been submitted in part or full by me for any other degree or diploma to this or any other university.

Date: 10th January 2017

CSIR-NCL, Pune



Sunil Sekhar A.C.

Research Student

Acknowledgements

The realization of this thesis work is achieved by the unconditional love and support provided by many of my colleagues, friends, family and well wishers. My experience in CSIR-NCL for the last five years has been nothing short of amazing, especially in our beloved CAT&MOSS family. This lab has given me immense opportunity to explore the scientific world either by scientific thoughts or by amazing me with the top class instrumentation facilities. This thesis is also a result of my experiences with many of the scientific arguments with other fellow researchers. It is one of the happiest moments to acknowledge affectionately to those who made my days fruitful here, without them I would not have come this far to climb the first step of my scientific carrier.

First and foremost I would like to thank my research supervisor Dr. C. P. Vinod. He has been supportive ever since I joined this lab. Without his care and concern I would have never made up to this stage of my research carrier. He acted like a friend, a philosopher and a guide at various times which kept me going during my stay at NCL. And he gave me the moral support and freedom to act upon my will during the most difficult times of research as well as thesis writing. I take this opportunity to show him my deepest sense of gratitude and respect; thank you sir for standing by me and correcting me at each step of my PhD work.

I extend my sincere thanks to the Director of CSIR-NCL Prof. Ashwini Kumar Nangia, Dr. Sourav Pal (former director), Dr. D. Srinivas (Head, Catalysis Division) and Dr. A. P. Singh (former Head, Catalysis Division) for providing me the opportunity to accomplish my research work in this prestigious laboratory. I sincerely thank Dr. C. S. Gopinath, Dr. T. Raja, Dr. Nandini Devi, Dr. Shubhangi Umbarkar and Dr. C.V.V. Satyanarayana for their support and encouragement throughout my PhD work. My DAC member has guided me throughout my PhD tenure with their valuable suggestions and criticisms, which helped me to put up the thesis in the current format. I express my sincere thanks to my DAC members Dr. S. K. Asha, Dr. K. Sreekumar and Dr. K. Krishnamoorthy for their support and care.

I express my heartfelt thanks to Dr. Jean-Philippe Dacquin for his great care and support during my stay at Lille University, France. He has shown faith in me and gave multiple opportunities to work with him during my PhD course. He is the one who kept a sense of humour when I had lost mine during the tough time of my research. I take this opportunity to thankfully acknowledge his tremendous efforts in sharpening my scientific thoughts and

wisdom. And I thank you for giving me the moral support and freedom, which I needed to move on during the difficult time of my PhD course. I extend my wholehearted thanks to Dr. Pascal Granger (LIA co-ordinator) and Dr. Christophe Dujardin for their care and concern during my stay at Lille University.

I thank all other scientific and non-scientific staff of CSIR-NCL and UCCS, Lille University for their help and support in scientific and technical matters during my tenure as a research student. I take this occasion to thank all my teachers, well-wishers, classmates and friends in various stages for their teachings, love, encouragement, kind cooperation and good wishes that I received from them. I have high regards for all my labmates for their support and help during my PhD. course. I thank Dr. Vysakh, Anish, Dr. Sreedhala, Sudheesh, Meera, Jino, Ziyad, Yogita, Shilpa, Vidya, Cygnet, Preeti, Sharad, Dr. Tanmay, Betsy, Aswathy, Kiran, Shoy, Sharath, Leena, Jijil, Dr. Rajesh, Dr. Alson, Dr. Suresh, Jithesh, Govind, Ashok, Anju, Sumantha, Manikandan, Trinadh, Tony, Ruchi, Kshirodra, Laxmiprasad, Atul, Abdelali, Simona and all malayalee and non-malayalee friends for their care and support as a colleague during my PhD tenure.

I do not have words to acknowledge the immense support received from my family; Mom, dad, sister, brother in law and their kids. Their continuing support inspired me to get focused on what I do and helped me to chase my dream throughout my carrier. The support I got from Neethu, my wife who happen to enter into my life during the difficult time of thesis writing, is so much that I could write the thesis in the current format. I sincerely thank her for not discussing the topic honeymoon during my thesis writing stage.

Above all, I owe it all to Almighty God for granting the wisdom, health and belief to undertake research work for my thesis and enabling me to its completion.

Sunil Sekhar A. C

Dedicated to my family

Table of Contents

Chapter 1: Introduction

1.1. Catalysis	2
1.2. Heterogeneous Catalysis	3
1.3. Porous materials as heterogeneous supports	4
1.4. General approaches in porous materials synthesis	5
1.5. Metal nanoparticles as active catalytic sites	6
1.6. Nanostructured catalysis	8
1.6.1. Au-Silica Powders, Nanostructures and Thin film catalysts	8
1.6.2. Pt-Alumina hierarchical nanocatalysts	11
1.7. Environmentally significant catalytic reaction over nanostructured catalysts	12
1.7.1. CO oxidation on Au-silica nanocatalysts	12
1.7.2. Nitrite hydrogenation over hierarchical Pt-alumina nanocatalysts	14
1.8. Instrumentation	15
1.8.1. UV-Visible Spectroscopy	15
1.8.2. X-ray Diffraction	16
1.8.3. N ₂ Porosimetry	17
1.8.4. Raman Spectroscopy	18
1.8.5. Fourier Transformed Infrared Spectroscopy (FTIR)	19
1.8.6. Nuclear Magnetic Resonance Spectroscopy (NMR)	19
1.8.7. Inductively Coupled Plasma Spectroscopy (ICP)	20
1.8.8. Scanning Electron Microscopy (SEM)	20
1.8.9. Transmission Electron Microscopy (TEM)	21
1.8.10. X-ray photoelectron spectroscopy (XPS)	21
1.8.11. Gas Chromatography	22
1.9. Scope and Objective of the thesis work	22
1.10. References	24

Chapter 2: Au-silica powder, core-shell nanostructures and its environmental catalysis

2.1. Introduction	28
2a. Au-mesoSiO ₂ powder catalyst and its CO oxidation Catalysis	32
2a.1. Experimental Methods	32
2a.1a. Synthesis of the catalyst Au-mesoSiO ₂	32
2a.1b. Catalytic Test: CO oxidation reaction	33
2a.2. Results and Discussions	34
2a.2.a. Structural characterisation: UV-Vis and X-ray diffraction analysis	34
2a.2.b. Textural Characterisation: Surface area analysis	35
2a.2.c. Microscopy analysis results: Transmission Electron Microscopy (TEM)	36
2a.3. Catalytic Test results	37

2b. Au@SiO ₂ core shell nanocatalyst and its CO oxidation catalysis	38
2b.1. Experimental Methods	39
2b.1.a. Synthesis of gold nanoparticles by Seed mediated method	39
2b.1.b. Silica encapsulation	39
2b.1.c. Catalytic Test: CO oxidation	40
2b.2 Results and discussions	40
2b.2.a. Structural characterization: UV-Vis and x-ray diffraction analysis	40
2b.2.b. Textural characterisation: Surface area analysis	41
2b.2.c. Microscopy analysis: Scanning and transmission electron microscopy	42
2b.3. Catalytic Test Results: CO oxidation reaction	45
2c. Au@Ti-SiO ₂ core shell nanocatalyst and its CO oxidation catalysis	48
2c.1. Experimental Methods	48
2c.1.a. Synthesis of core shell Au@Ti-SiO ₂ nanocatalysts	48
2c.1.b. Synthesis of gold nanoparticles by Seed mediated method	48
2c.1.c. Silica encapsulation	49
2c.1.d. Modification of silica matrix with Titanium	49
2c.1.e. Catalytic test: CO oxidation	49
2c.2 Results and Discussions	50
2c.2.a. Structural characterization	50
2c.2.b. Textural characterization	57
2c.2.c. Microscopy Analysis	57
2c.3 Catalytic Test Results: CO oxidation reaction	60
2c.4 Spent catalyst analysis	63
2.3 Conclusion	64
2.4 References	66

Chapter 3: Au-mesoSiO₂ thin film model surface for catalytic applications

3.1. Introduction	70
3.2. Raman spectroscopy	71
3.3. Surface Enhanced Raman Scattering (SERS)	72
3.4. Gold mesoporous silica thin film model surfaces as nanocatalysts	73
3.5. Synthesis of Au-mesiSiO ₂ thin film catalysts (GSM-23F)	74
3.5.a. Pre-treatment of the substrate, Si (100)	74
3.5.b. Silica gold sol-gel synthesis	74
3.5.c. Film casting on the hydroxylated Si (100) substrate	74
3.6 Results and Discussions	75
3.6.a. Structural Characterisation	75
3.6.b. Microscopy analysis	76
3.7. Experimental: SERS and catalytic reaction	79
3.8. GSM-23F as a robust SERS substrate	79
3.9. GSM-23F as a catalytically active model surface	80
3.10. Conclusions	84
3.11. References	85

Chapter 4: Engineering the porous architecture of Pt-alumina and its environmental catalysis

4.1. Introduction	88
-------------------	----

4a. Synthesis and Characterisation of mesoporous, macroporous and macro-mesoporous Pt-alumina architecture and the impact of these pore system on the catalytic activity	94
4a.1. Experimental Methods	
4a.1.1. Periodically ordered mesoporous alumina (PMA) synthesis	94
4a.1.2. Macroporous alumina (MA) synthesis	95
4a.1.2.a. Synthesis of monodisperse polystyrene beads (PS-300)	95
4a.1.3. Macroporous-mesoporous alumina (MMA) synthesis	96
4a.2. Pt impregnated meso, macro and macro-mesoporous alumina	96
4a.3. Catalytic test: Nitrite hydrogenation using hydrogen gas as reducing agent	96
4a.4. Results and Discussions	97
4a.4.1. Amorphous alumina (PMA, MA and MMA) support characterisation	97
4a.4.2. 1 wt% Pt supported catalyst (Pt-PMA, Pt-MA and Pt-MMA) characterisation	103
4a.5. Catalytic test results: - Nitrite hydrogenation reaction	105
4b. Impact of soft ageing treatment on the textural properties of alumina and its catalytic activity for the hydrogenation of nitrites on a Pt-alumina catalyst	107
4b.1. Experimental Methods	
4b.1.1. Hierarchical macroporous & macroporous-mesoporous alumina synthesis	107
4b.1.2. Pt impregnation on the hierarchical alumina	108
4b.2. Catalytic test: Nitrite hydrogenation reaction	108
4b.3. Results and Discussions	109
4b.3.1. Hierarchical macroporous alumina (MA-X) synthesised by soft ageing treatment method and its catalytic activity	109
4b.3.2. Hierarchical macroporous-mesoporous alumina (MMA-X) synthesised by soft ageing treatment method and its catalytic activity	118
4.2. Conclusions	121
4.3. References	123
Chapter 5: Summary and Conclusions	126
List of Publications	
Curriculum Vitae	

List of Figures

Figure No	Figure Caption	Page No
1	Representing the catalysed and uncatalysed reaction energy profile depending in the progress of the reaction	3
2	Schematic representation of surface plasmon resonance	16
2a.1	Insitu UV-Vis spectra of gold nanoparticles reduced using P123	35
2a.2	Surface area analysis data for the sample GSM-23 and the bare SiO ₂ support after calcination	36
2a.3	HR-TEM images of the calcined AU@-mesoSiO ₂ nanocatalysts	37
2a.4	CO oxidation activity profile Vs temperature for the catalyst GSM-23 before and after hydrogen pre-treatment	38
2b.1	Liquid state UV-Vis spectral data of the gold colloid, silica encapsulated gold colloid and the wide angle x-ray diffraction of Au@silica sample	41
2b.2	Surface area and pore size distribution analysis profile for the calcined Au@silica core shell nanostructures	42
2b.3	SEM analysis of the core shell nanostructured Au@silica catalysts under different magnifications	42
2b.4	TEM images of the calcined Au@silica core shell nanostructures under various magnifications	43
2b.5	TEM images of the sample after reduction pre-treatment of Au@silica and that of the calcined samples of Au colloid deposited on SBA-15	44
2b.6	CO oxidation reaction profile as a function of temperature	46
2b.7	TEM images of the spent catalysts Au@silica after 3 cycles of CO oxidation and that of Au-SBA-15 after 1 cycle of CO oxidation	47
2c.1	Liquid state UV-Vis spectra (a) of gold nanoparticles synthesised by seed mediated synthesis and subsequent encapsulation (b) wide angle x-ray diffraction pattern if the core shell nanostructures with various "Ti" loading	51
2c.2	Solid state UV-Vis analysis spectra of the various Ti-loaded core shell nanocatalysts after calcination	52
2c.3	FTIR (a) and (b) Raman analysis data of various AST catalysts	52
2c.4	The ²⁹ Si NMR spectra of (a) AST series catalyst with various Ti loading and (b) Au@silica core shell nanostructure without any Ti loading	53
2c.5	Ti 2p XPS analysis profile for the AST series calcined samples	54
2c.6	XPS analysis data (a) O 1s and (b) Si 2p of the calcined AST series catalyst	55
2c.7	Ti 2p XPS spectra of the nanocatalysts AST1 before and after hydrogen pre-treatment	56
2c.8	The surface area (a) and pore size distribution (b) analysis of the calcined AST samples	57
2c.9	TEM analysis of the AST1 calcined sample with various magnifications	58
2c.10	TEM images of the samples AST5 (a and b) and ASt10 (c and d) with various magnifications	59

2c.11	SEM images of the calcined (a) AST1 (b) AST5 and (c) AST10	59
2c.12	The CO oxidation activity profile (a) calcined and (b) reduced AST series catalysts as a function of temperature	61
2c.13	CO oxidation second cycle (a) and (b) N ₂ pre-treated AST1Red and ASt1Cal samples CO oxidation	62
2c.14	Catalytic activity profile for AST1Red for 3 consecutive cycles of CO oxidation	63
2c.15	The (a) Ti(2p) XPS and (b) TEM analysis of the spent catalyst after 3 cycles of CO oxidation	64
2c.16	FTIR of the spent AST series catalyst after 3 cycles of CO oxidation	64
3.1	(a) wide angle x-ray diffraction analysis of the GSM-23F film and (b) solid state UV-Vis spectra of the sample spin coated on an FTO plate	75
3.2	XPS data of the GSM-23F thin film after calcination	76
3.3	SEM images of the thin film GSM-23F on various magnifications	76
3.4	Elemental mapping of the GSM-23F thin film done under scanning electron microscope	77
3.5	HR-TEM images of GSM-23F under various magnifications	78
3.6	SERS spectra of Rhodamine B on GSM-23F thin film and bare silicon substrate	80
3.7	Raman spectra of the organic molecule under consideration using 633 nm laser source, namely PNP and PAP in solid and aqueous form	81
3.8	PNP to PAP conversion on GSM-23F thin film catalyst using NaBH ₄ as the reducing agent monitored using a raman spectrometer with laser source (a) 514 nm and (b) 633 nm	82
3.9	Raman spectral data of 4-aminophenol with Au nanoparticle colloid (CTAB capped 8-12 nm Au NPs) under 633 nm laser source	83
4a.1	TGA of as-synthesised samples (a) and the comparison of the thermal stability of the periodic mesoporous alumina calcined at two temperatures (b)	97
4a.2	Wide angle x-ray diffraction pattern of alumina synthesised by different methods (a) and the small angle XRD of the mesoporous alumina calcined at two different temperatures (b)	99
4a.3	N ₂ adsorption-desorption isotherm of the different types of calcined alumina samples as well as the pore size distribution of (a) PMA-650 and (b) MA-650	99
4a.4	SEM analysis of the polystyrene beads synthesised	101
4a.5	SEM images of MA-650 at different magnifications	102
4a.6	TEM images of the calcined samples PMA-650, MA-650 and MMA-650	103
4a.7	Wide angle x-ray diffraction patterns of the Pt-impregnated samples after calcination at 400 °C and after reduction at 450 °C	104
4a.8	Porosimetry analysis of Pt-impregnated samples after calcination	104

4a.9	The time dependent catalytic activity results for the nitrite reduction reaction using the various Pt supported alumina catalyst	106
4b.1	TGA of the samples made with and without soft ageing treatment (a) and the wide angle XRD analysis of the MA-X samples	109
4b.2	Wide angle XRD pattern of the macroporous alumina after Pt impregnation followed by calcination (a) and reduction at 450 °C (b)	110
4b.3	Surface area analysis of the MA-X samples and the corresponding pore size distribution graph	111
4b.4	Surface area and pore size distribution analysis of the MA-X samples after Pt impregnation and calcination	112
4b.5	SEM images of the MA-X samples	112
4b.6	HR-TEM images of (a) Pt-MA-0-Red and (b) Pt-MA-48-Red samples	114
4b.7	XPS data for the MA-X samples reduced exsitu before the analysis at 450 °C	115
4b.8	TPD profiles for various Pt-alumina samples	116
4b.9	Catalytic activity results of Pt impregnated and reduced macroporous alumina (MA-X) samples	117
4b.10	TGA/DTG analysis of the soft ageing treated and non treated samples (a) and the wide angle XRD pattern of the MMA-X samples (b)	118
4b.11	The wide angle XRD analysis of (a) 1 wt% Pt impregnated, calcined and (b) reduced at 450 °C MMA-X samples	119
4b.12	Surface area and pore size distribution analysis of various Pt-MMA-X samples	119
4b.13	Catalytic test results of various Pt-MMA-X samples at room temperature under 1 bar H ₂ pressure	120

List of Schemes

Scheme No	Scheme caption	Page No
1	Schematic representation of the nitrite hydrogenation over a transition metal catalyst, using hydrogen as the reducing agent	14
2a.1	One pot synthesis of Au@meso-SiO ₂ nanocatalyst	33
4a.1	Periodic mesoporous alumina (PMA) synthesis by evaporation induced self assembly methodology using P123 as the soft template	94
4a.2	Macroporous alumina (MA) synthesis by EISA methodology using polystyrene beads of 300 nm size as the hard template	95
4a.3	Periodic macroporous-mesoporous alumina (MMA) synthesis by EISA methodology using P123 as well as polystyrene beads of 300 nm size in a co-templating strategy	96
4b.1	Evolution of the mesoporous nature in the hierarchical macroporous-mesoporous alumina by varying soft ageing treatment time	113

List of tables

Table No	Table Caption	Page No
4a.1	Physico-chemical properties for various alumina support after calcination at 650 °C	100
4a.2	Physisorption analysis results of the support and Pt impregnated samples after calcination	105
4b.1	Physico-chemical properties of the support (MA-X) as well as Pt impregnated and calcined samples	111
4b.2	Relative surface composition of Pt species on amorphous alumina	115
4b.3	Turnover frequency represented in terms of Pt surface composition and particle size	118

List of Abbreviations

- SEM - Scanning Electron microscopy
- TEM – Transmission Electron Microscopy
- XRD – X-ray Diffraction
- ICP – Inductively Coupled Plasma
- UV-Vis – Ultraviolet-Visible spectroscopy
- GC – Gas Chromatography
- FID – Flame Ionisation Detector
- TCD – Thermal Conductivity Detector
- XPS – X-ray Photoelectron Spectrometry
- BET – Brauner Emmet Teller
- BJH – Barrett Joyner Halenda
- NMR – Nuclear Magnetic Resonance
- TOF – Turn Over Frequency
- SERS – Surface Enhanced Raman Spectroscopy
- SPR – Surface Plasmon Resonance
- TPR – Temperature Programmed Reduction
- TGA – Thermogravimetry Analysis
- PMA – Periodic Mesoporous Alumina
- MMA- Macroporous Mesoporous Alumina
- MA – Macroporous Alumina
- SAT – Soft Ageing treatment Time
- EISA – Evaporation Induced Self Assembly
- PS300 – Polystyrene Spherical beads of 300 nm dime

Chapter.1

Introduction

Introduction

Catalysis and catalytic processes has a long standing history ever since the modern civilization of the mankind. Right from the pharmaceutical industry to petrochemical or fine chemical industry catalysis is applied everywhere. With the latest Paris declaration, curtailing current environmental pollution will largely rely on the work carried out by the catalysis community in the coming years. From dawn to dusk, the common men will handle many of the products which are in the market as a result of the catalytic processes developed, starting from plastic carry bags to automobiles or personal health care products. The first glimpse of catalysis was in the early 19th century when Faraday and Kirchhoff observed the influence of certain chemicals in facilitating the reaction progress though they have not directly under going any changes. Berzelius was the first who coined the word “Catalysis” in 1835, which holds one of the major shares of the current industrial processes. As described by Berzelius, the term catalysis refers to any chemical process which is accelerated by certain substances without undergoing any change by itself. Later, in 1909 Wilhelm Ostwald received Noble prize for explaining the fundamental chemistry behind reaction equilibrium and kinetics of the reactions based on catalysis. Industrial revolution in catalysis happened after the pioneering discovery by Fritz Haber and Carl Bosch for their Haber-Bosch process for ammonia synthesis by spongy iron catalyst (Nobel prize in 1918). Gerhard Ertl was given Nobel Prize in 2007 for unravelling the molecular level details of ammonia synthesis using surface science techniques. A lot of studies in catalysts as well as catalysis has progressed and as a results two major classifications has developed based on the phase with which a reaction is happening, namely Homogenous catalysis and Heterogeneous catalysis. The easy separation and hence recyclability of heterogeneous catalysis is always composed with homogenous catalysis in terms of the conversion, selectivity and atom economy. A wise choice is necessary for the green and sustainable catalysis from the industrial as well as environmental point of view.

1.1 Catalysis:-

A catalyst is believed to alter the energetics of the reaction by altering the transition state of the reaction by providing a less energy path way and thereby leading to meaningful reaction. In terms of the collision theory one can clearly define that a catalyst will increase the number of effective collision among the reactants and hence leads to product formation at the expense of much lesser energy.

For a general reaction, $X + Y \longrightarrow Z$

The transition state and hence product formation can happen in a much lesser energetic state with the help of a suitable catalysts. This is achieved by taking an alternate reaction pathway with a single or multiple transition states, but keeping the overall free energy change of the reaction as same. Further, an excellent catalyst choice could result in the selective formation of the intended product in a multistep reaction. Thus, catalysis can bring down the essential reaction variables to a much environmentally viable scenario where required conversion and selectivity can be easily achieved. It is evident from the reaction energy profile in Figure.1 that the activation energy for an uncatalysed reaction is much higher when compared to a catalysed reaction and there is no change in the overall energy difference between the reactants and product irrespective of the reaction pathway selected.

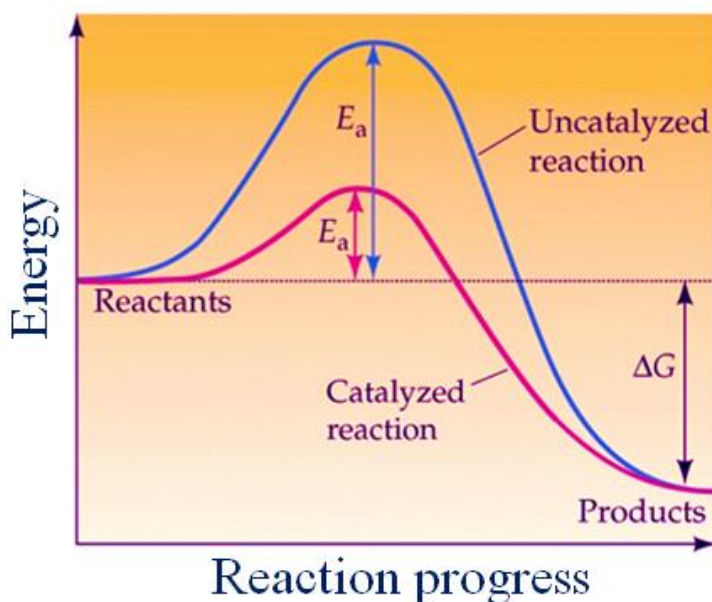


Figure.1 representing the catalysed and uncatalysed reaction energy profile depending on the progress of the reaction.

1.2 Heterogeneous catalysis

The presence of the catalysts in a phase which is different from the reactants during catalysis is referred as the Heterogeneous catalysis. It prevails over homogenous catalysis in its inherent easiness in the catalysts separation as well as the recyclability while the conversion as well as selectivity is compromised in many cases. The heterogeneous catalysis principles are broadly based on the adsorption of the reactants, surface reaction of the adsorbed species on the active catalytic centres and finally desorption of the product from the catalysts surface.

In the supported heterogeneous catalysis, adsorption of the reactant on the solid catalysts can be a Physisorption (only physical interactions like van der Waals interaction with the catalyst surface) or can be Chemisorption (chemical interaction like a co-ordinate bond with the catalyst surface). Chemisorption often leads to dissociative adsorption of the molecules on the active site of the catalyst, yet molecular adsorption is also observed in many cases. In both the above mentioned adsorption process the reactant varies its electronic properties or energetics which is favourable for the reaction to proceed further. The surface reaction after adsorption on the catalyst surface is widely divided into three categories,

- (a) Langmuir-Hinshelwood mechanism:- the reactants separately adsorb on the active catalytic sites, react with each other and finally the product is desorbed
- (b) Eley-Rideal mechanism:- One of the reactants adsorbs on the catalytic site, the other reactant reacts with the adsorbed species and then product desorbs from the surface
- (c) Mars-Van Krevelen (MVK) mechanism:- both the reactants adsorb on the surface, one of the reactant forms an excited precursor complex with the surface and is mobile. It will then migrate to the other adsorbed reactant through the catalyst surface, reacts and finally product desorbs from the surface leaving the catalytic site intact.

In heterogeneous catalysis the active catalytic sites are atoms or exposed facets where the actual reaction occurs. More over the active phase will be normally supported on a high surface area support to make it economic as well as sustainable by imparting added stability to the active catalytic sites. The dispersion of these catalytic sites on the support is considered to be one of the prime attribute in heterogeneous catalysis to impart its effectiveness in catalysing chemical reactions. High surface area porous materials like silica, alumina, etc find its application in heterogeneous catalysis in this respect. Often these supports play a vital role in stabilising the active phase for catalysis or by uplifting the catalytic property by strong metal support interaction (SMSI). Many a times the heterogeneous catalysis is the supported catalysis itself since active metallic phase will be deposited on a solid support.

1.3 Porous materials as Heterogeneous supports

By definition a porous material is a solid material having interconnected voids, which can be filled using a gas or liquid. Based on the nature of the pores, the materials are broadly classified into two,

- (a) Open porous :- open and connect to the outside surface

(b) Closed porous :- internally closed, isolated from the outside surface

These kinds of porosity generally lead to larger surface area as well as lesser density for the materials. The open porosity can greatly influence the behaviour of the materials during catalysis, adsorption, separation etc where as the closed pores are beneficial to generate less dense structural modules or thermally insulating materials. Further, IUPAC¹ had classified the open porous materials into three category based on their pore sizes,

(a) Microporous materials :- Pore size less than 2 nm

(b) Mesoporous materials :- Pore size ranging from 2 to 50 nm

(c) Macroporous materials :- Pore size above 50 nm

These porous materials can be ordered or disordered in nature. The ordered mesoporous materials have their pore channels arranged but their atomic arrangements are not ordered. Whereas, in the case of disordered mesoporous materials neither pore channels nor the atomic arrangements are ordered. The inherent large surface areas and pore volume associated with the mesoporous materials make them as an ideal choice for supporting the active phase in heterogeneous catalysis. This application started when MOBIL corporation was able to make ordered mesoporous material MCM-41 followed by SBA-15 from University of California, Santa Barbara. The ordered porous nature of these materials provides large surface area for the silica materials with better mesopore size and pore wall thickness, ideal for supporting smaller metallic species (metal nanoparticles) for catalytic applications. Similarly, other mesoporous materials like alumina, titania, ceria, etc has also been extensively used as catalyst supports owing to their pore properties as well as metal support interactions.

1.4. General approaches in porous material synthesis

Templating approach is one of the widely used methodologies in generating mesoporosity in materials.²⁻³ A template is defined as the structure directing agent which decides the pore architecture of the resulting porous oxide materials by allowing it to grow in a predefined fashion. These templates are generally divided into two categories, soft template and hard template based on the way in which they allow the inorganic precursor to grow around. The soft templates always have polar head group and a nonpolar tail which preferentially allow them to self assemble to form micelles under the synthesis conditions. These can be cationic, anionic or neutral. In the case of soft templating strategy, the inorganic precursor will grow around the micellar assembly under suitable conditions of temperature and pH, and on

calcination these micelles will be removed leaving behind the well defined micellar void in the resultant materials. In the case of hard templating approach, the inorganic precursor will grow within the void of the hard template (like porous silica, polymer beads etc) and once the template is removed by suitable methods, a replica of the pore system present in the hard templates will remain with the inorganic oxide materials. A co-operative assembly of soft and hard templating strategy is also envisaged as a tool for introducing pore characteristics of different dimensions.⁴ This kind of meso-macroporous assembly will ultimately enhance the diffusion properties when it comes to liquid phase catalysis, specifically where diffusion limitations play a crucial role in influencing catalysis.

The traditional methodologies used for the synthesis of porous materials can broadly be classified as

- (a) Sol-Gel synthesis⁵⁻⁷
- (b) Evaporation Induced Self Assembly (EISA)⁸⁻⁹ coupled with templating strategy^{4, 10}
- (c) Co-precipitation method¹¹
- (d) Solution combustion method¹²⁻¹³
- (e) Hydrothermal method¹⁴⁻¹⁵

In all these methodologies sol-gel and EISA methods are widely practiced because of its simplicity and easy operational conditions. In the sol-gel methodology the inorganic precursor is first hydrolysed by acidic or basic medium in presence of a suitable surfactant followed by the condensation of hydrolysed species. After the desired ageing time for the complete condensation or growth of the inorganic oxide matrix, high temperature treatment is carried to remove the surfactant, generate pores as well as for creating pure phase of the inorganic oxides. In the case of EISA strategy, the initial concentration of the template will be less than the critical micellisation concentration of the template, over a period of slow evaporation of the solvent the micellisation starts along with the acid or base catalysed hydrolysis of the inorganic precursor. Finally the condensed inorganic matrix will be subjected to high temperature treatment to remove the template as well as to generate the porosity.

1.5 Metal nanoparticles as the active catalytic sites

In heterogeneous catalysis metal nanoparticles are considered as the active centres in many of the oxidation, hydrogenation and organic transformation reactions. The variable oxidation

state and vacant d-orbital make the transition metals as the better choice as active sites in homogenous as well as heterogeneous catalysis. When it comes to the case of supported heterogeneous catalysis, metal nanoparticles in the zero valent state prevails in its catalytic activity; specifically when it comes in the case of hydrogenation as well as oxidation catalysis even though a change in oxidation state during the catalysis can be anticipated in many cases. Further, the drastic change in properties when the size diminishes into nano regime makes them ideal system in nanocatalysts where one can precisely tune the size and shape of the nanoparticles by chemical methods. When these nanoparticles are in the colloidal form, the nanocatalysis resembles more like homogeneous catalysis, where as when these nanoparticles are in the solid form (supported on another solid material) it actually becomes heterogeneous and the catalysis turns out to be heterogeneous catalysis. In physical terms, the extent of delocalisation of electrons mainly depends on the size of any system, and hence a dramatic change in physical and chemical properties will result when the size falls into nano regime.¹⁶ Hence, the surface reactivity of these nanoparticles is directly dependent on their size. As mentioned earlier catalysis involves the surface reactivity of the active catalytic site and thus the size of the metal nanoparticles is directly related to its catalytic property. Accordingly, quantum size effect will come into action leading to the variable intrinsic property of the nanoparticles. If support is also in the nano form, then the overall property of the catalyst can be tuned in a desired manner for heterogeneous catalysis which renders added conversion and selectivity control for a particular reaction. Similarly, the exposed crystal facets are also argued to be a crucial part in nanocatalysis like the increased number of under co-ordinated atom in smaller size particles.¹⁷ The different surface energy of these exposed facets could possibly alter the mode of surface adsorption of the reactants and the desorption of the product from the surface of the active site, both of them are considered to be the back bone of heterogeneous catalysis concepts.

The number of under co-ordinated atoms is considered as the catalytic hot spots in these nanoparticles, and the formation of which depends mainly on the size of the metal nanoparticles. Further, the atoms at the edges and corners are more reactive than those at the planes; whose number also increases with decreasing particle size. A control over metal nanoparticle size is a must in heterogeneous catalysis in order to deliver appreciable reactivity; hence a lot of studies are directed towards the synthesis of monodisperse metal nanoparticles in the past. Two fundamental schools of thoughts in metal nanoparticle synthesis is the bottom up approach and the top down approach. In the bottom up approach,

colloidal metal nanoparticles are synthesised starting from the precursor and generally by chemical methods, whereas in the top down approach the bulk material is sliced into nano regime preferably by physical methods. Thus, in the colloidal synthesis chemistry a stabilising agent/capping agent is generally used to control the specific size and shape of the nanoparticles. Many a time this capping agent could effectively tune the surface property of the nanoparticles and thus substantially tune the catalytic property in colloidal nanocatalysis. In the following section a brief introduction about nanocatalysis, especially catalysis by supported Au and Pt nanoparticles which has received a lot of attention in this area is presented.

1.6 Nanostructured catalysis

Supported nanoparticles with well defined shape as well as falling in the nano meter regime can be actually referred to be nanostructured catalysts and the catalysis nanocatalysis. The specific size and shape of the overall catalyst is designed by keeping the catalytic properties required under a specific set of experimental conditions. Some of the nano structures which are widely used in heterogeneous catalysis are Core-shell, Yolk-shell, hollow spheres, nanoporous, periodically ordered and hierarchically ordered amorphous supports. Out of which core-shell and yolk shell are ideal for high temperature reactions since these can avoid the thermal sintering of the core nanoparticles one of the prime reasons for catalyst deactivation. In the case of yolk shell catalysts, the active core near to one side of the shell can improve the catalytic activity by its easy access. The pore systems can result in better selectivity for multistep multicomponent reactions.

1.6.1 Au-silica powder, nanostructured and thin film catalysts

Gold catalysis is undoubtedly an area that has taken the homogeneous and heterogeneous catalytic arena by surprise. Significance of the size and shape dependency of metal nanoparticles as explained above is profound in the case of gold catalysis. The initial interest in gold catalysis was the efforts to understand how a inert bulk material can very efficiently catalyse many of the chemical reactions of industrial and environmental significance under ambient conditions. This has led to high degree of understanding of gold catalysis in the past few decades, thanks to the surface science and modern insitu experimental tools in unravelling molecular level details of heterogeneous catalytic process on this material.¹⁸ In heterogeneous gold catalysis the role of the support is mainly to support the active gold nanoparticles on the surface so that coalescence and growth of larger nanoparticles can be

avoided during the synthesis as well as catalysis. Another important factor contributing towards the selection of an ideal support is the large surface area, tunable pore size and adequate pore volume in addition to the easy availability and economic viability to use in heterogeneous catalysis. Silica, being its easy availability, large surface area with tunable surface property, greater mechanical and thermal stability is considered as an ideal support for many of the heterogeneous catalytic reactions. For gold catalysis, it is well documented in literature that the size dependency as well as thermal sintering is very high when gold nanoparticles are supported on inert supports like silica and alumina owing to their poor metal support interaction.¹⁹ Thus, the synthesis as well as the stabilisation of monodisperse gold nanoparticle on these inert supports is still a challenge for the catalysis fraternity. There are a number of conventional methods in which gold can be supported on solid supports, which preferably have large surface area with interconnected and ordered pore networks. Among which, impregnation or adsorption of the metal precursor is the widely adopted conventional method for supporting gold nanoparticles on the solid supports like silica, alumina etc. The aqueous phase adsorption of the Au using the widely used hydrophilic precursor HAuCl_4 is highly pH dependent as pH of the medium can play a vital role in deciding the surface charge of the support used and hence interfere with adsorption of AuCl_4^- . Under such a situation the exchange of the chloride ions with that of the hydroxyl ions are equally important for the better dispersion of Au (III) species on the support surface. According to thermodynamic calculations of reaction equilibria, the $\text{Au}(\text{OH})_3$ formed is reported to precipitate during the HAuCl_4 hydrolysis if the pH is above 9.²⁰ Thus pH of the medium is a crucial factor in the impregnation of Au (III) species on a solid support and is predicted that the size increases from 5-25 nm if the pH increases from 4-9 based on few initial reports.²¹⁻²² Further, extensive washing and reduction under hydrogen atmosphere at high temperature is expected to remove the remnant chloride ions after impregnation, which is believed to improve the catalytic activity of the gold nanoparticles. Another widely adapted mechanism is the deposition-precipitation method²³ which first reported by Haruta et al for gold nanoparticles on mesoporous supports. Here insoluble $\text{Au}(\text{OH})_3$ is precipitated by varying the pH and hence deposited on the support. According to Haruta, the nucleation as well as the precipitation of these $\text{Au}(\text{OH})_3$ species solely happens on the defect sites on the mesoporous solid support. The major difference between adsorption/impregnation and deposition-precipitation method is the lesser mobility of Au nanoparticles during the heat treatment step due to decreased percentage of chloride ions on the support surface. Even though these colloidal methods limit the size of the metal nanoparticles, heterogenizing on a

solid support develops some more challenge in the stability of these nanoparticles. Especially on a silica support these gold nanoparticles are prone to undergo thermal sintering during the colloidal deposition or the actual catalytic cycles. It has been observed and reported in the past that the active small gold nanoparticles or clusters easily undergo coarsening due to its very low Tammann temperature ($395\text{ }^{\circ}\text{C}$)²⁴, which limits the application of these catalysts to lower temperature regime for size sensitive catalytic reactions.²⁵ Further, exothermicity of certain reactions like CO oxidation developed enhanced local heating during catalysis, leading to poor recyclability associated with the sintering. Yet, DFT calculations made by Dudney et al reports the stability of gold nanocluster on a defective silica surface just like that of on reducible TiO_2 support pointing towards the significance of Au-Silica catalyst as an active and sustainable catalyst.²⁶ Surfactant mediated chemical synthesis methodologies helped the chemist in making size and shape specific gold nanoparticles in colloidal form and thus the next gold supporting strategy is the deposition of the preformed nanoparticles on the solid supports. This methodology will limit the size of the nanoparticles and restricts its migration while synthesis as well as catalytic reactions. Materials with ordered mesoporous channels like SBA-15 and MCM-41 has been extensively used for these purpose since the void space they provide can accommodate active metal nanoparticles of variable dimensions.²⁷ Because of the weaker interaction of Au^{3+} with the silica surface, surface functionalisation is identified as the best protocol to effectively entrap these cationic species within the voids. A subsequent reduction treatment will result in the formation of metallic gold nanoparticles.²⁸ Still, these entrapped nanoparticles can also undergo thermal sintering many a times under harsh reaction conditions on a mesoporous silica support leading to poor catalytic recyclability. Encapsulated nonmaterials has emerged as the ideal choice under these circumstances since it can avoid the problems associated with the thermal sintering of the gold nanoparticles at high temperature as well as the metal leaching in the liquid phase catalysis. A metal nanoparticle core which is accessible through mesoporous shell can thus provide sinter resistance to the active catalytic phase hence this kind of encapsulation strategy finds its own significant place in modern material synthesis pedagogy.²⁹⁻³¹ Various architectures like core shell, yolk shell, hollow porous nanostructures has emerged as the best catalytic support in this respect. Plenty of literature represents their significance in catalysis not only in supporting Au but other transition metals like Pt, Pd, Ru, Rh etc. In this methodology, the efforts are limited where bifunctionality of certain surfactants like Pluronic P123 or cetyl trimethylammonium bromide (CTAB) as the capping agent for the colloidal nanoparticle synthesis as well as the structure directing agent for the support synthesis. This

gives the advantage of limiting the number of variable in fine tuning the synthesis protocol. Mesoporous thin films with accessible pore channels for the incorporation active catalytic sites as well as for the easy diffusion of reactants and products make them as attractive choice for making composite thin films for catalytic applications.³²⁻³⁴ Further, the thin film model surface of this category has emerged in the late 1990's as a direct approach towards understanding the mechanism of many of the catalytic reactions using surface science tools. The single crystal studies could pave the road towards a better understanding of the catalytic mechanism via identifying the mode of adsorption, the nature of the surface species during catalysis, the active site for catalysis etc.³⁵⁻³⁷ Yet, there was huge material gap since many of these studies using single crystals actually do not represent a real catalyst and hence the conclusions drawn out from these studies may not be necessarily accurate. Thus making composite thin films which could mimic the surface properties of a single crystal along with the chemical nature of a composite real catalyst could potentially reduce this material gap. Scientific community has made progress towards this direction in the last few decades utilising the surface science studies under operando conditions.³⁸⁻³⁹ The major challenge in making these kinds of composite thin films is the orientation of the pore channels in a direction which is accessible to the reactants so that diffusion limitation can be avoided as well as it can be directly probed under operand conditions. These kinds of studies specifically probing the interface where the actual catalysis happens are expected to reveal the misery behind many of the catalytic reactions which has not been completely understood.

1.6.2. Pt-alumina hierarchical nanocatalysts

The higher thermal stability as well as dominant crystalline phase with tunable pore size and surface area makes alumina a prominent support for heterogeneous catalysis. The industrial significance of alumina is widely recognized in the automobile and petrochemical industry as catalysts as well as catalyst supports. For example, γ -alumina is used as a support for Ni or Co nanoparticles in the hydrodesulphurization⁴⁰ (HDS) reaction industrially. The presence of mesoporosity is identified as a pre-request for catalytic application in alumina as in the case of silica, and hence a lot of efforts have been directed towards the synthesis of alumina with tunable porosity over different length scale. The creation of mesoporosity or interconnected porosity is theoretically expected to reduce the heat and mass transfer limitations associated with heterogeneous catalysis. Among the various conventionally used methodologies, surfactant templating coupled with sol-gel or hydrothermal methodology is visualized as a promising tool for the development of tailor made porous alumina.⁴¹ Evaporation induced

self assembly strategy is successful in the synthesis of ordered mesoporosity in alumina when coupled with surfactant templating as reported by many groups.⁴² In the synthesis of these materials, the most crucial step is the control over the hydrolysis/condensation rate of the inorganic alkoxide precursor under the synthesis conditions. For this reason it is necessary to have a strong affinity between the precursor ensemble and the template used, which could potentially result in the formation of ordered meso or macrostructure base on the template used. Up on removal of the template after the nucleation and growth of the inorganic oxides, open porosity is generated in the material.

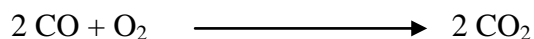
Porous alumina has been widely utilised as a heterogeneous supports for various metal nanoparticles in catalysis owing its large surface area and pore size distribution. Ni nanoparticle deposited on mesoporous alumina has previously been reported for its ability to partially oxidise methane to synthesis gas⁴³ and many other reports.⁴⁴⁻⁴⁵ Likewise, Pd nanoparticle supported alumina has been extensively studied for its various catalytic applications⁴⁶⁻⁴⁸ as well as for its better metal support interaction in a Pd only three way catalytic convertor system.⁴⁹ Number of other catalytically active metal nanoparticles like Ru⁵⁰⁻⁵¹, Au⁵²⁻⁵³ etc are deposited on alumina and tested for its applicability as heterogeneous catalysts. Pt being low cost when compared the above mentioned noble metal nanoparticles are widely used as an active phase for hydrogenation reaction owing to its inherent hydride formation ability under catalytically relevant conditions. A number of reports are available in literature regarding the various techniques used to deposit the Pt nanoparticles over alumina with good dispersion, stability, metal support interaction and catalytic applicability⁵⁴⁻⁵⁸ indicating the promising application of this system in heterogeneous catalysis.

1.7 Environmentally significant catalytic reaction over nanostructured catalysts

1.7.1. CO Oxidation on a Au-Silica nanocatalyst

The toxic nature of carbon monoxide evolving from the chemical industry as well as automobile exhaust prompted the scientist to develop technologies to reduce CO pollution. Once inhaled the CO will limit the oxygen carrying capacity of haemoglobin by converting it into carboxyhaemoglobin in human body hence creates serious health hazards. The presence of CO in the atmosphere indirectly enhances the green house effect by consuming hydroxyl radical present in the atmosphere which generally acts as a troposphere detergent in removing methane from atmosphere. Though the reaction is chemically not so challenging from the point of a view of the number of reacting components involved or the number of possible

products formed, this fundamental reaction puzzled the catalytic community in gold based catalysts for a long time.



This particular reaction needs three bodies to interact under a certain specific thermodynamic and kinetic conditions to proceed smoothly in the forward direction and thus catalyst has to be tailor made to effectively perform catalysis. It has been reported by Haruta et al⁵⁹ in their initial studies that the optimum size range for an active gold catalyst for CO oxidation is with a gold particle size between 3-5 nm. Simultaneously Goodman et al⁶⁰ identified the electronic variation within the same nanoparticles at the edges and corners using Scanning Tunnelling microscopic analysis (STM). The under co-ordinated atoms at the edges and corners with variable surface energy is considered as the active sites for catalysis. At the same time the metal support interaction is also given equal credits for this environmentally significant CO oxidation on gold based heterogeneous catalysts. Since the rate determining step identified for this reaction is the oxygen dissociation and it is well known that the oxygen sticking coefficient is negligible on a gold surface, the basic question was where is oxygen getting activated and how? Thus based on the catalytic activity observed, the support has been categorised into two, active (helps in oxygen activation/dissociation, TiO₂, MgO as examples) and inert (not helping in oxygen dissociation, SiO₂, Al₂O₃ as examples).⁶¹ Later, Behm et al⁶² provided a reasonable explanation with experimental proof regarding the oxygen activation on various supports and he stabilised the concept of perimeter interface for oxygen activation which first put forward by Haruta and co-workers. Silica is being considered as the least active support since it cannot activate molecular oxygen under ambient conditions though it is having large surface area and tenable pore size, an essential criterion for any heterogeneous support. In addition to that the early synthesis protocols overlooked the stability of the gold nanoparticles on the silica support owing to the weak interaction between silica surface and the gold precursor under the synthesis conditions. This finally leads to sintering of the gold nanoparticles either during synthesis or catalysis limiting the catalytic life cycle.

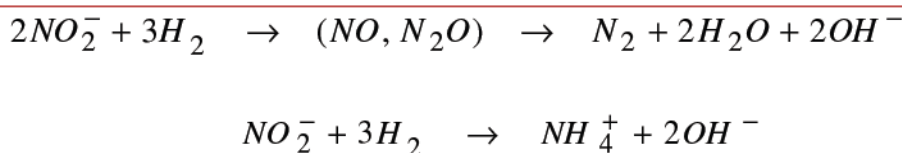
Further, the size dependency also should be revisited with the help of modern characterisation tools to firmly establish the size dependency as the sole reason on to which catalytic activity depends. The ease of availability and synthesis conditions make mesoporous silica an attractive support. In addition to that specific control over the overall geometry of the catalyst

can also play a vital role since under the nanometre size regime even silica can also show different surface property. As mentioned previously the sintering can be limited by encapsulating the active metal inside a porous shell as practiced by many in the recent past.²⁹⁻

³¹ Finally incorporating an active support like TiO₂ on a gold-silica system could potentially enhance the activity towards the CO oxidation and such a study could potentially tell the influence of gold nanoparticle size in the overall catalytic activity of the catalyst.

1.7.2. Nitrite hydrogenation over hierarchical Pt-alumina nanocatalysts

Nitrate and nitrite contamination in the ground water as well as the surface water is one of the major environmental problems in many of the countries. Industries working on oil refining, milk related products, fertiliser manufacturing, fibre processing units etc are expected to expel nitrogen containing effluents as an industrial waist. The water solubility and the higher stability of these ions cause potential challenges in front of the research community in waste water treatment. The ingestion of nitrites has serious health issues beyond specific limits, especially in infants. According to the World Health Organisations (WHO) report in 2012, the allowed level of nitrites in drinking water is only 3 mg/L, this recommendation points to the serious health issues related to the ingestion of nitrites in human beings. The stringent environmental protection rule in the modern world has resulted in the development of a number of treatment technologies namely, biological denitrification, reverse osmosis, ion exchange method and chemical reduction method for the denitrification of surface as well as ground water. Each of the above mentioned methods has its own limitation related to its applicability and recyclability. Yet, chemical reduction method posses' advantages like easier operational control, higher conversion rate and the absence of any secondary pollutant.



Scheme.1 Schematic representation of the nitrite hydrogenation over a transition metal catalyst, using hydrogen as the reducing agent

It is very clear from the above scheme that even if the overall reaction selectively forms nitrogen gas, there is the generation of considerable amount of hydroxide ions making the solution medium alkaline. The presence of increased alkalinity should be controlled either by

introducing a buffering agent or by improving the diffusion properties of the catalyst. Hence the overall supported catalyst morphology plays a significant role for these kinds of hydrogenation reactions. Porous supports have been used as the best catalytic support for this reaction also, provided if they could overcome the heat and mass transfer limitations during catalysis. Generally Pd and its bimetallic counterparts are considered as one of the best choices for catalytic hydrogenation of nitrites in the literature and a huge volume of data is available regarding its kinetics and deactivation results.⁶³⁻⁶⁷ Similarly, Pt based reports are also available for the preliminary understanding of the reaction pathways involved in this environmentally important reaction. Though literature claims the hydrogenation of nitrites has intrinsic diffusion barriers, there is no experimental proof in literature regarding the direct correlation of diffusion limitation with the catalytic activity in case of nitrite hydrogenation on Pt based porous materials. Instead few literature results claims the morphological control of Pt nanoparticles as well as the active plains for the final selectivity towards nitrogen during nitrite hydrogenation in water.⁶⁸⁻⁶⁹ In 2004 Strukul et al attempted to correlate the activity of Pt and Pd supported on SnO₂ with variable surface area and pore size to its hydrogenation capability of nitrates.⁷⁰ Their experimental procedure include the application of a buffering agent CO₂ to maintain the overall pH neutral throughout the reaction; many literature results claim the utilisation of such a buffering agent to improve the selectivity towards the nitrogen during the catalytic hydrogenation of nitrites. Lefferts et al detailed the support effect on the selectivity of nitrite reduction in water by taking Pd on carbon nano fibres under varying conditions like temperature, nitrite to hydrogen ratio as well as reaction pH.⁷¹ Thus still there needs to be considerable amount of efforts to design catalytic process to selectively convert the nitrites into nitrogen without the generation of ammonia.

1.8 Instrumentations

1.8.1 UV-Visible spectroscopy

The formation as well as the size of the metal nanoparticles can be confirmed through UV-Visible analysis. Metal nanoparticles absorbs light in the UV-Vis region of the electromagnetic spectrum and will give a broad absorption spectra; typically Gold, silver and copper nanoparticles in the visible region. These absorptions are due to the phenomenon of surface Plasmon Resonance (SPR). The SPR can be described as the collective oscillation of the conductive electrons in a solid stimulated by incident light.

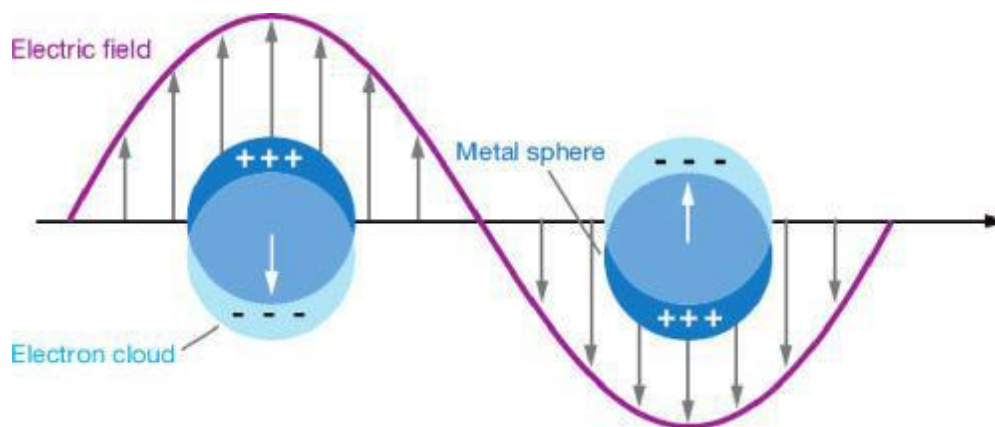


Figure.2: schematic representation of Surface Plasmon Resonances⁷²

Surface plasmon is created at the boundary of a metal surface and these represent the quantized oscillations of surface charges produced by an external electric field. For surface plasmon on metal nanoparticles there are a number of modes (ℓ). The most important is the $\ell = 1$ resonance (Mie theory) which has an optically active dipole field configuration. For nanoparticles of gold, copper and silver this dipole resonance occurs in the UV-Vis region making the nanoparticles useful for optical applications.⁷³⁻⁷⁴ As well as the dielectric properties of the material, the frequency of the dipole resonance depends upon the size and shape of nanoparticles.⁷⁵ Since the SPR depends on the size, shape and aggregation of Au NPs⁷⁶ UV-Vis spectroscopy is a very useful tool which allows estimation of gold nanoparticles size, shape, concentration and aggregation level. Surface Plasmon resonance in the nano meter scale is called Localized surface plasmon resonance. In core/shell nanoparticles characterization, UV-Vis is used to compare the individual spectra of core, shell, and core/shell material. UV-Vis analysis and the spectra was acquired using Varian Cary 50 Conc UV-Vis spectrophotometer with a dual beam source for the current study and each spectrum is correct with blank runs.

1.8.2 X-ray diffraction analysis

Powder X-ray diffraction technique is widely used to identify the unknown compounds, crystallite size and the identification of lattice parameters for the crystalline materials. Here, the interaction of the material with x-rays (Cu $K\alpha$ or Mo $K\alpha$) will results in the diffraction of these beams to a specific directions according to Bragg's equation,

$$n\lambda = 2d\sin\theta$$

Where, λ is the wavelength of the x-ray used, d is the interplanar spacing, Θ is the angle between the incoming x-ray and the normal to the reflecting lattice plane and n is the order of reflection, which is normally an integer.

Bragg peaks are measured by observing the intensity of the scattered x-rays and the width of the peak generally gives the ordering of the channels in porous solids as well as the size of the crystallite in nanomaterials. Thus Scherrer formulae is used to calculate the crystallite size of the particles,

$$D = \frac{K\lambda}{\beta \cos\theta}$$

Where, D is the crystallite size, λ is the wavelength of x-ray used, Θ is the diffracting angle and β is the full width at half maximum of the diffracting peak under consideration. K is a constant which normally is taken as 1.

The following specific instruments are used in the current thesis work, small and wide angle powder X-ray diffraction (XRD) of all the sample were measured on a PANalytical X`pert Pro duel goniometer diffractometer. A proportional counter detector was used for low angle experiments and an X`celerator solid state detector was employed in wide angle experiments. Cu $K\alpha$ radiation source (1.5418 Å) is used with a Ni filter and data collection was carried out using a flat holder in Bragg-Brentano geometry (0.20/min). In chapter.3 low angle XRD measurements have been performed using a D8 advanced X-ray diffractometer (Bruker AXS), low angle X-ray diffraction patterns were acquired from 0.3° to 6° with 0.02° step size.

1.8.3 N₂ porosimetry analysis

Surface area analysis by N₂ porosimetry is one of the promising tools in identifying the textural property of solid supported materials. The analysis is based on the theory developed by Brunner, Emmet and Teller considering the multilayer adsorption and capillary condensation in mesoporous materials. The BET equation can be represented as,

$$\frac{P}{V(P_0 - P)} = \frac{1}{V_m C} + \frac{(C - 1)}{V_m C} (P/P_0)$$

Where, P is the adsorption equilibrium pressure, P_0 is the saturation vapour pressure of the adsorbate at the experimental temperature, V is the volume of the N₂ adsorbed at pressure P , V_m is the volume of the adsorbate needed for monolayer adsorption and C is a constant

related to the heat of adsorption and liquefaction. A linear relationship between $P/V (P_0 - P)$ and P/P_0 is used to obtain the volume of nitrogen adsorbed under the experimental condition. Further the surface area of the catalyst can be calculated from the equation,

$$SA = ((V_m)(22414)) N_a \sigma$$

N_a is Avogadro number and σ is mean cross sectional area covered by one adsorbate molecule, which is generally considered as 0.162 nm^2 for N_2 molecule. Here, V_m can be calculated by plotting $\frac{P}{V (P_0 - P)}$ against P/P_0 and the slope of which will give the value of V_m as, $V_m = 1/(\text{slope} + \text{y-intercept})$

Several methods are there to completely extract the other textural properties like pore size, pore volume and external surface area. Barrett-Joyner-Halenda (BJH) method is very popular among the various methods in calculating the pore size distribution in mesoporous materials. The pore size distribution is generally represented in terms of $\Delta V_p/\Delta r_p$ versus r_p , where V_p is the mesopores volume and r_p is the mesopores radius.

Specifically in chapter.2 surface area measurements were carried out using Autosorb 1C (Catalysis Division, CSIR-NCL) while in chapter.3 Tristar 3020 (Lille University, France) is used. The instruments specifications as well as experimental conditions are as follows, Nitrogen adsorption/desorption isotherms were collected using automated gas adsorption analyser (Autosorb/Tristar3020). The program consists of both adsorption and desorption branch and typically ran at $-196 \text{ }^\circ\text{C}$ after samples were degassed at $250 \text{ }^\circ\text{C}$ for 3 hrs once the final temperature had been maintained. Specific surface area was calculated via the BET model at relative pressure of $P/P_0 = 0.06 - 0.3$. The total pore volume was estimated from the uptake of adsorbate at a relative pressure of $P/P_0 = 0.99$. The pore size distribution was calculated using DFT/BJH model applied to the desorption branch of the isotherm.

1.8.4 Raman spectroscopy

The inelastic scattering from a material under the Raman laser light forms the basis of Raman spectroscopy. Here, the incoming monochromatic light will interact with the molecule/material under consideration and will undergo shift in their frequency either by gaining energy or losing energy to the interacting molecule. Thus the inelastically scattered light can directly give information about the chemical nature of the material under

consideration. The inelastically scattered light with lower frequency is called Stokes lines and the one with increased frequency is called anti-Stokes lines. The elastically scattered light is called Rayleigh lines. These Raman lines can give potential information related to the bonding and co-ordination environment present in the metal oxide as well as the mode of adsorption in the case of catalysis if used under operando conditions.

For the present thesis work LabRam spectrometer make HJY (CSIR-NCL) was used for Raman analysis with a laser wavelength of 633 nm and 514 nm depending upon the sample properties.

1.8.5 Fourier Transformed Infrared Spectroscopy (FTIR)

The absorption of radiation in the infra red region can clearly tell about the nature of the chemical bond involved in a material/molecule. The basic requirement for the absorption to happen is that there should be a change in dipole moment associated with each absorption. The IR spectrum of a molecule is a major tool used in the structure elucidation as well as determining the purity of the compounds. In practical sense the sample will be subjected to interact with IR radiation, absorption occurs when the frequency of the vibration resonates with the incident frequency and gives an absorption spectrum in the detector. In actual practice the FTIR instrument works by using a beam of light with a combination of different frequencies than a monochromatic source used in the conventional IR spectrometer. This process of interaction of the sample with the beam of light with varying combinations of frequencies will be repeated several times and the amount of absorbed frequencies will be noted. These data points will be treated with a mathematical model through Fourier Transformation to get a meaningful absorption data in terms of absorption against wavelength of light absorbed. Since these absorptions correspond to a particular orientation of the bonds, specific symmetry of the material or bonds, it acts as fingerprints for that particular material/molecules.

Through out this thesis work FTIR analysis of the pelletized samples is carried on Bruker Tensor 27 FTIR spectrophotometer with DTGS detector under room temperatures using KBr as internal standard.

1.8.6 Nuclear Magnetic Resonance Spectroscopy (NMR)

The physical and chemical nature of a material can be identified by utilising the magnetic property of some of the nuclei present in that material, and NMR utilises this property of

materials. When these magnetic nuclei (Like ^1H , ^{29}Si , ^{27}Al etc) kept under a magnetic field interacts with the external field under resonant conditions and the spectrum obtained in this condition can reveal about the co-ordination environment, structure and purity of the sample under consideration. The chemical shift values obtained in the spectrum can be used to clearly identify the co-ordination environment of the nuclei under consideration and hence the structural elucidation of the material or molecule. The shape and width of the spectral lines can directly tell the bonding pattern in the case of solid state NMR spectra.

For the present study, the room temperature ^{29}Si NMR spectra were recorded on a JEOL 400 spectrometer at a frequency of 8 KHz.

1.8.7 Inductively coupled Plasma spectroscopy (ICP)

This spectroscopy is used to identify as well as quantify the presence of trace elements in the sample under consideration. The method basically generates ions of a particular element by utilising inductively coupled plasma and the characteristic electromagnetic radiations emitted by these excited atoms or ions will be detected and used for quantification of that particular element. The intensity of these emissions is directly proportional to the concentration of the analyte.

In the present thesis work, ICP-AES analyses were done on an optical emission spectrometer Therm IRIS intrepid II XSP after the sample is dissolved in HF solution.

1.8.8 Scanning Electron Microscopy (SEM)

SEM is widely used for understanding the 3D morphology of materials and hence a major tool in the material characterisation which works based on the electron microscopy principles. Here, a focused electron beam is used to scan the samples, and the secondary electrons emitted from the samples/atoms by the excitation of the electron beams is focused and collected to generate the 3D image of the sample. Since these secondary electrons are emitted from the surface of the material, resolutions as high as 1 nm can be achieved in an SEM under the secondary electron imaging mode.

The SEM data represented in chapter.2 and chapter.4 are collected on a FEI, model quanta 200 3D with EDX for elemental analysis (CMC, CSIR-NCL), while in chapter.3 all the SEM images are collected on Hitachi SU-70, SEM-FEG (Laboratoire de Réactivité de Surface-CNRS UMR 7197, Université Pierre et Marie Curie, France)

1.8.9 Transmission Electron Microscopy (TEM)

It is used for understanding the absolute morphology of the material under atomic resolution using the transmitted beam of the incident light through the sample. TEM works based on the principle of optical microscopy but uses focused electron beams as the source. The lower de-broglie wavelength of the electron beams allows it to give higher resolution when compared with a normal optical microscope. Hence, it is possible to get atomic resolution under a TEM instrument (the accelerated electron wavelength is about 2.24 pm at 300 keV).⁷⁷ This tool has been widely used to understand the morphology of nanomaterials as well as metal oxide materials.

In chapter 2 and chapter 4 all the transmission electron microscopy images collected on Tecnai (Model F30, CMC, CSIR-NCL) operating at 300 kv, while in chapter.3 the TEM images were collected on JEOL JEM 2011 with a LaB6 source (Lille University, France). Samples were dispersed in ethanol with low power sonication before drop casting the sample on a carbon coated Cu grid for observation.

1.8.10 X-ray photoelectron spectroscopy (XPS)

XPS is a surface science technique widely used to precisely identify the chemical composition of the active components in heterogeneous catalysis. XPS spectra are basically obtained by irradiating the sample under consideration with a beam of X-rays and measuring the kinetic energy of the ejected electrons from the sample surface. An XPS instrument works based on the principle of photoelectric effect, where the kinetic energy of the ejected electron will directly give the work function of the materials and thereby indirectly giving the ionisation energy of oxidation state of the material/metal under consideration.

$$KE = h\nu - BE - \emptyset$$

Where, KE is the kinetic energy of the ejected electrons, $h\nu$ is the incident photon energy, BE is the binding energy of the electron and \emptyset is the work function of the spectrometer.

Since the mean free path of the electrons are quit high under vacuum when compared to ambient conditions, XPS measurements needs ultra high vacuum conditions to obtain a decent spectra. Likewise, those electrons which are not undergoing inelastic scattering will only be able to reach the detector and hence the technique is highly surface sensitive. The

ambient pressure XPS has been the area of interest for the past few years where one can analyse the sample under few tens of millibar pressure and thereby reducing the so called pressure gap which exists in surface science studies.

The chemical nature of the samples discussed in chapter.2 and chapter.4 is investigated using XPS analysis (APPES, PREVAC, Centre of excellence in surface science, CSIR-NCL) in the UHV mode using Al K α monochromator, while in chapter.3 XPS experiments were performed using an AXIS Ultra DLDRatos spectrometer equipped with Al K α monochromator and a charge compensation gun.

1.8.11 Gas Chromatography

Gas chromatography is an analytical tool widely used for the separation, identification as well as quantification of the analyte present in a sample based on the differential adsorption of each species on a stationary phase. The mobile phase usually an inert gas will carry the sample through the long stationary phase packed in the form a column and will get adsorbed based on the affinity of the analyte towards the surface polarity or surface property of the stationary phase. Based on the interaction between the analyte and stationary phase the retention time varies and separation happens and the analyte will reach to the detector and will be identified and quantified. The detectors associated with a gas chromatographic instrument will be either Flame ionisation (FID) or a Thermal Conductivity detector (TCD).

1.9 Scope and Objective of the thesis work

Synthesis of nanostructured materials with monodisperse size and well defined architecture result in tailor made application of the materials in catalysis. Anchoring or encapsulation of metal nanoparticles in a predefined pore system can impart high thermal stability to the active catalytic sites which enables the sustainable catalytic activity. In this regards, gold-mesoporous silica still finds its application in the fundamental model reaction like CO oxidation. The size dependency of Au nanoparticles in CO oxidation catalysis and the scope of using inert and cheap support like SiO₂ are addressed. To accomplish this, synthesis of porous silica as a novel support for CO oxidation by making nanostructured Au-Silica catalysts is attempted. Further, a composite thin film model catalyst of this category could reduce the material gap in surface science studies. Alongside hierarchical porous materials also acts as good catalytic supports since interconnected pore systems are largely available in these systems. Design and development of hierarchical alumina with enhanced diffusion

properties is extremely important, especially where liquid phase reactions are involved which are controlled by mass transfer limitations. It is important to understand the nature and type of pore architecture which is best suited for specific reactions. Pt nanoparticles deposited on hierarchical porous alumina architectures are identified as the best choice owing to its importance in industrial catalysis to co-relate the support morphology with catalytic applicability as well as product selectivity. Thus the thesis focus on studying the synthesis of novel materials with added functionalities and their application in environmentally important reactions like CO oxidation and denitrification of ground water.

1.10 References:-

1. D. A. J. Rouquerol, C. W. Fairbridge, D. H. Everett, J. H. Haynes, ; N. Pernicone, J. D. F. Ramsay, K. S. W. Sing, K. K. Unger, *Pure & Appl. Chem.*, 1994, **66**, 1739-1758.
2. Y. Wan and Zhao, *Chemical Reviews*, 2007, **107**, 2821-2860.
3. A. Stein, S. G. Rudisill and N. D. Petkovich, *Chemistry of Materials*, 2014, **26**, 259-276.
4. N. D. Petkovich and A. Stein, *Chemical Society Reviews*, 2013, **42**, 3721-3739.
5. A. Feinle, M. S. Elsaesser and N. Husing, *Chemical Society Reviews*, 2016, **45**, 3377-3399.
6. C. J. Brinker, in *The Colloid Chemistry of Silica*, American Chemical Society, 1994, vol. 234, ch. 18, pp. 361-401.
7. S. Mann, S. L. Burkett, S. A. Davis, C. E. Fowler, N. H. Mendelson, S. D. Sims, D. Walsh and N. T. Whilton, *Chemistry of Materials*, 1997, **9**, 2300-2310.
8. D. Grosso, F. Cagnol, G. J. d. A. A. Soler-Illia, E. L. Crepaldi, H. Amenitsch, A. Brunet-Bruneau, A. Bourgeois and C. Sanchez, *Advanced Functional Materials*, 2004, **14**, 309-322.
9. G. J. d. A. A. Soler-Illia, A. Louis and C. Sanchez, *Chemistry of Materials*, 2002, **14**, 750-759.
10. Y. Deng, J. Wei, Z. Sun and D. Zhao, *Chemical Society Reviews*, 2013, **42**, 4054-4070.
11. F. Cavani, F. Trifirò and A. Vaccari, *Catalysis Today*, 1991, **11**, 173-301.
12. K. Rajeshwar and N. R. de Tacconi, *Chemical Society Reviews*, 2009, **38**, 1984-1998.
13. A. Varma, A. S. Mukasyan, A. S. Rogachev and K. V. Manukyan, *Chemical Reviews*, 2016.
14. W. Shi, S. Song and H. Zhang, *Chemical Society Reviews*, 2013, **42**, 5714-5743.
15. D. R. Modeshia and R. I. Walton, *Chemical Society Reviews*, 2010, **39**, 4303-4325.
16. A. W. Snow and H. Wohltjen, *Chemistry of Materials*, 1998, **10**, 947-949.
17. R. Narayanan and M. A. El-Sayed, *Nano Letters*, 2004, **4**, 1343-1348.
18. T. Zambelli, J. Winterlin, J. Trost and G. Ertl, *Science*, 1996, **273**, 1688-1690.
19. J. P. Gabaldon, M. Bore and A. K. Datye, *Topics in Catalysis*, 2007, **44**, 253-262.
20. P. J. Murphy and M. S. LaGrange, *Geochimica et Cosmochimica Acta*, 1998, **62**, 3515-3526.
21. S. Ivanova, C. Petit and V. Pitchon, *Applied Catalysis A: General*, 2004, **267**, 191-201.
22. G. C. Bond and D. T. Thompson, *Gold Bulletin*, 2000, **33**, 41-50.
23. R. Zanella, S. Giorgio, C. R. Henry and C. Louis, *The Journal of Physical Chemistry B*, 2002, **106**, 7634-7642.
24. S. E. Golunski, *Platinum Metals Review*, 2007, **51**, 162-162.
25. M. Haruta, *CATTECH*, 2002, **6**, 102-115.
26. G. M. Veith, A. R. Lupini, S. Rashkeev, S. J. Pennycook, D. R. Mullins, V. Schwartz, C. A. Bridges and N. J. Dudney, *Journal of Catalysis*, 2009, **262**, 92-101.
27. P. R. Selvakannan, K. Mantri, J. Tardio and S. K. Bhargava, *Journal of Colloid and Interface Science*, 2013, **394**, 475-484.
28. M. Perez-Cabero, J. El Haskouri, B. Solsona, I. Vazquez, A. Dejoz, T. Garcia, J. Alvarez-Rodriguez, A. Beltran, D. Beltran and P. Amoros, *Journal of Materials Chemistry*, 2010, **20**, 6780-6788.
29. P. M. Arnal, M. Comotti and F. Schüth, *Angewandte Chemie International Edition*, 2006, **45**, 8224-8227.

30. C. Galeano, R. Güttel, M. Paul, P. Arnal, A.-H. Lu and F. Schüth, *Chemistry – A European Journal*, 2011, **17**, 8434-8439.
31. C.-H. Lin, X. Liu, S.-H. Wu, K.-H. Liu and C.-Y. Mou, *The Journal of Physical Chemistry Letters*, 2011, **2**, 2984-2988.
32. P. Innocenzi and L. Malfatti, *Chemical Society Reviews*, 2013, **42**, 4198-4216.
33. G. Wirnsberger, B. J. Scott and G. D. Stucky, *Chemical Communications*, 2001, 119-120.
34. Y. Bian, X. Wang, Z. Zeng and Z. Hu, *Surface and Interface Analysis*, 2013, **45**, 1317-1322.
35. S. Dahl, A. Logadottir, R. C. Egeberg, J. H. Larsen, I. Chorkendorff, E. Törnqvist and J. K. Nørskov, *Physical Review Letters*, 1999, **83**, 1814-1817.
36. M. Mavrikakis, P. Stoltze and J. K. Nørskov, *Catalysis Letters*, 2000, **64**, 101-106.
37. C. P. Vinod, J. W. Niemantsverdriet Hans and B. E. Nieuwenhuys, *Applied Catalysis A: General*, 2005, **291**, 93-97.
38. E. Stavitski and B. M. Weckhuysen, *Chemical Society Reviews*, 2010, **39**, 4615-4625.
39. T. Kjellman and V. Alfredsson, *Chemical Society Reviews*, 2013, **42**, 3777-3791.
40. S. L. González-Cortés, S. M. A. Rodulfo-Baechler, T. Xiao and M. L. H. Green, *Catalysis Letters*, 2006, **111**, 57-66.
41. W. Deng, M. W. Toepke and B. H. Shanks, *Advanced Functional Materials*, 2003, **13**, 61-65.
42. Q. Wu, F. Zhang, J. Yang, Q. Li, B. Tu and D. Zhao, *Microporous and Mesoporous Materials*, 2011, **143**, 406-412.
43. P. Kim, Y. Kim, H. Kim, I. K. Song and J. Yi, *Applied Catalysis A: General*, 2004, **272**, 157-166.
44. I. Chen and D. W. Shiue, *Industrial & Engineering Chemistry Research*, 1988, **27**, 1391-1396.
45. C. H. Bartholomew and R. J. Farrauto, *Journal of Catalysis*, 1976, **45**, 41-53.
46. J. R. Gaudet, A. de la Riva, E. J. Peterson, T. Bolin and A. K. Datye, *ACS Catalysis*, 2013, **3**, 846-855.
47. K. Persson, P. O. Thevenin, K. Jansson, J. Agrell, S. G. Järås and L. J. Pettersson, *Applied Catalysis A: General*, 2003, **249**, 165-174.
48. M. Yashima, L. K. L. Falk, A. E. C. Palmqvist and K. Holmberg, *Journal of Colloid and Interface Science*, 2003, **268**, 348-356.
49. D. H. Kim, S. I. Woo and O. B. Yang, *Applied Catalysis B: Environmental*, 2000, **26**, 285-289.
50. S. Park, M. Kim, D. H. Koo and S. Chang, *Advanced Synthesis & Catalysis*, 2004, **346**, 1638-1640.
51. M. Bilal and S. D. Jackson, *Catalysis Science & Technology*, 2012, **2**, 2043-2051.
52. N. Perret, F. Cárdenas-Lizana and M. A. Keane, *Catalysis Communications*, 2011, **16**, 159-164.
53. F. Cárdenas-Lizana, S. Gómez-Quero and M. A. Keane, *Catalysis Letters*, 2009, **127**, 25-32.
54. A. Manasilp and E. Gulari, *Applied Catalysis B: Environmental*, 2002, **37**, 17-25.
55. A. Shamsi, J. P. Baltrus and J. J. Spivey, *Applied Catalysis A: General*, 2005, **293**, 145-152.
56. A. T. Madsen, E. H. Ahmed, C. H. Christensen, R. Fehrmann and A. Riisager, *Fuel*, 2011, **90**, 3433-3438.
57. A. Dolev, G. E. Shter and G. S. Grader, *Journal of Catalysis*, 2003, **214**, 146-152.
58. J.-H. Lee and H. H. Kung, *Catalysis Letters*, 1998, **51**, 1-4.

59. M. Haruta, S. Tsubota, T. Kobayashi, H. Kageyama, M. J. Genet and B. Delmon, *Journal of Catalysis*, 1993, **144**, 175-192.
60. M. Valden, X. Lai and D. W. Goodman, *Science*, 1998, **281**, 1647-1650.
61. M. Haruta, *Catalysis Today*, 1997, **36**, 153-166.
62. M. M. Schubert, S. Hackenberg, A. C. van Veen, M. Muhler, V. Plzak and R. J. Behm, *Journal of Catalysis*, 2001, **197**, 113-122.
63. S. Hörold, K. D. Vorlop, T. Tacke and M. Sell, *Catalysis Today*, 1993, **17**, 21-30.
64. I. Mikami, Y. Sakamoto, Y. Yoshinaga and T. Okuhara, *Applied Catalysis B: Environmental*, 2003, **44**, 79-86.
65. H. Qian, Z. Zhao, J. C. Velazquez, L. A. Pretzer, K. N. Heck and M. S. Wong, *Nanoscale*, 2014, **6**, 358-364.
66. J. K. Chinthajjala, A. Villa, D. S. Su, B. L. Mojet and L. Lefferts, *Catalysis Today*, 2012, **183**, 119-123.
67. A. Pintar, G. Berčič and J. Levec, *AIChE Journal*, 1998, **44**, 2280-2292.
68. A. Miyazaki, T. Asakawa, Y. Nakano and I. Balint, *Chemical Communications*, 2005, 3730-3732.
69. M. Duca, M. C. Figueiredo, V. Climent, P. Rodriguez, J. M. Feliu and M. T. M. Koper, *Journal of the American Chemical Society*, 2011, **133**, 10928-10939.
70. M. D'Arino, F. Pinna and G. Strukul, *Applied Catalysis B: Environmental*, 2004, **53**, 161-168.
71. J. K. Chinthajjala and L. Lefferts, *Applied Catalysis B: Environmental*, 2010, **101**, 144-149.
72. K. A. Willets and R. P. Van Duyne, *Annual Review of Physical Chemistry*, 2007, **58**, 267-297.
73. H. Xu, E. J. Bjerneld, M. Käll and L. Börjesson, *Physical Review Letters*, 1999, **83**, 4357-4360.
74. T. W. Ebbesen, H. J. Lezec, H. F. Ghaemi, T. Thio and P. A. Wolff, *Nature*, 1998, **391**, 667-669.
75. K. L. Kelly, E. Coronado, L. L. Zhao and G. C. Schatz, *The Journal of Physical Chemistry B*, 2002, **107**, 668-677.
76. M.-C. Daniel and D. Astruc, *Chemical Reviews*, 2003, **104**, 293-346.
77. C. B. C. David B. Williams, *New York, NY* 2009.

Chapter 2

Au-SiO₂ powder, Core shell nanostructures and its environmental catalysis

published major conclusions from this chapter,

1. A. C. Sunil Sekhar, K. Sivaranjani, C. S. Gopinath* and C. P. Vinod*, *Catalysis Today*, 2012, 198, 92-97
2. A. C. Sunil Sekhar, C. J. Meera, K. V. Ziyad, C. S. Gopinath and C. P. Vinod*, *Catalysis Science & Technology*, 2013, 3, 1190-1193
3. A. C. Sunil Sekhar, K. V. Ziyad, Y. Soni and C. P. Vinod*, *ChemCatChem*, 2015, 7 (7), 1222-1230

2.1 Introduction

Gold has always fascinated the scientific community ever since the discovery of the catalytic capabilities of gold¹⁻² when its size is reduced to nano meter range.³ The scientific fraternity is challenged by these discoveries to establish a correlation between the size of these nanoparticles and its chemical and physical behaviours under ambient conditions as well as industrially relevant conditions. It is well known that the stability of these NPs are highly sensitive to its local environment; and to make use of their significant characters for useful purposes, one has to think about stabilizing these nanoparticles either by chemical methods or by physical methods. Surfactant/capping agent mediated chemical synthesis of these nanoparticles have an upper hand over the conventional impregnation method when it comes in the case of size and shape of the NPs.⁴⁻⁵ Moreover, in the recent past it has been well documented that many of the chemical properties, specifically the catalytic properties are mainly dependent on the size of gold NPs as well as the exposed facets.⁶⁻⁹ The advantages like the ease of catalyst separation and recyclability has resulted in the application of gold nanoparticles in heterogeneous catalysis. In such cases the metal support interaction as well as the thermal stability of nanoparticles will decide the catalytic applicability of supported gold catalyst under industrially and environmentally significant reactions. Oxide matrices are conventionally considered as the best supports for transition metal nanoparticles mediated reactions under ambient and industrially challenging conditions. This tradition has come from the repeated observation of better catalytic activity in these systems on account of the better dispersion and stabilisation of metal nanoparticles. Yet, thermal sintering of metal nanoparticles under reaction condition owing to the higher mobility of the nanoparticles leads to the irreversible aggregation and thus lesser catalytic activity. Sintering is a severe problem in gold catalysis, which undergoes morphological transformations and particle growth under

reaction conditions. Hence, stabilising gold nanoparticles on heterogeneous supports, especially silica is a puzzling problem in nanoparticles mediated heterogeneous catalysis.

When it comes to the case of heterogeneous supports, silica with large surface area as well as tunable porosity stands itself as the ideal choice for many of the catalytic reactions. In addition to that the high thermal stability along with its surface hydroxyl groups makes it a suitable candidate for high temperature studies as well as functional points for anchoring metal nanoparticles. Specifically in the case of gold nanoparticles, the conventional metal supporting methodology like impregnation or deposition-precipitation failed to result in active catalysts for high temperature reactions on a gold-silica catalyst. This is mainly attributed to the silica surface charge as well as the nature of the gold precursor widely used (HAuCl_4 solution), along with the acidic conditions adapted for metal loading in the impregnation procedure.¹⁰⁻¹¹ On top of that, the weaker interaction of the supported gold nanoparticles on silica results in its irreversible migration and thus sintering leading to poor catalytic life cycle under harsh reaction conditions. Though Bond started the gold catalysis with a broader perspective in the early 80's, the legacy continued with Haruta and Hutchings. Further, the notorious nature of gold on a silica support which undergo sintering in presence of reactive gases as well as high temperature reaction conditions provoked us to make sinter resistant Au-silica nanocatalysts in its powder form with variable morphology and to check for the applicability in the environmentally significant CO oxidation reaction. It has been proposed in many past studies that metal nanoparticles can be anchored on heterogeneous supports by selectively functionalising the support surface and then making use of the electrostatic interactions to support active metal phase on the support, followed by its reduction to metallic state. Literature shows the catalytic activity data for Au supported on a variety of heterogeneous supports. On a gold catalyst for CO oxidation, the supports so far studied can be categorized into two based on their oxygen activation; active supports (TiO_2 ,

Fe₂O₃ etc) and inactive supports (SiO₂ and Al₂O₃). A number of reports are there to support the above said fact were they show that active supports like TiO₂ outperform the inactive supports when gold nanoparticles supported such materials are utilized for CO oxidation reaction.^{10, 12} Silica being inert cannot activate molecular oxygen, similarly gold with negligible oxygen sticking coefficient cannot activate molecular oxygen at ambient conditions; thus limiting its applicability to high temperature CO oxidation. Anchoring the active gold nanoparticles within the mesoporous channels has emerged as a successful method to prevent the sintering of Au nanoparticles and thereby enhancing the catalytic cycle life. Though, the literatures show better activity on heterogeneous gold catalysts, they vary from one another in the synthesis methodologies. Critical aspects considered while developing such synthesis methodology is the size and shape of gold nanoparticles as well as better metal-support interaction. Most of these reports are based on the size dependency of gold catalysts for CO oxidation reaction. Dealing with gold nanoparticles of size above the widely accepted size range of 3-5 nm for CO oxidation reaction will help one to exactly understand the major factor involved in CO Oxidation reaction viz “size dependency Vs metal support interaction”. Hence efforts are taken to understand the involvement of metal support interaction in tuning the final catalytic activity by selectively controlling the synthesis methodology and thus improving the catalytic activity in an otherwise considered bad support silica. In the first section, ultra small gold nanoparticles are incorporated inside the pore channels of silica in a novel one pot synthesis methodology and thereby enhancing its sinter resistance by the restricted migration under reaction condition. Such an anchoring strategy in a single step without the application of any anchoring agent has not been reported by many groups. A strategy where a template which could theoretically act as structure directing agent for mesoporous silica synthesis as well as a reducing agent for gold nanoparticles is demonstrated.

Encapsulating active metal NPs inside a shell has been identified as an elegant route to enhance the thermal stability of the nanostructured catalyst in the recent past.¹³⁻¹⁶ Such a core@shell system can be ideal for high temperature reactions as well as size dependent catalytic reactions if the shell is porous enough to facilitate the diffusion of reactants and products. Schuth et al¹³ developed a series of such core shell as well as yolk shell systems and showed its higher sinter resistance capability under reactive environment at elevated temperatures. Similarly, Somorjai et al¹⁷ showed the exceptional thermal stability and catalytic life cycles for their Pt@m-silica catalyst in the past pointing towards the applicability of encapsulation strategy. By adopting seed mediated synthesis methodology gold nanoparticles of size 8-12 nm has been synthesised and used as the active phase for CO oxidation. The possibility of application of a capping agent for gold nanoparticles as well as the structure directing agent for silica synthesis could potentially reduce the complexities associated with the core-shell synthesis protocol in the case of Au@SiO₂ nanoparticles. Hence in our synthesis, Cetyl trimethyl ammoniumbromide (CTAB) is utilised as the capping agent for gold nanoparticles and structure directing agent for silica synthesis in our protocol. As mentioned previously, an encapsulation strategy is designed to cover the gold nanoparticles within a porous silica shell so that a number of catalytic cycles can be tested and significant data can be drawn out to understand the applicability of the core shell catalyst in terms of its sinter resistance and catalytic activity. Moving further to improve the catalytic applicability of such a sinter resistant core shell system, efforts have been taken to introduce a reducible centre on the silica support so that the critical oxygen dissociation rate can be increased and thus catalytic activity. Incorporation of a heteroatom like “Ti” could effectively improve the oxygen activation capacity and hence can enhance the overall catalytic activity like CO oxidation where oxygen dissociation is considered to be the rate determining step. Efforts have been taken to develop such a core shell Au@Ti-SiO₂ system by modifying the

Au@silica system and are tested for its CO oxidation capability to derive direct evidences for the much acclaimed oxygen activation/dissociation on a reducible support. Theoretically, on incorporation of Ti in the SiO₂ matrix, there can be creation of Ti³⁺/Ti⁴⁺ system results in the reducible nature of the supports and the generated oxygen vacancies plays the key role in oxygen dissociation phenomenon through superoxides.

Thus the chapter 2 specifically deals with Au-silica nanocatalysts in different morphology and also its modifications and its catalytic activity for the environmentally significant CO oxidation reactions. This chapter is further subdivided into three part which are as follows,

2a. Au-mesoSiO₂ powder catalyst and its CO oxidation Catalysis

2b. Au@SiO₂ core shell nanocatalyst and its CO oxidation catalysis

2c. Au@Ti-SiO₂ core shell nanocatalyst and its CO oxidation catalysis

The synthesis, characterisation and catalytic activity results are given in detail in the corresponding subdivision.

2a. Au-mesoSiO₂ powder catalyst and its CO oxidation Catalysis

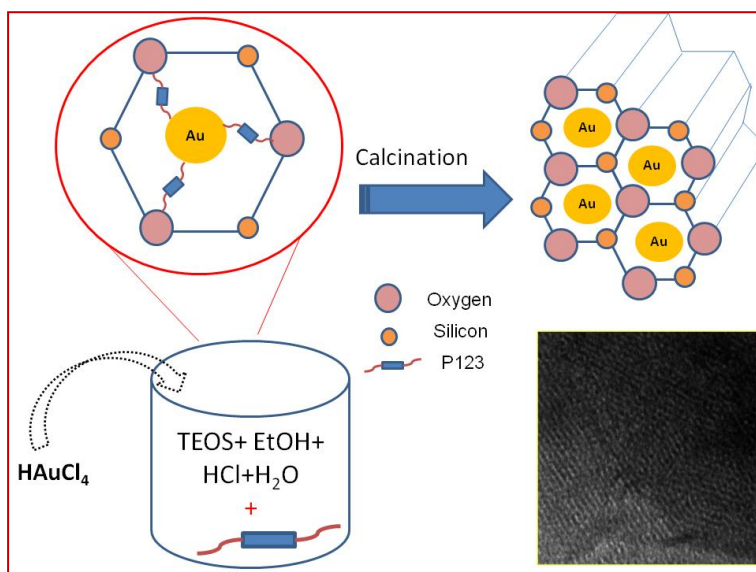
Gold nanoparticles anchored mesoporous silica nanocatalysts has been synthesised in a one pot manner where the Pluronic P123 is used as the structure directing agent for silica synthesis as well as the reducing agent for gold nanoparticle. The synthesis protocol used in the current study as well as the complete characterisation of the synthesised material followed by its catalytic test results are as follows,

2a.1 Experimental

2a.1a. Synthesis of the catalyst Au-mesoSiO₂:-

In the one pot synthesis method of the Au-SiO₂ catalyst (hereafter, GSM-23), the procedure reported by Stucky et al was modified and used.¹⁸ Typically, the synthesis procedure involves the addition of 1 mL of tetraethylorthosilicate (Merck), 10 mL ethanol, 3 mL Millipore water and 2 mL of HCl (pH=2) in a beaker followed by stirring for 1 h at 50- 80⁰C.

Simultaneously, 1g P123 (Aldrich) dissolved in 5 ml ethanol (stirred for 1 h) is added to the above silica source. The mixture is further stirred for 15 min at room temperature followed by addition of 0.1 M of the gold precursor ($\text{HAuCl}_4 \cdot 3\text{H}_2\text{O}$; 99.99%; Aldrich). The solution turned light yellow and was left for stirring for 3 h. The solution was then left still at room temperature for 24 h for sol-gel formation. The gel formed after 24 h is heated at 110°C for 1 h followed by calcination at 540°C for 4 h.



Scheme.2a.1 One pot Synthesis of Au@meso-SiO₂ nanocatalyst

The chloroauric acid molecules entrapped in the silica matrix undergoes thermal reduction during calcination results the formation of gold nano particles incorporated mesoporous silica. The synthesis procedure adopted is shown in scheme 1. Mesoporous silica was prepared by the above procedure as a reference, but without the addition of gold precursor.

2a.1b. Catalytic Test: - CO oxidation reaction

The calcined catalyst was pre-treated prior to reaction. Typically, the catalyst GSM-23 was reduced at 300°C in flowing hydrogen (100%) with a flow rate of 15 cm^3 per minute and held for an hour, then cooled to room temperature. The catalyst tests were carried under atmospheric pressure in a fixed bed reactor of diameter 14 mm details of the reactor is described elsewhere.¹⁹ Mass flow controllers (Brooks) were used to control the gas flow from the respective cylinders N₂, O₂ and CO. The reactor was placed in a tubular furnace with a uniform heating zone of 4 cm and temperature of the furnace was controlled using

Radix 6400 temperature controller. A K-type thermocouple placed in a thermowell over the catalyst is used to measure the catalyst bed temperature. A reaction gas containing 5% CO was passed over 250 mg of catalyst (pre-treated). The flow rate of the reaction gas mixture is 25 ml/min with a GHSV of $6000 \text{ cm}^3\text{g}^{-1}\text{h}^{-1}$. The conversion reported here is in the steady state where catalyst was ramped at 2°C and held at various temperatures for 10 minutes for equilibration. The data is collected at 5 minutes interval and are found to be consistent. The reactor outflow was analysed using a gas chromatograph equipped with online gas sampling valve, 91.44 cm molecular sieve 13X column and thermal conductivity detector (TCD). All the catalytic test runs were carried out from room temperature to 300°C . The hydrogen reduction at elevated temperature turns out to be a crucial step for good catalytic activity.

2a.2 Results and Discussions

2a.2.a. Structural characterisation:- UV-Vis and X-ray diffraction analysis

To understand the formation of gold nanoparticle by using P123 as a reducing agent a time dependent UV – Vis spectroscopy analysis is carried out on the interaction of P123 with gold precursor. Typically, 2 mM $\text{HAuCl}_4 \cdot 3\text{H}_2\text{O}$ and 0.4 mM P123 in 50 mL Millipore water was stirred for 1 min and time dependent UV-Vis collected. The time dependent data represented in Fig.1 shows a decrease in intensity of the peak at 212 nm originating from Au^{3+} and the development of a broad peak centered at 517 nm, indicating the reduction of Au (III) to Au (0). The gold surface plasmon peak around 517 nm clearly shows that P123 can be a versatile reducing agent for producing Au nanoparticles with very small size (see the inset Fig 2a.1a). Recently, Alexandridis and co workers in a systematic study used various amphiphilic copolymers for reduction and stabilization of gold nanoparticles at room temperature.²⁰ It is proposed that the formation of gold nanoparticles from AuCl_4^- comprises of three main steps: (i) reduction of metal ions by block copolymer in solution, (2) absorption of block copolymer on gold clusters and the reduction of metal ion on the surface of these gold clusters, and (iii) growth of metal particles and its stabilization by block copolymer.

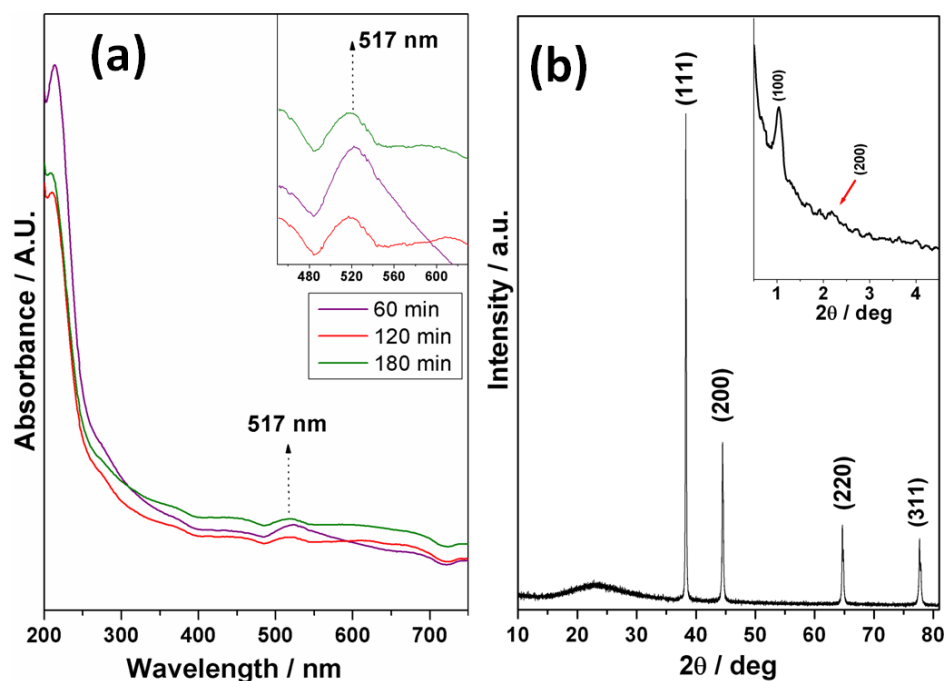


Figure.2a.1 In situ UV-Vis spectra of gold nanoparticles reduced using P123 as the reducing agent; inset clearly shows the formation of a peak at 517 nm indicating the formation of smaller gold nanoparticles (a) and (b) the x-ray diffraction analysis of the Au-mesoSiO₂ nanocatalysts after calcination; inset showing the presence of considerable extent of periodicity in the synthesised material.

It is evident from Figure.2a.1 that P123 acts as a reducing agent for gold nanoparticles and is able to maintain a considerable amount of periodicity in silica synthesis even though a one pot methodology is adapted in the current case. Figure.2a.1b. shows the XRD pattern of gold incorporated mesoporous silica. The diffraction peak at $2\Theta = 38^\circ$ and subsequent higher order reflections can be indexed to the Au (111) and other facets of gold nanoparticles. The XRD data also reveal a weak peak around $2\Theta = 23^\circ$ which can be attributed to the mesoporous silica phase. The mesoscopic organization of the material is confirmed by the low angle XRD spectrum shown in the inset of Figure.2a.1b. The low angle peak at $2\Theta = 1^\circ$ is a direct signature of such hexagonally organized silica structure.²¹

2a.2.b Textural Characterisation:- Surface area analysis

The mesoporosity of the synthesised Au@meso-SiO₂ and the bare support SiO₂ is clearly evident from the surface area analysis results. From figure.2a.2 it is evident that both the materials showed type IV isotherm with H2 hysteresis loop.²²

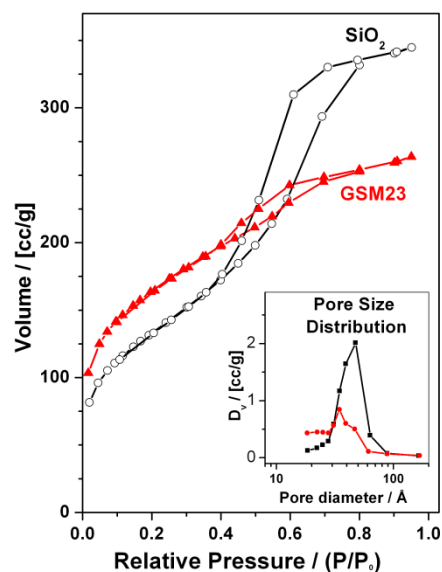


Figure.2a.2 The surface area analysis data for the samples Au@meso-SiO₂ (GSM-23) and the bare SiO₂ support after calcination

The surface area for Au- mesoporous silica (406 m²/g) is less than the pure mesoporous silica (510 m²/g). Similarly, the pore size (3.5 nm) and pore volume (0.41 cc/g) obtained from surface area measurements are smaller compared to pure mesoporous silica counterpart (4.5 nm; 0.53 cc/g). The ICP analysis carried out to find out the gold loading gave values of 3.5 atom %.

2a.2.c Microscopy analysis results:- Transmission Electron Microscopy (TEM) analysis

The high resolution transmission electron (HR-TEM) analysis of the Au@meso-SiO₂ (GSM-23) catalysts clearly shows the existence of periodicity in the silica matrix as well as the formation of ultra small gold nanoparticles. Well ordered parallel mesoporous channels are evident from Figure 2a.3 confirming the experimental evidences obtained from surface area and XRD measurements. The presence of extremely small Au nanoparticles formed inside the porous network could be identified from the TEM images (marked with yellow arrows for clarity in Figure.2a.3b). In spite of the challenges associated with identifying small particles with TEM there was clearly a definitive particle contrast from that of the support. The hexagonal pore structure is also evident from our high resolution images. It should be noted that TEM also revealed very few bigger Au nanoparticles ~60- 70 nm outside the framework silica possibly due to the agglomeration of the gold nanoparticles formed outside the channels during the calcination step. The size of the gold nanoparticle calculated to be between 2-4 nm

inside the mesochannels would serve as an ideal system for carrying out catalytic reactions probed by gold.

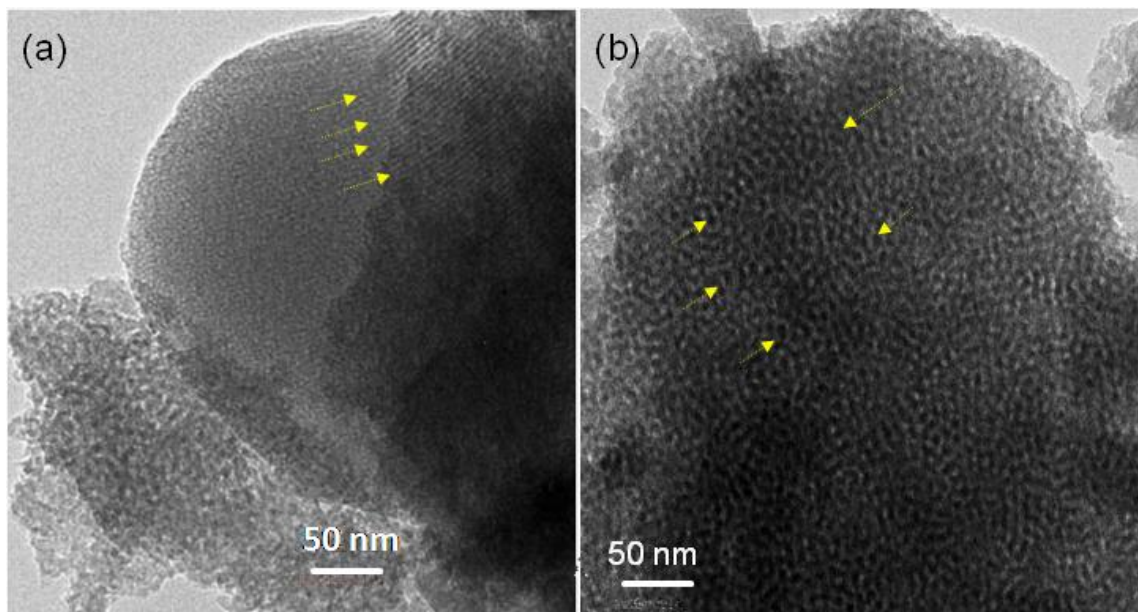


Figure.2a.3 HR-TEM images of the calcined Au@-mesoSiO₂ nanocatalysts (a) showing periodicity and (b) ultra small gold nanoparticles inside the mesopores of silica material

Hence, the materials synthesized here is expected to show catalytic activity for CO oxidation reaction if one consider the necessary requirement as 3-5 nm gold nanoparticles as well as the basic problem associated with sintering also can be neglected since the gold nanoparticles are entrapped inside the pore channels of the mesoporous silica synthesized.

2a.3 Catalytic Test results:-

The catalyst synthesized GSM-23 is further tested for its catalytic applicability for CO oxidation with and without a mild pre-treatment condition. The catalytic activity on account of various temperatures is represented in Figure.2a.4 where one can clearly see approximately 17% CO conversion on a calcined GSM-23 sample at 300 °C. It will be worth mentioning at this point that the bare silica support does not show any trace of catalytic activity even at 300 °C. It has been well documented in literature that a hydrogen pre-treatment of the catalyst is necessary before the actual catalytic cycle in case of a gold-silica system to excel in its catalytic applicability.²³⁻²⁵ Hence, mild hydrogen pre-treatment at 300 °C for our GSM-23 catalyst has been carried out and further tested for its CO oxidation capability.

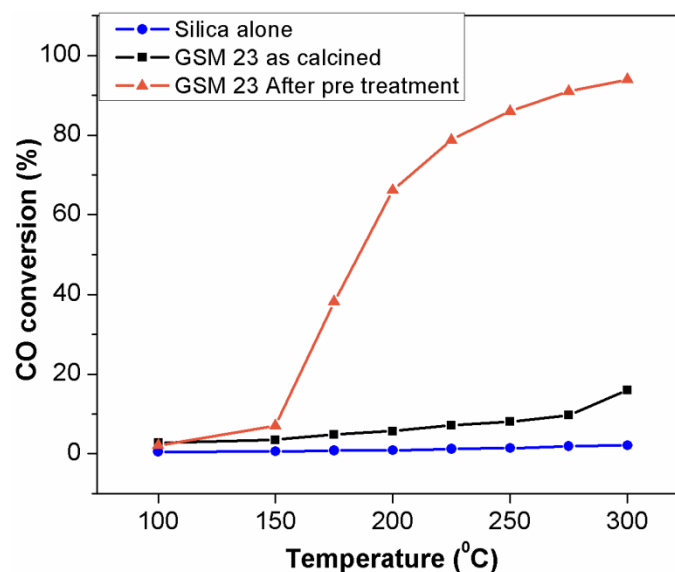


Figure.2a.4 CO oxidation activity profile Vs temperature for the catalyst GSM-23, before and after hydrogen pre-treatment (reduction). Bare silica support is also given in order to show the negligible influence of the support in actual catalysis

The mild hydrogen pre-treated sample showed exceptional enhancement in its CO oxidation activity leading to almost 100% conversion at 300 °C. This increase in activity can be correlated to the improved oxygen dissociation capability of our GSM-23 catalyst after the reduction treatment. In other words the least activity of the calcined GSM-23 when compared to the reduced GSM-23 could be the lack of the defective sites like oxygen deficient F-centers which are crucial in supplying reactive oxygen species necessary for CO oxidation. A simple calcination process will not be sufficient for the creation of those oxygen vacancies in our silica supported GSM-23 catalyst, were as these sites are plenty in the surface of popular supports like TiO₂ and MgO for gold based CO oxidation reaction even at room temperature. The mild hydrogen pre-treatment could possibly abstract oxygen from the Si-O-Si bond resulting in the formation of electron rich defect sites. Thus superoxide mediated oxygen dissociation can be envisaged in our catalysts under experimental conditions resulting in higher catalytic activity after the reduction step. Such superoxide involved oxygen activation and dissociation is proved both theoretically and experimentally in systems like Au/MgO catalysts.²⁶ In silica system such a molecular level understanding is still lacking and needs further fundamental studies to obtain direct evidences.^{24, 27}

2b. Au@SiO₂ core shell nanocatalyst and its CO oxidation catalysis

An encapsulation strategy is envisaged a better tool for developing sinter resistant catalysts and is utilised in this section of the thesis work. Monodisperse gold nanoparticles are

synthesised using the well known seed mediated synthesis methodology followed with the porous silica encapsulation. CTAB is deployed as the structure directing agent as well as capping agent in the current synthesis approach. A detailed description of the synthesis as well as sinter resistance catalytic applicability is discussed below,

2b.1 Experimental

The synthesis of the nano catalyst is a step wise process involving seed growth and support (silica) encapsulation. A modified procedure of Jana et al²⁸ is adopted here and is described in detail below,

2b.1.a. Synthesis of gold nanoparticles by Seed mediated method:-

Preparation of gold seed

65 ml aqueous solution containing 2.5×10^{-4} M HAuCl₄ (Sigma Aldrich, 99.9%) and 2.5×10^{-4} M trisodium citrate (Alfa Aesar) was prepared in a conical flask. Next 2 mL of ice –cold freshly prepared 0.1M NaBH₄ (Spectrochem 96%) solution was added to the solution while stirring. The pink colour of the resulting solution shows the formation of nano gold.

Preparation of growth solution

200 ml of the aqueous solution (2.5×10^{-4} M) HAuCl₄ mixed with 6gm of Cetyl trimethyl ammonium bromide (Spectrochem 98%) was heated until the solution turned a clean orange colour, cooled to room temperature and used as the growth solution.

The growth solution is then treated with 0.1 M (1.3 ml) of ascorbic acid (Spectrochem 98%) and added to the gold seed solution while stirring, the solution turns into wine red and the stirring continued for another 10 minutes.

2b.1.b. Silica encapsulation

In order to control the silica thickness the total solution is divided into different batches and silica encapsulation is carried out. In a typical procedure 50 ml of the above solution is stirred for 24 hrs after mixing with 20 ml of ethanol, 0.6 ml ammonia solution and 0.05 ml tetraethyl orthosilicate (Merck). Centrifuged at 10000 rpm for 10 minutes and the residue were kept for drying followed by calcinations at 500 deg for 6 hrs.

2b.1.c. Catalytic Test:- CO oxidation

The catalyst tests were carried out under atmospheric pressure in a fixed bed reactor of diameter 14 mm. More detail of the reactor is described elsewhere.¹⁹ The mass flow controllers (Brooks) were used to control the gas flow from the respective cylinders N₂, O₂ and CO₂. The reactor was placed in a tubular furnace with a uniform heating zone of 4 cm and temperature of the furnace was controlled using Radix 6400 temperature controller. A K-type thermocouple placed in a thermowell over the catalyst was used to measure the catalyst bed temperature. The flow rate of the reaction gas mixture was 25 mL/min (1:5:19, CO:O₂:N₂) and the calculated GHSV was 30000 cm³g_{cat}⁻¹h⁻¹. The conversion reported here is carried out in the steady state where the catalyst is ramped at 2 °C/min and held at various temperatures for 10 minutes of equilibration. After that data was checked for consistency by noting the conversion at 5 min interval (twice) at the specific temperature. The reactor outflow was analyzed using a gas chromatograph equipped with online gas sampling valve, 91.44 cm molecular sieve 13x column and thermal conductivity detector (TCD). The catalytic test runs were carried out before and after hydrogen pretreatment from room temperature to 300 deg.

Prior to the catalytic test, the Au@silica core shell catalyst is pre-treated under flowing hydrogen gas without any diluents for 1 hour at 400 °C with a ramping rate of 1 °/min.

2b.2 Results and discussions

2b.2.a Structural characterization:- UV-Vis and x-ray diffraction analysis

The formation of colloidal gold nanoparticle is clearly evident from the visible colour change of the gold solution from pale yellow to wine red, which is further confirmed by the liquid state UV-Visible spectral analysis. From figure.2b.1a it is evident that gold nanoparticles of size around 8-12 nm is formed as a mild broad peak at 518 nm is present in the UV-Vis spectra of the gold colloid and after the silica encapsulation step a red shift is visible with a peak value 525 nm. In our system, the red shift in peak position can be correlated to the change in refractive index of the surrounding medium (silica in this case) after the encapsulation step, rather than increase in particle size during encapsulation. Further, the wide angle x-ray diffraction analysis clearly indicates the formation gold nanoparticles in the face centered cubic (fcc) lattice in the amorphous silica material (Figure.2b.1b) in our core shell nanostructured Au@silica after the calcination of 500 °C for 6 hours.

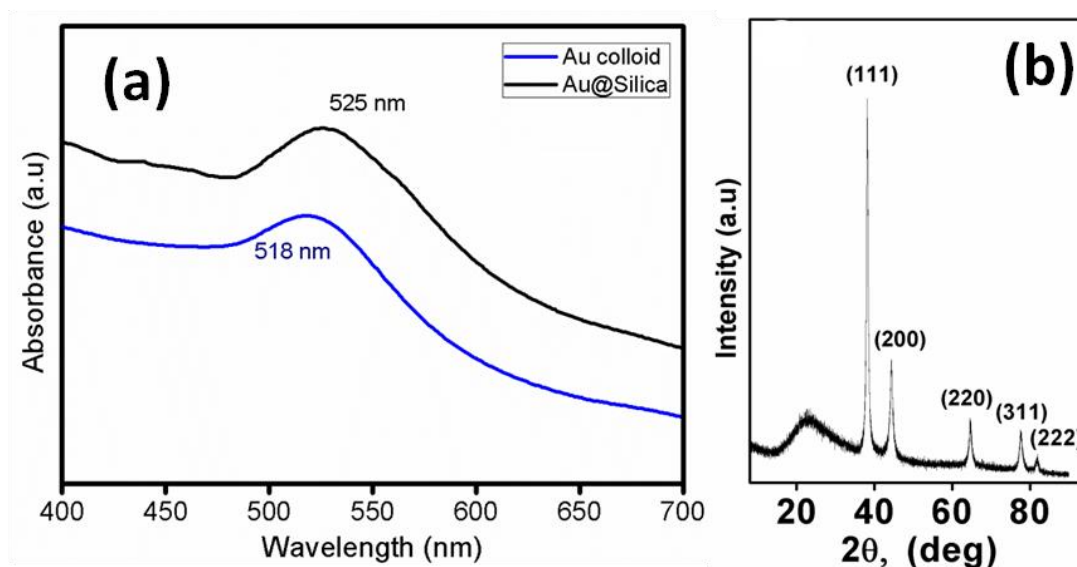


Figure.2b.1 (a) liquid state UV-Vis spectral data of the gold colloid and the colloid after silica encapsulation and (b) the wide angle X-ray diffraction analysis data of the Au@silica sample calcined at 500 °C. The peaks corresponding to the fcc gold nanoparticles are indexed.

2b.2.b. Textural characterisation:- Surface area analysis

The calcined core-shell nanostructures were subjected to the BET analysis where Au@silica core-shell nanocatalyst gave exceptionally high surface area values of 900 m²/g with a pore volume of 0.96 cc/g. The isotherm obtained from the surface area analysis showed type IV isotherm with H4 hysteresis loop. The smaller hysteresis loop at higher partial pressure region indicates the presence of inter connected pore systems with variable pore size or narrow pore opening. Still, the plateau ranging from relative pressure values approximately 0.35 to 0.85 indicates the presence of reasonable amount of uniform mesopores. Further, the sudden uptake of nitrogen in the lower partial pressure values indicates existence of a minute portion of micropores within the core-shell system, which could possible come from the pore shrinkage happen during the high temperature calcination step.

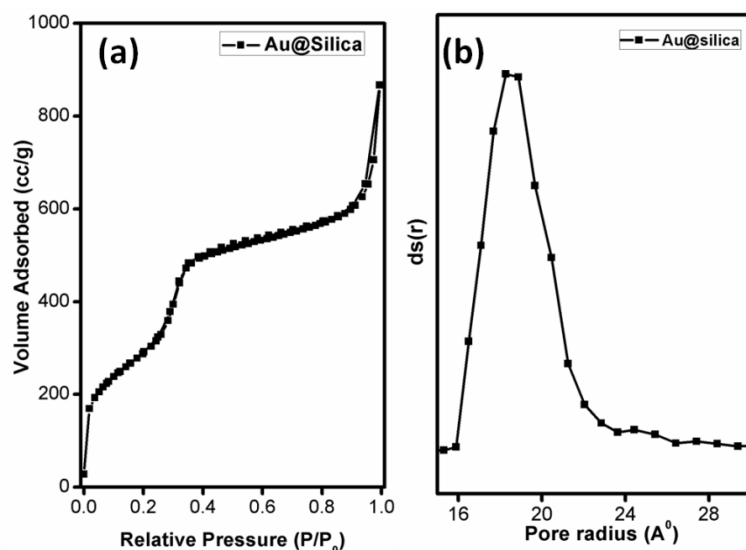


Figure.2b.2 Surface area (a) and pore size distribution (b) analysis profiles for the calcined Au@silica core-shell nanostructures

2b.2.c Microscopy analysis:- Scanning electron and transmission electron microscopy

The formation of core-shell morphology in our Au@silica nanostructures is directly confirmed by the scanning electron microscopy (SEM) analysis. The 3D spherical morphology without any coalescence is clearly seen in the SEM image represented in Figure.2b.3, It should be noted at this point that the 3D morphology without any trace of bigger gold nanoparticles is confirmed from the SEM analysis.

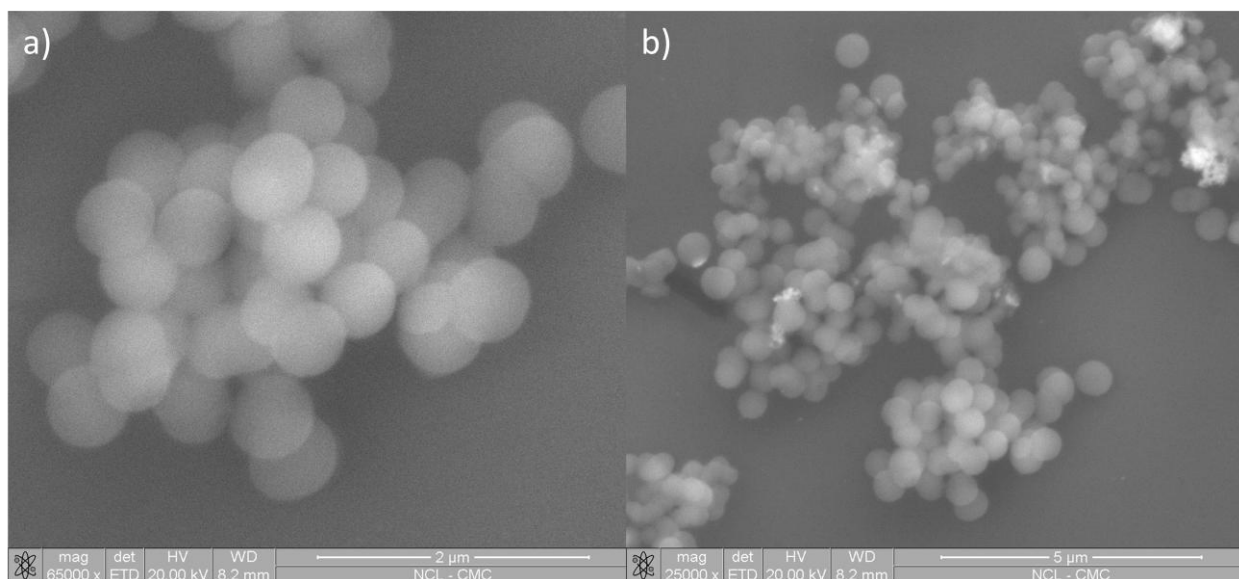


Figure.2b.3 Scanning electron microscopy analysis of the core-shell nanostructured Au@silica catalysts under different magnifications (a) 2 μm and (b) 5 μm

In order to understand the particle size along with the shell thickness, high resolution transmission electron microscopy analysis of our catalysts has been carried out further. It is very clear from figure.2b.4 that the core shell morphology is intact after calcination at 500 °C for 6 hours with a gold core size of 8-12 nm and an average shell thickness of approximately 15-20 nm. It is evident from the TEM images that individual nanoparticles are separated from each other by a dense and highly porous silica shell, thus restricting migration of the gold nanoparticles to a considerable extent and hence avoiding sintering during the high temperature calcination. The highly porous nature results from the removal of the CTAB capping agent/structure directing agent during the calcination step and the resultant porosity leads to higher surface area with better pore volume (see figure.2b.2).

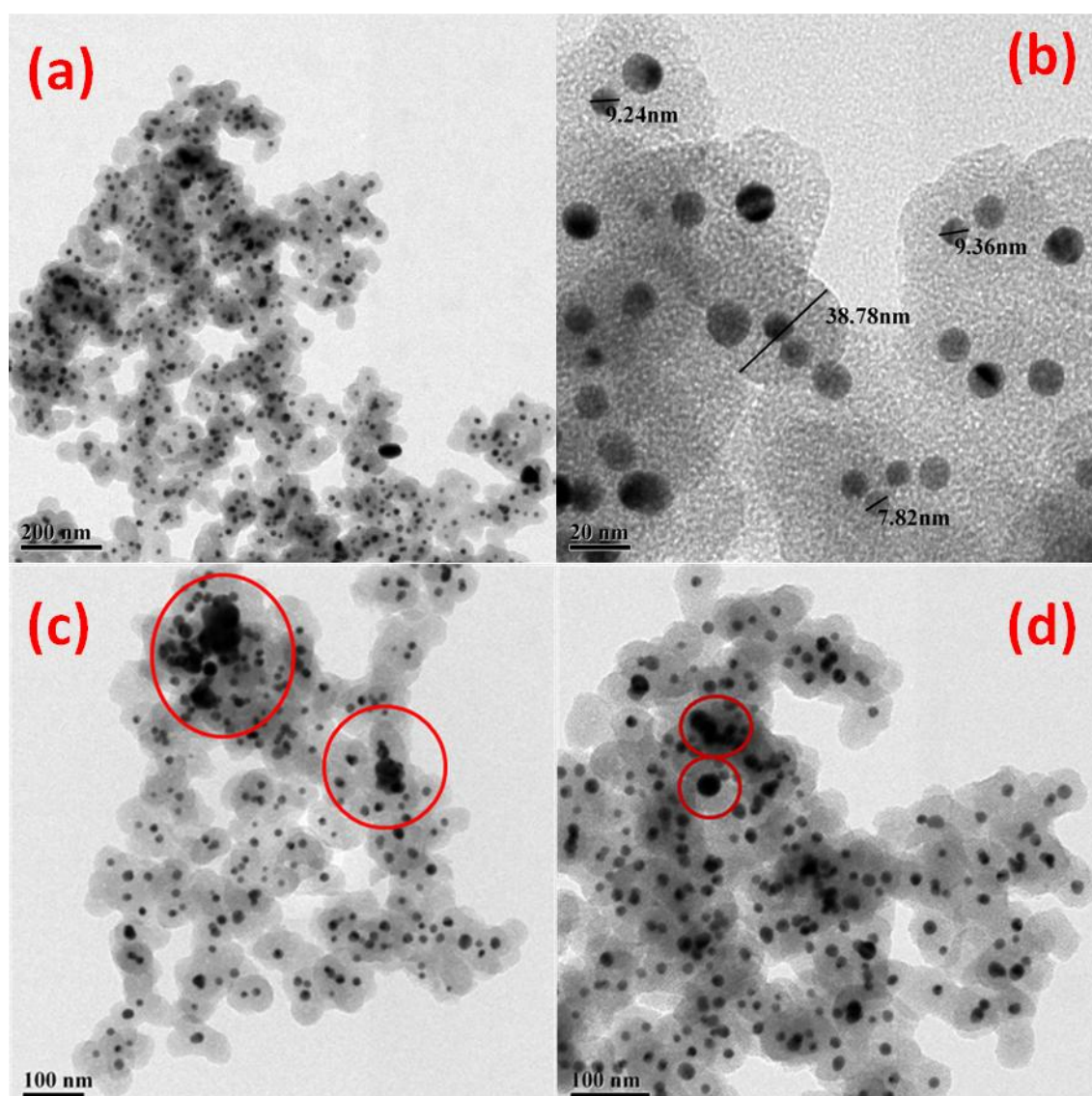


Figure.2b.4 Transmission electron microscopy images of the calcined Au@silica core shell nanostructures under various magnifications; (a) and (b) representing the clearly showing the presence of gold core with 8-12 nm size with in a porous silica shell, (c) and (d) representing the presence of larger gold nanoparticles outside the silica shell

The TEM image clearly exemplifies the success of the synthesis protocol adapted here in developing sinter resistant core-shell nano-architectures (Figure.2b.4a and b). It should be noted at this point that larger gold nanoparticles of size 30-40 nm were visible which are falling outside the silica spheres, and under goes sintering during the calcination step. These bigger particles are actually contributing to the larger diffraction and are clearly visible in our x-ray diffraction analysis (see Figure.2b.1b). Our preliminary understanding about the gold-silica system for CO oxidation (see Chapter.2a.3) provoked us to do the pre-treatment under flowing hydrogen gas. For the present study, the hydrogen pre-treatment is carried out at 400 °C for 1 hour under pure hydrogen stream.

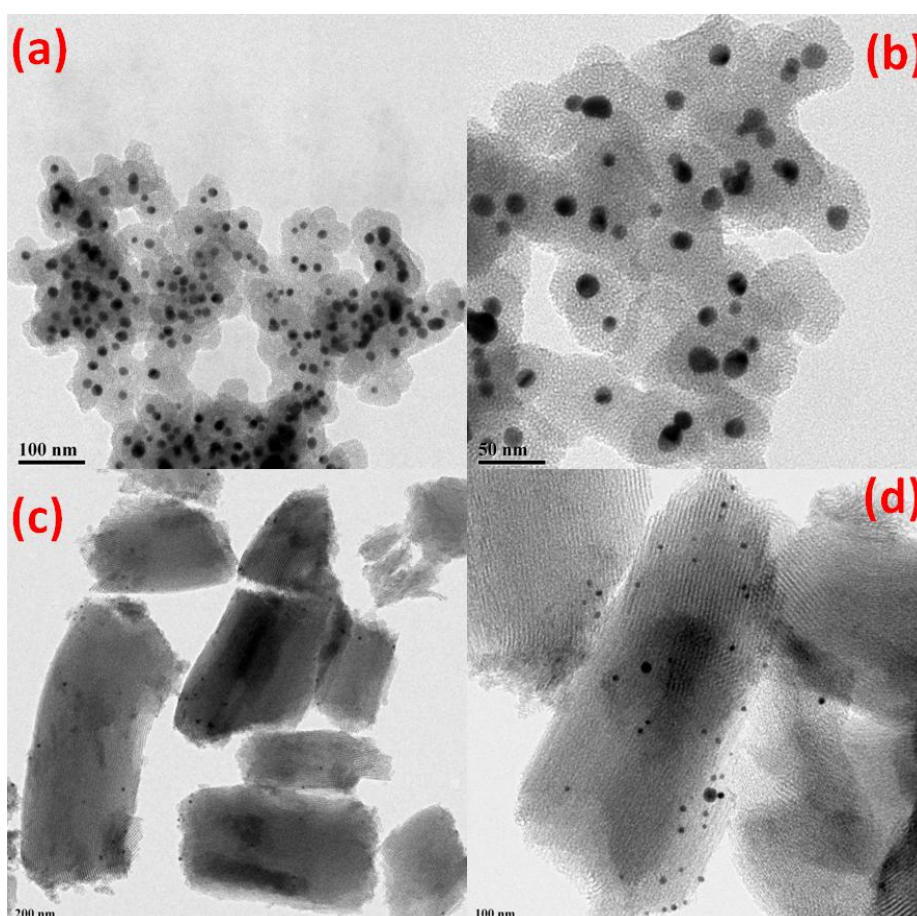


Figure.2b.5 TEM images of the sample after reduction pre-treatment of Au@silica (a) and (b), and that of the calcined sample of Au colloid deposited on SBA-15 (c) and (d)

Further in order to understand the positive impact of our system against sintering during the reaction as well as catalytic test, Au-SBA-15 catalyst is synthesised by colloidal deposition of the gold colloid on commercial SBA-15 support. This supported catalyst Au-SBA-15 is also thoroughly characterised using TEM (figure.2b.5c and d).

It is evident from the above characterisations that the synthesised material is having a core shell nanostructure where the gold core is easily accessible through the porous silica shell and the morphology is intact even after high temperature calcination or pre-treatment under reactive gas like hydrogen. This points to the applicability of this material as a heterogeneous catalyst. To prove the sinter resistance capability of such core shell architectures, CO oxidation reaction has been carried out over our Au@silica core shell nanocatalyst in an oxygen rich environment and the catalytic test results are given in details in the next section.

2b.3 Catalytic Test Results:- CO oxidation reaction

The presence of large surface area with large pore volume and pore size makes our system an attractive choice for heterogeneous reactions where heat and mass transfer limitations play a pivotal role in overall catalytic activity. In the case of CO oxidation over a gold-silica system the widely discussed sintering under reaction stream is kept in mind while making the catalysts and thus the core shell morphology is designed. Further, the size dependency of gold nanoparticles also needed to be revisited for the conventionally considered model CO oxidation reaction on a gold-silica system, hence gold nanoparticle of size 8-12nm is selected for the current study. Based on the conventional heterogeneous catalytic backgrounds on a gold silica system for CO oxidation, the chosen gold nanoparticle size range as well as the considered support is least favourable for the reaction.

Still, the calcined Au@silica catalyst was found to be active from approximately 150 °C reaching a maximum of around 45 % conversion at 300 °C. The catalyst after subjecting to a mild reduction in flowing H₂ at 400 °C was further tested for CO oxidation. It is interesting to note that these nanocatalysts having gold core of 8-12 nm size, gave around 10% conversion at room temperature itself in the first cycle with overall conversion reaching around 90% at 300 °C (Figure.2b.6). The steady state CO conversion for second and third cycle of the same catalyst without any further catalyst regeneration or pre-treatment is also shown in Fig.2b.6. The observed catalytic activity is remarkable as it gave 40-45 % conversion from second cycle onwards at room temperature which reached 100 % at 250 °C. A similar observation was obtained in terms of conversion in the consecutive cycles when a different batch of the catalysts is used for the current study. The origin for this trend is not very clear at the moment and needs further investigation. The shape of the CO oxidation curve at low temperature regime in the second and third cycle is interesting though not surprising. The conversion value of 44 % at room temperature increases to 65 % at 60 °C and decreases to 59 % at 80 °C.

On further increasing the temperature there is a steady increase in the conversion reaching almost 100 % at 250 ° C.

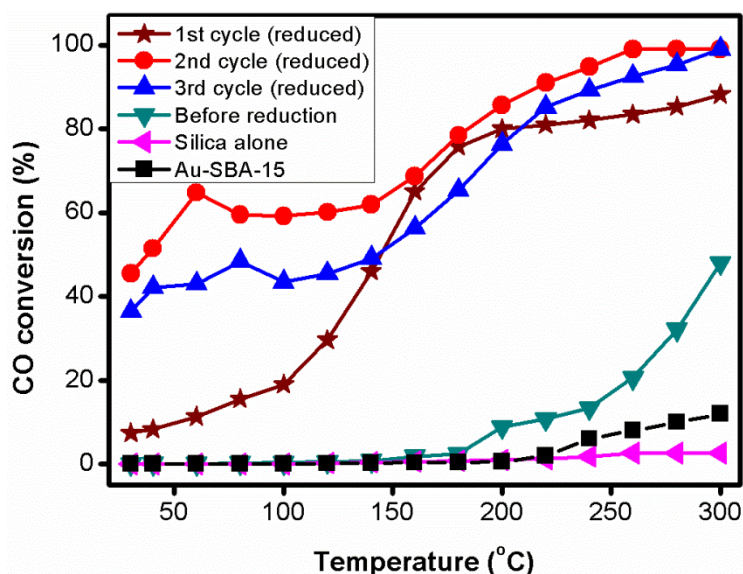


Figure.2b.6 CO oxidation reaction profile as a function of temperature, For clarity Au-SBA-15 sample also included in the figure

This type of behaviour in the low temperature regime is previously observed on Au-Silica based systems.²⁹⁻³¹ Recently, Qian et al showed CO oxidation from gold nanoparticles of approximately 10 nm supported on silica.²⁵ The volcano type behaviour observed at low temperature regime in this instance was argued to be due to the temperature dependent competition between surface reaction and desorption of weakly chemisorbed species. This also suggested the involvement of weakly chemisorbed species in the mechanism of low temperature CO oxidation. From CO oxidation curve shown in Figure.2b.6 it is clear that the performance of the catalyst is almost retained even during the 3rd cycle which exemplifies the durability of the catalyst. The sustained catalytic activity even during the 3rd cycle of CO oxidation could largely be attributed to the stability of the Au nanoparticles towards sintering against temperature and onstream reactive gases. TEM carried out to investigate the morphology of the spent catalyst after the third cycle of CO oxidation revealed exceptional stability of the catalyst retaining the same morphology and size of the particles (Figure.2b.7) Whereas, a completely collapsed morphology is observed for the SBA-15 deposited gold colloidal nanoparticles after the first cycle of CO oxidation itself

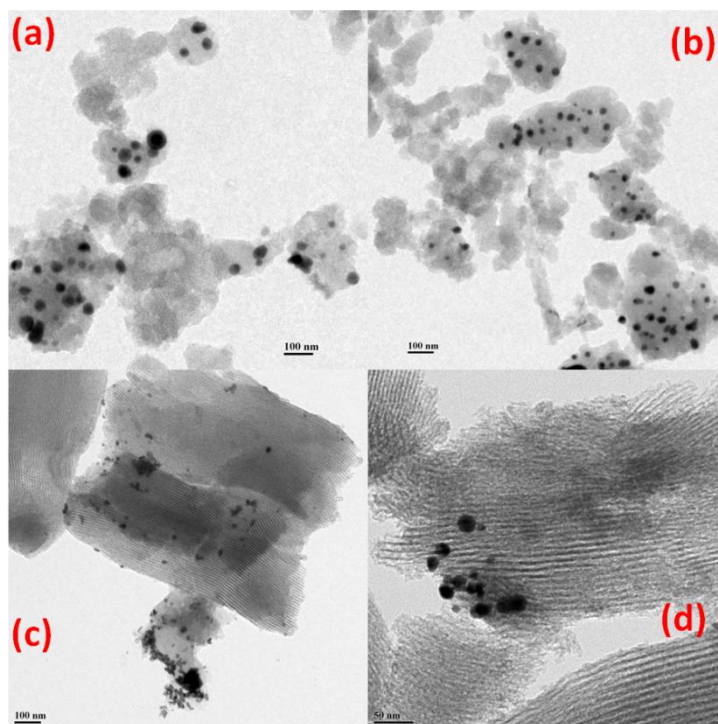


Figure.2b.7 Transmission electron microscopy image of the spent catalysts Au@silica after 3 cycles of CO oxidation (a and b) and that of Au-SBA-15 after 1 cycle of CO oxidation (c and d)

Gabaldon and Datye have carried out a systematic STEM study on the stability of gold nanoparticles on various mesoporous silica systems and showed sintering during the reaction especially on those supported on 3-D architectures.³² The free mobility of the gold nanoparticles on a silica support resulting in sintering is more or less restricted due to the confinement effects in our case. Another striking feature of this catalyst is the room temperature CO oxidation activity of Au nanoparticle which is approx 8-12 nm size on silica which is considered as an inactive support. It is known from the previous CO oxidation studies on gold/silica system that this is well above the optimum size of an active CO oxidation catalyst.³³ The studies carried out on nanoparticles of size ranging between 8-10 nm have been reported in literature.^{29, 34} Haruta et al demonstrated reactivity of 8 nm Au/SiO₂ catalyst deposited by impregnation method showed conversion of only 5 % at 550 K reaching 55 % at 700 K.³⁴ A similar trend in reactivity has also been reported by Qian et al for a particle size of 10 nm supported on SiO₂. Mou and co-workers also carried out CO oxidation on different silica supports like MCM41, MCM48 and SBA15 where the particle size of approximately 8-10 nm showed a conversion of 40-50 % at 80 °C.³⁵ In contrast, Au nanoparticles of approximately 6 nm supported on silica with considerable amount of E`centers were found to catalyse CO oxidation with 42 % conversion at 40 °C which is close

to the conversion achieved at room temperature during the second cycle.³⁶ Using electron paramagnetic resonance (EPR) technique a mechanistic understanding on gold nanoparticle assisted oxygen vacancy formation along with the role of 6-20 nm Au particle for the generation of oxygen vacancies on silica surface has been reported. The resulting catalyst is found to generate superoxide species there by ruling out a gold alone mechanism for CO oxidation. Considering these facts a possible explanation for the excellent room temperature activity in our core shell system could be the presence of considerable amount of oxygen vacancies created during the reduction step in the nano pore channels which can facilitate the activation of oxygen.

2c. Au@Ti-SiO₂ core shell nanocatalyst and its CO oxidation catalysis

The core shell Au@silica system which is discussed in chapter 2b helped us to conclude that silica is no longer an inert support for gold based catalysts, specifically for CO Oxidation even if the size range falls above the optimum range. This conclusion provoked us to further explore this area by incorporating a hetero atom and thereby introducing reducibility in an otherwise non reducible silica support and thus one can expect enhanced catalytic activity for CO oxidation. Keeping this idea in our mind Ti atom is chosen to selectively incorporate in the silica matrix to make Au@Ti-SiO₂. The synthesis procedure along with its complete characterisation as well as catalytic test results are given in detail in the following section.

2c.1. Experimental

2c.1.a. Synthesis of core shell Au@Ti-SiO₂ nanocatalysts

The synthesis of our core shell nanocatalysts is based on a modified seed mediated gold nanoparticle synthesis followed by Ti-SiO₂ encapsulation. In a typical procedure, gold nanoparticles are synthesized by seed mediated method and stabilized by cetyltrimethyl ammonium bromide (CTAB) capping. The applicability of CTAB as a structure directing agent is further utilized in the shell encapsulation process. The different steps involved in the synthesis of our Au@Ti-SiO₂ catalyst (from here onwards AST) are;

2c.1.b. Synthesis of gold nanoparticles by Seed mediated method:-

Preparation of gold seed

65 ml aqueous solution containing 2.5×10^{-4} M HAuCl₄ (Sigma Aldrich, 99.9%) and 2.5×10^{-4} M trisodium citrate (Alfa Aesar) was prepared in a conical flask. Next 2 mL of ice –cold freshly

prepared 0.1M NaBH₄ (Spectrochem 96%) solution was added to the solution while stirring. The pink colour of the resulting solution shows the formation of nano gold.

Preparation of growth solution

200 ml of the aqueous solution (2.5×10^{-4} M) HAuCl₄ mixed with 6gm of Cetyl trimethyl ammonium bromide (Spectrochem 98%) was heated until the solution turned a clean orange colour, cooled to room temperature and used as the growth solution.

The growth solution is then treated with 0.1 M (1.3 ml) of ascorbic acid (Spectrochem 98%) and added to the gold seed solution while stirring, the solution turns into wine red and the stirring continued for another 10 minutes.

2c.1.c. Silica encapsulation

In order to control the silica thickness the total solution is divided into different batches and silica encapsulation is carried out. In a typical procedure 50 ml of the above solution is stirred for 24 hrs after mixing with 20 ml of ethanol, 0.6 ml ammonia solution and 0.05 ml tetraethyl orthosilicate (Merck).

2c.1.d. Modification of silica matrix with Titanium:-

The titanium doping on silica matrix was carried out by modifying the procedure reported by Guttel et al.³⁷ Typically 3 μ l (AST1), 15 μ l (AST5) and 30 μ l (AST10) of titanium isopropoxide dissolved in 2.5 ml of ethanol is used as the titanium precursor. For Ti incorporation, 0.5 ml of the above prepared precursor solution is added in to the silica encapsulated gold sol under vigorous stirring; and stirring continued for 30 minutes.

The above colloid was centrifuged at 10000 rpm for 10 minutes and the residue washed with Millipore water twice. It is then extracted using ethanol kept for drying over night at 50 °C and finally calcined at 500 °C for 6 hrs.

2c.1.e. Catalytic test:- CO oxidation

The applicability and the stability of the synthesized materials for catalytic applications were tested by carrying out CO oxidation reaction from room temperature upto 300 °C. The catalyst tests were carried out under atmospheric pressure in a fixed bed reactor of diameter 14 mm. More details of the reactor is described elsewhere.¹⁹ The mass flow controllers (Brooks) were used to control the gas flow from the respective cylinders N₂, O₂ and CO. The

reactor was placed in a tubular furnace with a uniform heating zone of 4 cm and temperature of the furnace was controlled using Radix 6400 temperature controller. A K-type thermocouple placed in a thermowell over the catalyst was used to measure the catalyst bed temperature. The flow rate of the reaction gas mixture was 25 mL/min (1:5:19, CO:O₂:N₂) and the calculated GHSV was 37500 cm³g_{cat}⁻¹h⁻¹. The conversion reported here is carried out in the steady state where the catalyst is ramped at 2 °C/min and held at various temperatures for 10 minutes of equilibration. The data was checked for consistency by noting the conversion at 10 min interval (twice) at the specific temperature. The reactor outflow was analyzed using a gas chromatograph equipped with online gas sampling valve, 91.44 cm molecular sieve 13x column and thermal conductivity detector (TCD). The catalytic test runs were carried out before and after hydrogen pre-treatment from room temperature to 300 °C.

2c.2 Results and Discussions

2c.2.a. Structural characterization

The synthesis of gold nanoparticles by seed mediated method has been followed at each stage by UV-Vis spectroscopy. The various plasmonic changes during synthesis as well as Ti-SiO₂ encapsulation is clearly observable in the figure.2c.1a; where curve a shows the plasmon band at 515 nm due to the formation of Au seed (size ~ 5 nm). This peak red shifts to 520 nm after the growth of Au nanoparticles which clearly indicates the increase in size of the particles. Curve c and d corresponds to UV-Vis spectra obtained after silica and Ti-SiO₂ encapsulation. The sample denoted as AST1 represents the Au-Ti-SiO₂ catalyst where 1wt% of titanium loading was attempted. Synthesis of AST5 and AS10 where 5 and 10 wt% of titanium precursor were used is also attempted in the current study. The ICP-AES analysis results were surprising as it showed a considerable variation from the intended values (shown in parenthesis) of 0.97 (1), 3.5 (5) and 4.5(10) wt%. Since our synthesis strategy involves centrifugation followed by washing in millipore water, the loss of some amount of titanium is expected. In spite of this almost 100% of Ti was able to get incorporated in the case of AST1 whereas around 45% in the case of AST10. The red shift in the peak position while silica encapsulation and titanium doping in UV-Vis spectrum is mainly because of the change in dielectric constant of the surrounding medium.³⁸

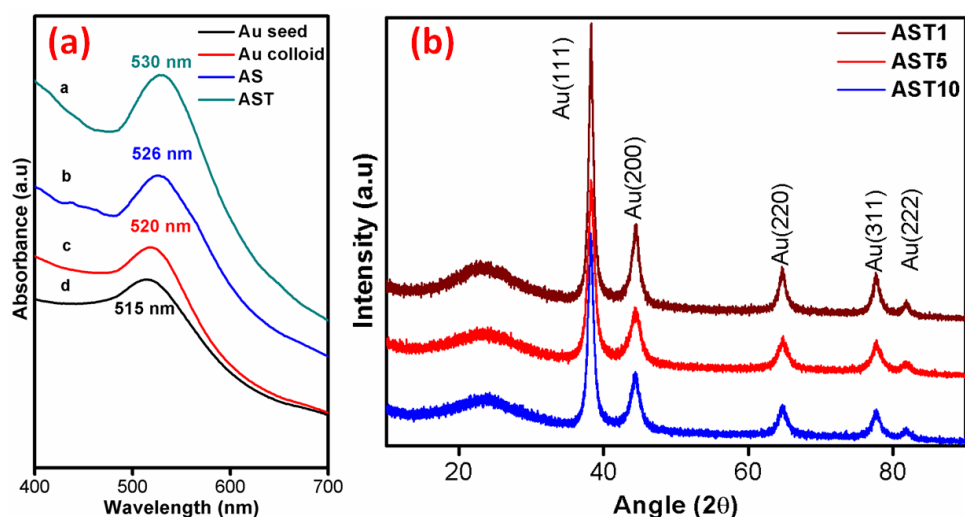


Figure.2c.1 Liquid state UV-Vis spectra (a) of gold nanoparticle synthesis by seed mediated synthesis and subsequent encapsulation and the wide angle X-ray diffraction pattern (b) of the core shell nanostructures with various Ti loading

The powder XRD of the synthesized samples (Figure.2c.1b) did not show any peak corresponding to the crystalline phase of titania³⁹ indicating incorporation of titanium within the silica matrix and not existing as phase segregated SiO₂ and TiO₂ physical mixture. The existence of gold in the fcc phase⁴⁰ is evident from the XRD analysis with an average crystallite size calculated from Scherrer formulae being 9 nm (for both 1AST and 5AST) and 25 nm (for 10AST). In order to understand the chemical stability of the amorphous Ti-SiO₂ shell AST1 catalyst is calcined at 800 °C for 6 hrs and still no evidence for the crystalline phase for titania or silica. Hence one can confirm that the synthesized materials are highly amorphous and rule out phase segregation during synthesis of AST1. Further, to check the formation of amorphous phase segregated system in our Au@Ti-SiO₂ catalyst the samples are tested under a solid state UV-Vis spectrophotometer to check the formation of TiO₂ in the matrix since UV-Vis sensitivity is more when compared to the x-ray diffraction technique in the current case. One can clearly observe (from Figure.2c.2) a broad peak corresponds to the anatase phase of titania centered around 335 nm on increasing the Ti loading in our catalyst, specifically in AST10 where the intended loading was 10% Ti. For all the Ti incorporation studied a peak obtained at 225 nm associated with a distorted geometry of titanium in mesoporous Ti-SiO₂.⁴¹ It should be noted that for TS1 like materials a sharp absorption is observed at 220 nm⁴²⁻⁴³ where as in our case this peak is broader and shifted to 225 nm indicating more heterogeneous co-ordination of Ti⁴⁺ and most probably present in tetrahedral/octahedral environment. As the Ti loading increases to 5 and 10 % an intense and

broad absorption peak at 335 nm is visible which is assigned to isolated TiO_2 clusters.⁴⁴ Thus with higher Ti precursor concentration instead of isomorphic substitution of Ti in the lattice, the TiO_2 particles are preferred which could potentially influence the overall morphology of the synthesized materials (for more explanations see section 2c.5).

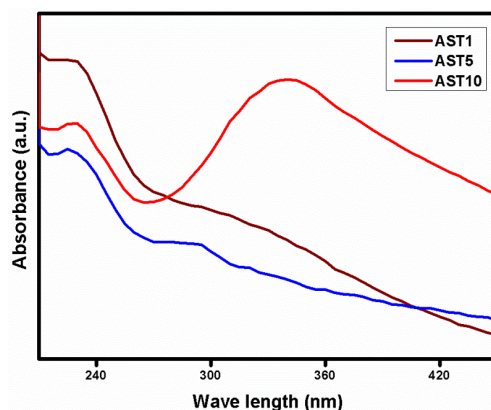


Figure.2c.2 Solid state UV-Vis analysis spectra of the various Ti-loaded core shell nanocatalysts after calcinations

Similarly, the FTIR and Raman spectroscopy analysis (Figure.2c.3a and b respectively) reveals the successful incorporation of Ti in the silica matrix for the AST series catalysts.

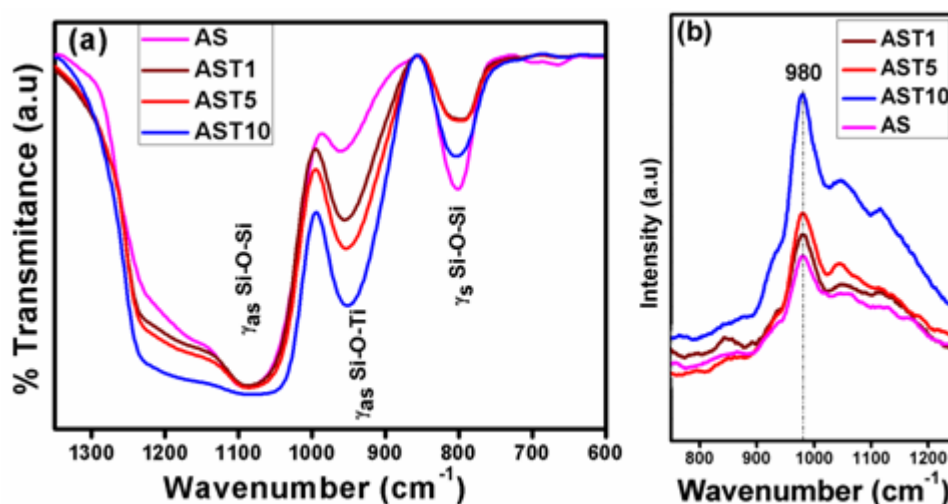


Figure.2c.3 FTIR (a) and Raman under a 633 nm laser source (b) of the various AST catalysts. For clarity the Au@silica catalysts is also given in the figure.

The vibrational analysis of the samples shown in Fig.6a gave further insight into the bonding characteristics of our core-shell system. For clarity gold@silica core shell system is also included in the figure. The 960 cm^{-1} peak is originally attributed to the stretching vibration of

the Si-O- group bonded to hydrogen or titanium.⁴⁵ More over the increase in the intensity of this band as the titanium loading increases from AST1 to AST10 in our case clearly manifests the incorporation of tetra coordinated titanium in the silica matrix. Based on a quantum chemical (SCF) calculations de Man and Sauer⁴⁶ previously reported that 960 cm⁻¹ peak can be interpreted as an anti-symmetric stretching mode of the Si-O-Ti bond in the Ti(OSi(OH)₃)₄ unit where Ti is tetra coordinated. Si-O-Si symmetric and asymmetric stretch at ~ 800 cm⁻¹ and 1080 cm⁻¹ are also clearly identified from our IR analysis of the sample with a decrease in intensity of 800 cm⁻¹ with increasing Ti loading. A similar trend is observable in the Raman spectral analysis of our samples when a visible laser source 514 nm was used. Deo et al has investigated the substitution of Ti in silicate lattice and observed enhancement in the scattering at 970 cm⁻¹.⁴⁷ While this band is essentially due to Si-O vibrations, the enhancement in their intensity is concluded to be due to Si-O-Ti bond formation. Unlike other reported Raman results where 960-970 cm⁻¹ corresponds to the presence of Si-O-Ti linkages,⁴⁷ a slight shift in peak position is observed in our system and it occurred at 980 cm⁻¹ (Fig.8b) with the peak intensity increasing with titanium loading.^{41, 44} The blue shift in the resonance Raman spectra of titanium incorporated silica has been previously reported with an excitation source of 422 nm.⁴⁴ The shift in peak position in our case may be due to the lower titanium loading and the presence of a considerable number of defect sites along with the poor scattering by the amorphous Ti-SiO₂ shell. ²⁹Si nmr analysis of all the samples have been further done to understand the co-ordination environment of the AST series samples, though its applicability is limited since no signature features of Si-O-Ti spectrum.⁴⁸

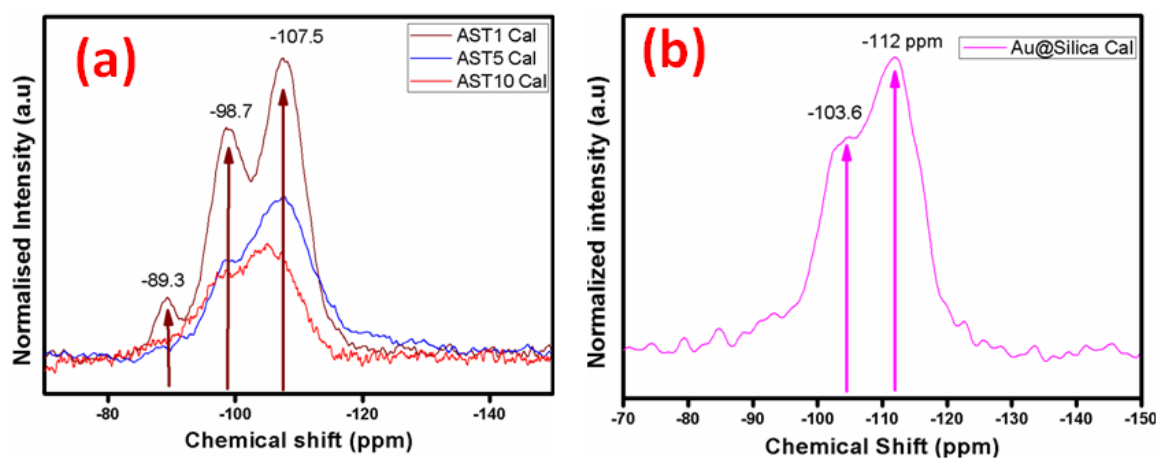


Figure.2c.4 The ²⁹Si NMR spectra of (a) AST series catalyst with various Ti loading and (b) Au@meso-SiO₂ system without any Ti loading

^{29}Si NMR of pure silica material is characterized by signal centered at -110 ppm attributed to Q^4 ($\text{Si}(\text{OSi})_4$) environment and a shoulder at approx -100 ppm for Q^3 silicons $\text{Si}(\text{OSi})_3\text{OH}$ sites. However, it is reported that on titanium incorporation in siliceous matrix results in a considerable broadening of the peaks and an asymmetry towards high field side because of the appearance of new feature at -116 ppm due to Si-O-Ti linkage.^{41, 49-50} The NMR experiments carried out on our sample also showed similar trend. A pure Au@silica catalyst show resonance at -112 ppm and a shoulder at -103.6 ppm which considerably changes its line shape and width on progressive titanium incorporation argued to be due to changes in the Si-O-Si angles in the SiO_4 tetrahedra after Ti incorporation (Figure.2c.4). The chemical identity of various components especially Ti in our core shell systems were examined by XPS analysis (Figure.2c.5). The formation of titanosilicate shell is firmly established by the XPS peaks at 459.6 eV (Ti $2p_{3/2}$) and 465.2 eV (Ti $2p_{1/2}$) which manifests titanium in the tetrahedral arrangement (Ti_{Td}).^{44, 51} The higher binding energy of Ti $2p_{3/2}$ in tetrahedral Ti^{4+} has been previously reported when titanium is well dispersed in silica matrix.⁴⁴ The binding energy of 459.6 eV is significantly different from Ti for instance in TiO_2 which is observed at 458.6 eV.⁵² The shift to the higher binding energy for titanosilicates has been explained by the increase in the inter atomic potentials due to the decrease of the coordination number of Ti and the shortening of the Ti-O bond suggesting the insertion of Ti^{4+} into the tetrahedral site of the silica network.⁵²⁻⁵³

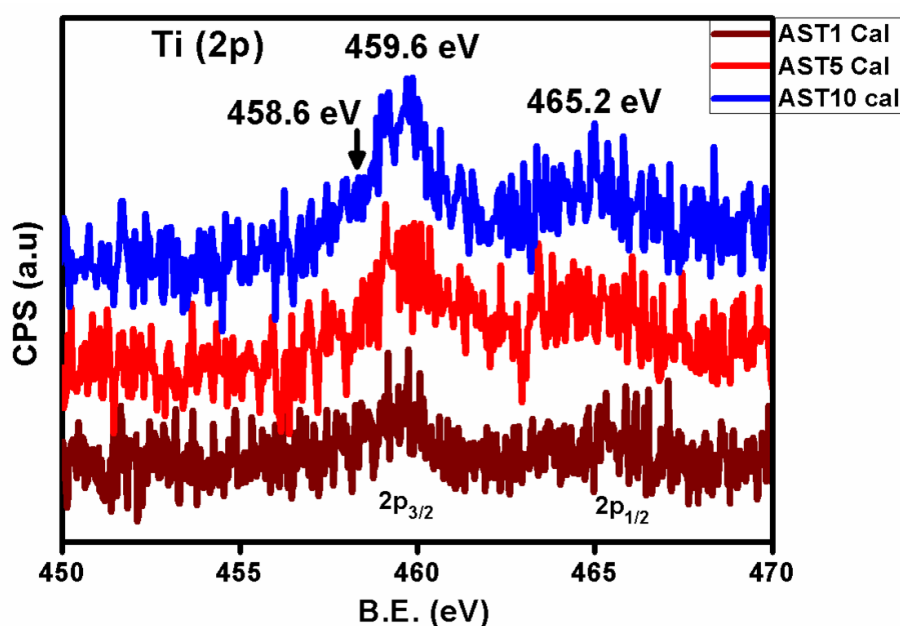


Figure.2c.5 Ti 2p X-ray photoelectron spectral (XPS) analysis profile for the AST series calcined samples

As the titanium loading increases from AST1 to AST10 an obvious increase in the Ti $2p_{3/2}$ XPS core level intensity was observed along with an increase in full width half maximum without marked shift in the peak maxima. A careful observation of AST10 Ti $2p_{3/2}$ shows that the increase in FWHM is related to an asymmetry towards lower binding energy side with possible development of 458.6 eV species (indicated by arrow in Figure.2c.5) corresponding to TiO_2 . Further evidence for the incorporation of titanium in the siliceous matrix is evident from the O 1s spectra of the calcined samples (Figure.2c.6a). The oxygen core level binding energy will decrease when titanium exists as Si-O-Ti in the siliceous matrix and hence will fall between the O 1s binding energy of pure silica (~ 533.5 eV) and pure titania (~ 530 eV).⁴¹ Thus in our case the O1s has a peak maxima centered on 532.6 eV which shows asymmetry and an increase in FWHM as the titanium doping increases. This is understandable as pure titanosilicate shows O1s binding energy centered around 532 -533 eV⁵⁴ with Si-O-Ti linkage feature at 531.7 eV.⁵⁵

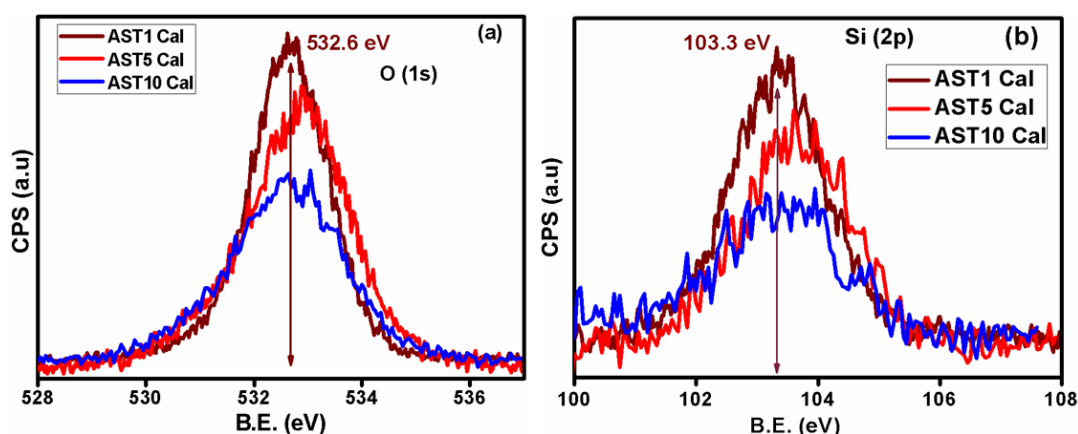


Figure.2c.6 X-ray photoelectron spectral analysis data (a) O 1S and (b) Si 2p of the calcined AST series catalyst.

The O1s spectrum from AST10 is considerably broad with possible contributions from Si-O-Si, Si-O-Ti and to some extent TiO_2 as the peak is observed to be asymmetric towards lower binding energy side. Hence possible phase segregation can be expected at higher Ti loading evident from the XPS, which is matching with the solid state UV-Vis observation discussed earlier. Concordantly the FWHM values of the O1s peak varies with the titanium doping and in our case the FWHM values are 1.7 (AST1), 2.1 (AST5) and 2.8 (AST10). Moreover the separation of 5.9 eV between Ti $2p_{3/2}$ and Ti $2p_{1/2}$ peaks and the shift in the binding energy of Si 2p towards the lower value when compared with pure silica (Figure.2c.6b) also

exemplifies the tetra co-ordination of titanium in the silica matrix.⁵⁶⁻⁵⁷ As a best practice all the calcined AST catalyst will be pre-treated at 400 °C under flowing hydrogen before catalytic test. In order to have a prior knowledge about any of the change in chemical composition of the actual catalysts, a reduced AST1 sample XPS analysis also carried out, so that any possible improvement in catalytic activity if observed can be precisely explained. A comparison of the Ti 2p xps spectra of the calcined and reduced AST1 sample is represented in Figure.2c.7

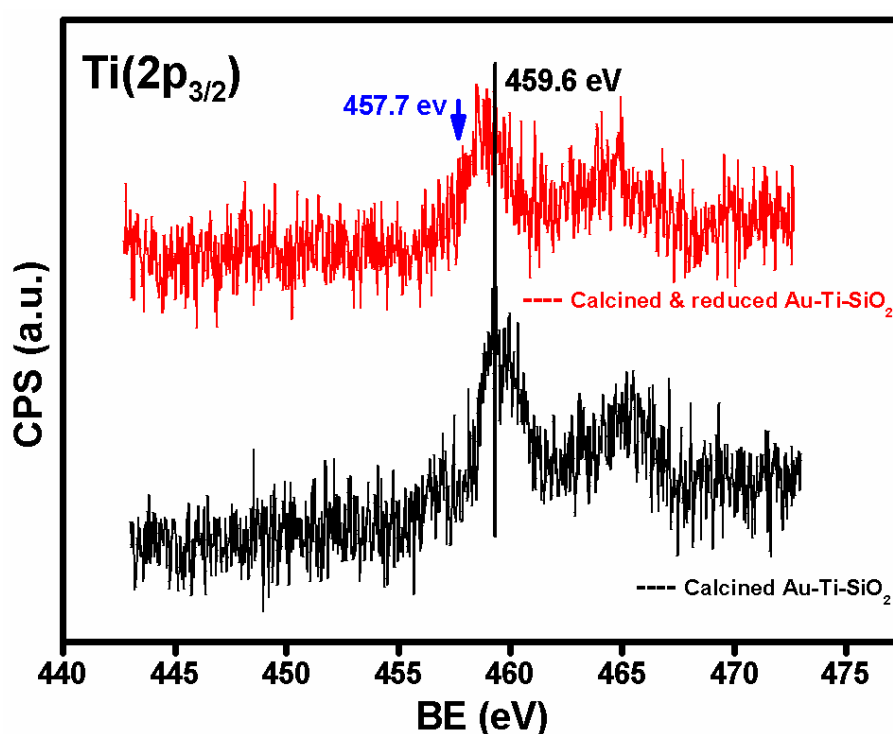


Figure.2c.7 Ti 2p XPS spectra of the nanocatalysts AST1 before and after hydrogen pre-treatment

The XPS spectra of the reduced sample showed an observable decrease in the binding energy of Ti 2p core level from 459.6 to 458.8 eV with a shoulder at 457.7 eV (Figure.2c.7) which matches well with the value for Ti 2p_{3/2} reported in literature for the existence of Ti³⁺ in titania.⁵⁸ In our case the reduction process at 400 °C can result in the formation of Ti³⁺ which will effectively generate oxygen vacancies in our Au@titanosilicate nanocatalysts. These oxygen vacancies are considered to play a pivotal role in determining the reactivity of supported gold catalysts.

2c.2.b Textural characterization

The synthesized catalysts were further subjected to surface area measurements and the surface area and pore size distribution curves from the three catalysts are shown in Figure.2c.8 which clearly shows the presence of a considerable amount of microporosity even though the three samples resemble type-IV isotherm. The surface area values increases with titanium loading and values obtained were 913 m²/g (AST1), 1020 m²/g (AST5) and 1072 m²/g (AST10) respectively. The pore size distribution by DFT method points out that there is not much change in the average pore radius showing a bimodal distribution with pores sizes of 8 Å and 14 Å.

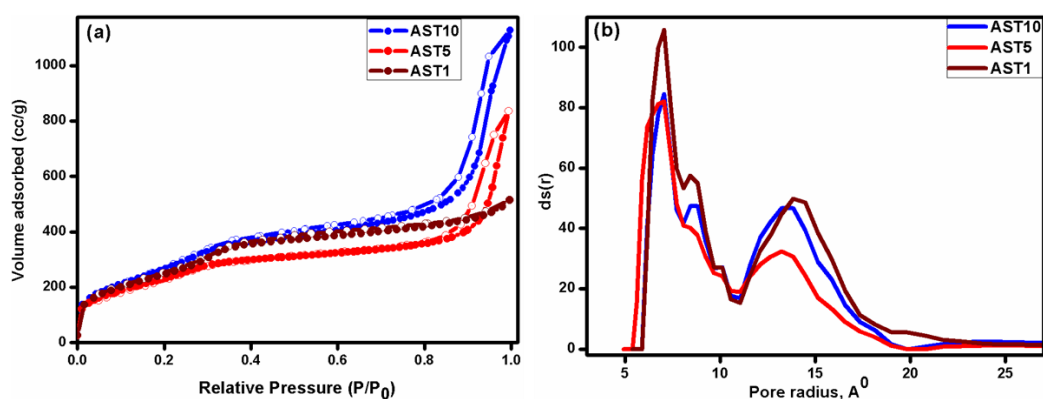


Figure.2c.8 The surface area (a) and pore size distribution (b) analysis of the calcined AST samples

The high nitrogen uptake in the case of AST5 and AST10 at higher partial pressures of nitrogen gas can be attributed to the presence of bottle neck type pore distribution within these systems that connects micropores with some of the larger mesopores. The bottle neck effect observed with titanium doping is reported in literature, which may be due to the disordered structural or morphological formation of titanosilicate with higher Ti incorporation as in our case.⁵⁹

2c.2.c Microscopy Analysis

Finally to understand the success of our synthesis methodology in generating the core-shell morphology like previously discussed (Chapter.2b) Au@silica system, all the synthesized materials thoroughly characterized using TEM and SEM. The formation of core shell morphology with a gold core of size ranging from 8-12 having an average shell thickness of 15 nm for AST1 is clearly evident from TEM (Figure.2c.9). Moreover, several light color contrast spots in the high resolution image (Figure.2c.9d) indicates the presence of pores in

the silica matrix generated during the removal of the CTAB ligand during the calcination step.

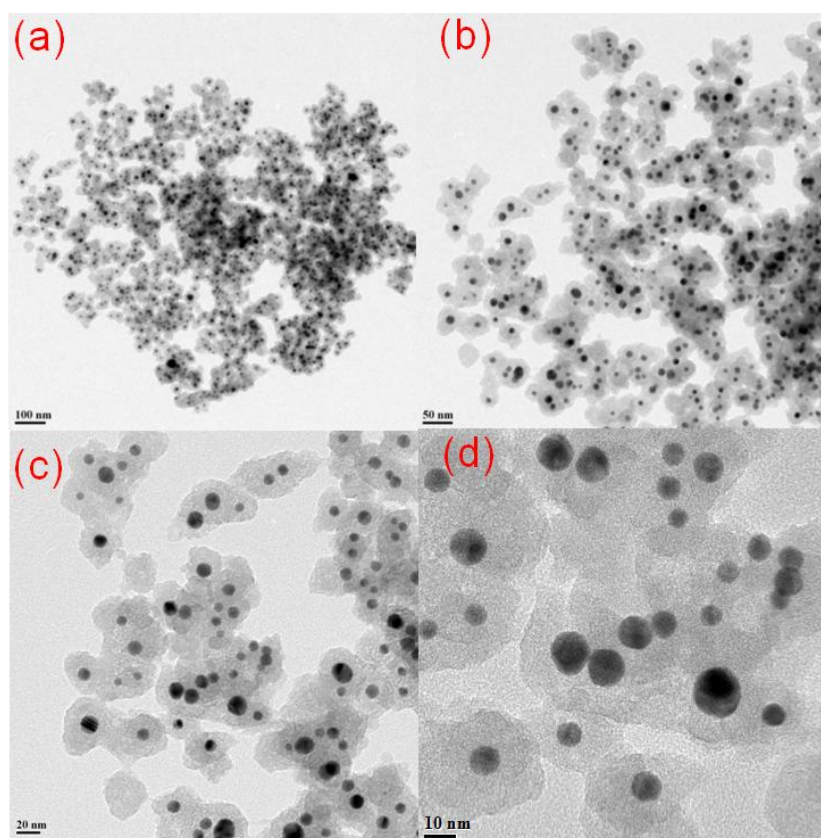


Figure.2c.9 Transmission electron microscopy analysis of the AST1 calcined sample with various magnifications

The HRTEM analysis of AST5 and AST10 is represented in Figure.2c.10. It is interesting to note that the core shell morphology was more or less retained in AST5 which starts losing this architecture when the concentration of titanium in the silica matrix increases beyond 5 wt%. A careful examination of the TEM images Figure.2c.10 (c and d) shows that the core shell morphology is more or less lost when the titanium wt% is beyond 5. Also it was interesting to note from TEM that going from AST1 to AST10 resulted in an increase in Au particle size with AST10 giving particle size around 25-30 nm. This is in agreement with the particle size obtained from Debye – Scherrer equation for AST10 catalyst. Thus it can be concluded that as the core-shell organization is lost the particles are more susceptible towards sintering. Hence, our synthesis strategy is restricted up to the loading of 10 wt% Ti in the core shell Au@Ti-silica catalyst.

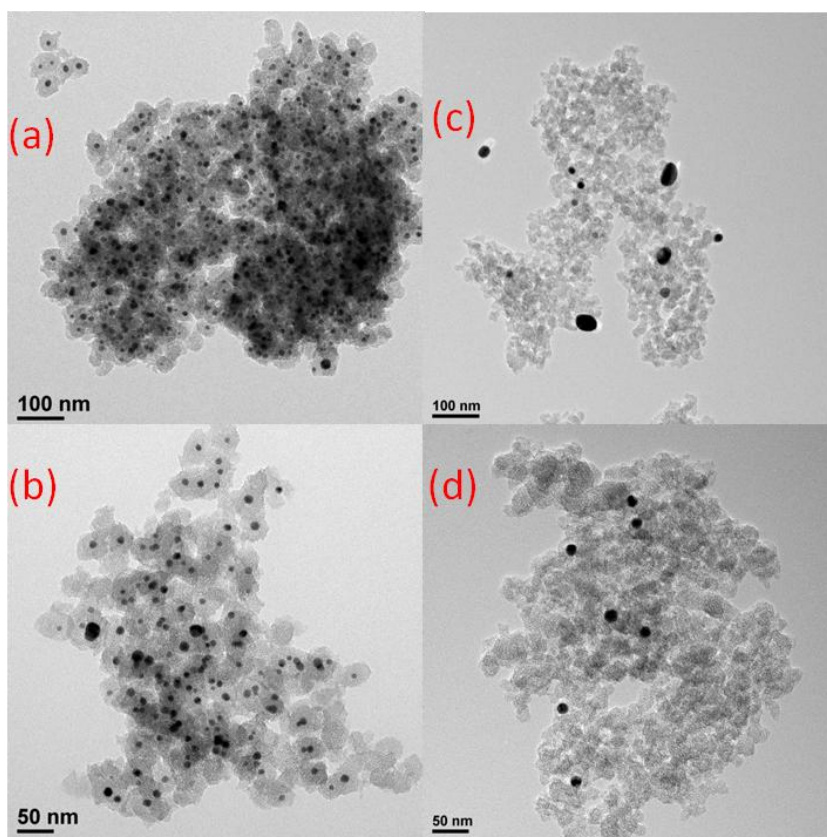


Figure.2c.10 Transmission electron microscopy images of the samples AST5 (a and b) and AST10 (c and d) with various magnifications

Additionally, the 3D morphology of all the samples is identified using scanning electron microscope and is represented in Figure.2c.11.

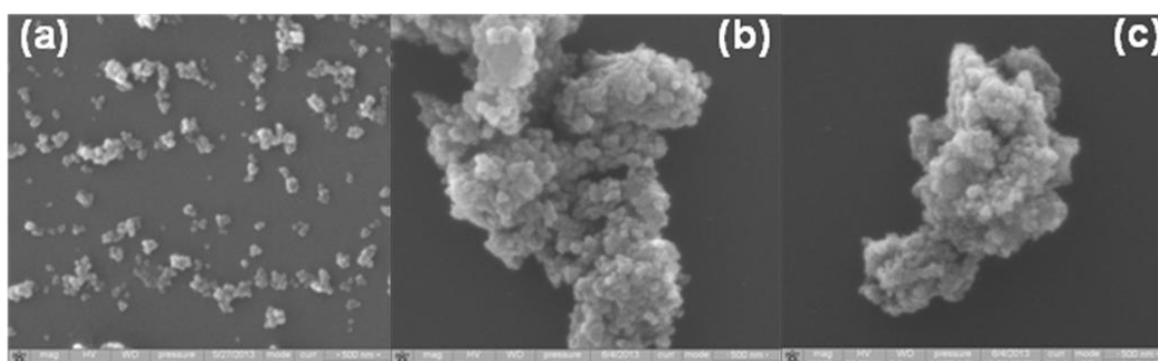


Figure.2c.11 Scanning electron microscopy images of the calcined (a) AST1 (b) AST5 and (c) AST10; scale bar 500 nm

The scanning electron microscopy images shown also confirm the existence of spherical morphology for AST1 and to some extent for AST5, whereas the AST10 system showed more sheet-like structures.

2c.3 Catalytic activity test results

The catalytic applicability as well as the sinter resistance ability of the synthesized material is further tested by considering the bench mark reaction of CO oxidation, which in most reported cases happen at high temperature owing to the non-reducible nature of silica. To our surprise, there was not any literature reference on probing the CO oxidation activity of Au nanoparticles on Ti-SiO₂ supports. One reason could be that Au@Ti-SiO₂ is a potential candidate for epoxidation reactions and most efforts have been directed towards this end.⁶⁰ For epoxidation reaction the mechanistic pathway includes the generation of superoxide species on the Ti-SiO₂ support which enhances the rate of epoxidation reaction.⁶¹ The same type of superoxide species are theoretically supposed to enhance the dissociation of oxygen molecules during CO oxidation reaction in an Au@Ti-SiO₂ support. Both these reasons instigated us to test our Au@Ti-SiO₂ catalyst in CO oxidation reaction rather than much discussed epoxidation reaction. In our synthesis strategy the nanoparticles were prepared with a size ranging from 8-12 nm, which itself places a potential challenge in front of our catalyst for CO oxidation reaction. Literature results clearly emphasize the need of smaller particle size (3-5 nm) for CO oxidation reaction using gold nanoparticles.^{3, 62} Yet, our own previous results shows that CO oxidation can happen in a Au-silica system if the size is above the optimum range as discussed in Chapter.2b.

Catalytic activity for CO oxidation was carried out with and without catalyst pre-treatment step, where the catalyst was reduced in presence of hydrogen gas stream for 1 hr at 400 °C in the pre-treatment step. All the as-synthesized and calcined samples were showing an onset temperature less than 200 °C, which has been dramatically shifted to room temperature in the case of AST1 and AST5 after a mild reduction pre-treatment. The CO oxidation capability of the calcined and the reduced catalysts has been shown in Figure2c.12. When compared with the results discussed in chapter.2b, it can be inferred that the selective doping of optimum amount of Ti on the silica matrix have brought down the 100% conversion temperature into a much smaller value of 160 °C in our AST1 and AST5 systems from 250 °C. The better activity of the AST10 calcined sample (Figure.2c.12a) at higher temperature compared to its counter parts may be due to the presence of smaller titania crystallites in the vicinity of Au nanoparticles, whose signature features were observed in the solid state UV results.

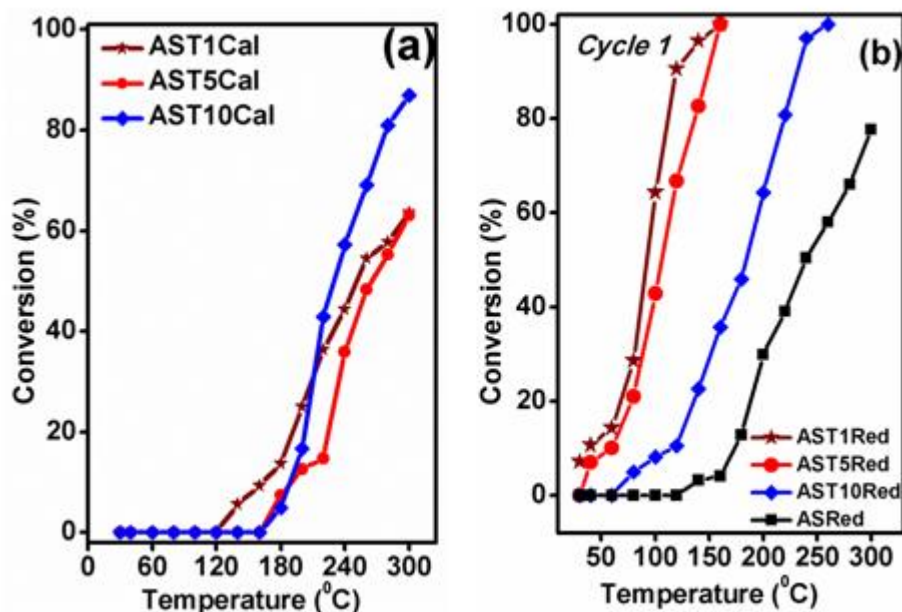


Figure.2c.12 The CO oxidation activity profile (a) calcined and (b) reduced AST series catalysts as a function of temperature. Au@silica (ASRed) reduced sample also represented for clarity in understanding the significance of Ti doping

Additionally, our AST1Cal sample was showing almost similar onset temperature when compared to its reduced Au@silica (denoted as ASRed) counterpart; indicating the potential advantage of titanium doping in higher surface area silica for the development of active Au@Ti-SiO₂ nanocatalysts. It is well documented in literature that the most difficult step in the CO oxidation reaction is the activation of oxygen which is believed to occur at the periphery of the Au-metal oxide interface preferably at the oxygen vacancies.⁶³ In the case of core shell AST1 and AST5 nanocatalysts the incorporation of Ti will generate surface oxygen vacancies along with the gold assisted oxygen vacancy creation in the silica counterpart during the hydrogen pre-treatment. The generation of mobile oxygen vacancies during the hydrogen pre-treatment is previously been reported by Mao et al²⁴ where they discuss the influence of superoxide species formed upon these oxygen vacancies during the reaction, on CO oxidation capability of their catalysts. In Figure.2c.12b, the first cycle of CO oxidation activity after the pretreatment in H₂ for 1 hr at 400 °C is represented. The activity is markedly improved from the calcined catalyst as evident by the lower onset temperature which starts from room temperature in the case of AST1 sample. For comparison the reactivity of Au@SiO₂ is also shown which is recorded at the same conditions as that of AST series. There is a similar activity trend for AST1 and AST5 catalyst when compared to AST10. This is mainly due to the effects of core-shell structure (AST1 and AST5) and particle size (8-10 nm)

in comparison to AST10 (particle size 20 nm). Thus a direct relation between the intact core-shell morphology along with the reducible nature of the Ti doped silica support can be deduced which makes AST1 and AST5 an excellent candidate for CO oxidation reaction. In our case there is generation of ample number of defect sites via oxygen vacancy owing to the existence of easily reducible Ti^{4+} . Along with that, the oxygen vacancies generated during the mild hydrogen treatment in the support results in an overall increase in the defect density in the synthesized catalysts which can bring down the onset temperature as well as an improvement in the maximum efficiency of the catalysts to a much lower temperatures (100% conversion at 160 °C). There is an overall dramatic increase in the activity in the second cycle of the synthesized catalysts below 100 °C even without any catalyst regeneration step and is shown in Figure.2c.13a

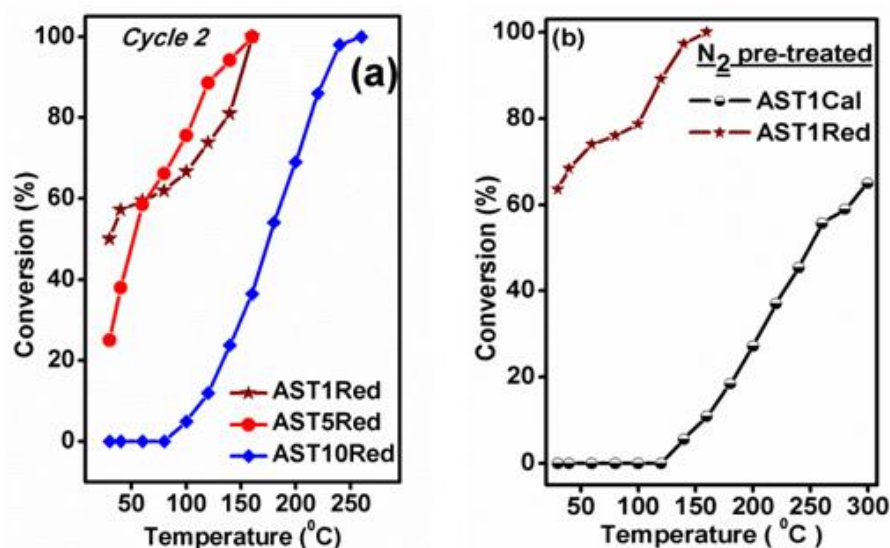


Figure.2c.13 (a) CO oxidation second cycle (b) N₂ pre-treated AST1Red and AST1Cal sample CO oxidation.

The second cycle the increased activity may be attributed to the removal of residual moisture. Such enhancement in the catalytic activity in the second cycle has been observed recently for Au-Y-TiO₂⁶⁴ and Au@SiO₂⁶⁴ catalysts under dry conditions. To understand this further, two experiments were performed where N₂-pretreatment was done on AST1Red and AST1cal sample inside the CO oxidation reactor up to 300 °C. The results of the CO oxidation activity done on these samples are given in Figure.2c.13b. The AST1Red catalyst sample after this N₂ pretreatment gave an activity similar (full conversion temperature) or even better

(increased room temperature activity) than the second cycle activity of AST1Red. On the other hand the AST1Cal sample even after the nitrogen pretreatment did not show much change in its catalytic activity for CO oxidation reaction. Thus the enhanced catalytic activity in the second cycle can be correlated to the removal of residual moisture from our core shell AST nanocatalysts. Further it is evident from the above experiments that a H₂ reduction is necessary to activate the catalysts, preferably by the creation of oxygen vacancies. It will be worth mentioning at this point that the AST1 reduced sample consistently give better catalytic activity for the tested three cycles of CO oxidation without any intermediate catalyst regeneration step (Figure.2c.14)

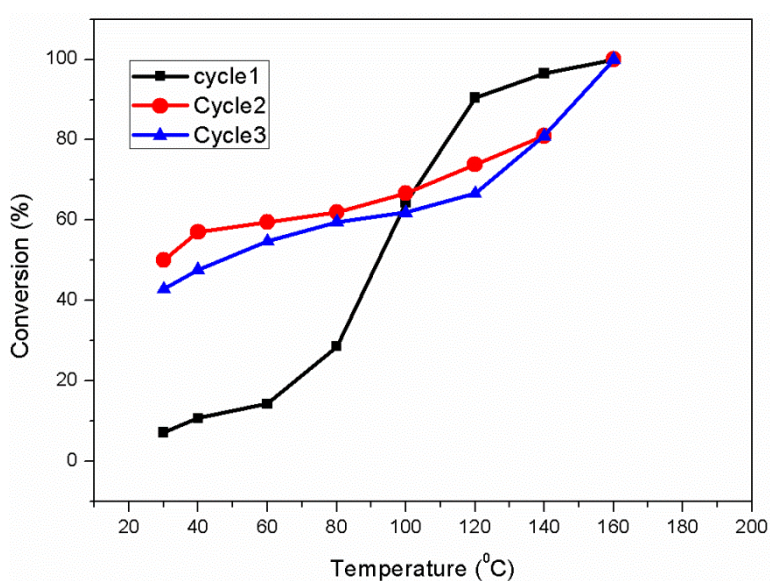


Figure.2c.14 Catalytic activity profile for AST1Red for three consecutive cycles of CO oxidation

2c.4 Spent catalyst analysis

In order to understand the structural and morphological stability of our active AST1 catalysts, XPS, FTIR, and microscopy analysis of the spent catalysts after three consecutive cycles of CO oxidation is carried out. The existence of Ti³⁺ peak in the Ti (2p) XPS spectra (Figure.2c.15a) of the spent catalyst clearly indicates the intact chemical state of the synthesized core shell AST nanocatalysts towards harsh reaction conditions.

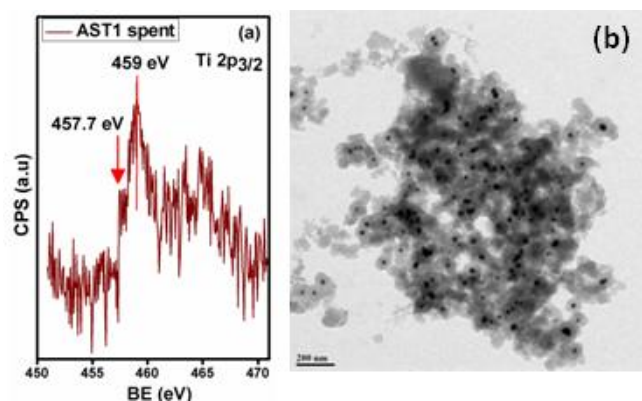


Figure.2c.15 The (a) Ti(2p) XPS and (b) TEM analysis of the spent catalyst after three cycles of CO oxidation

Transmission microscopy analysis of the AST1 catalyst after three cycles of CO oxidation is shown in Figure.2c.15b clearly shows the intact core shell morphology even after three cycles of CO oxidation reaction. Similarly the FTIR analysis (Figure.2c.16) of the spent catalyst did not show much variation from the fresh catalysts, thereby demonstrating the chemical stability of the synthesized Au@Ti-SiO₂ nanocatalysts.

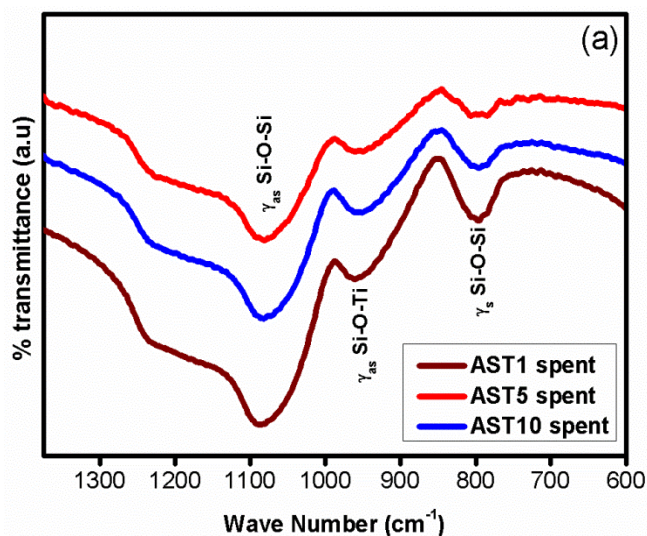


Figure.2c.16 FTIR of the spent AST series catalysts after three cycles of CO oxidation.

2.3 Conclusions

The applicability of the much debated poor silica support for gold based active CO oxidation catalysts is shown in this chapter. In all the Au-Silica synthesis discussed in this chapter, the bifunctionality of the surfactant used is specifically utilised to bring down the complexity associated with the nanoparticle synthesis followed by silica incorporation.

The novel concept of anchoring ultra small gold nanoparticle inside pore channels of porous silica material is successfully achieved and shown in section.2a. The bifunctionality of Pluronic P123 as a reducing agent for gold nanoparticles as well as a structure directing agent for mesoporous silica synthesis is utilised for the anchoring of gold nanoparticle inside the mesopores channels of silica. Here the ultra small gold nanoparticles were able to bring down the onset temperature for CO oxidation into 150 °C after a mild reduction step. The synthesis strategy is further modified to address the basic question of size dependency along with the purposeful avoidance of silica as a support in CO oxidation for gold based catalyst. Hence, in section.2b gold nanoparticles of size 8-12 nm is synthesised and encapsulated in porous spherical silica in a core shell pattern and utilised for CO oxidation. The applicability of CTAB as the capping agent for gold nanoparticles and structure directing agent for porous silica synthesis is applied in this synthesis. It was clearly observed that the material is able to catalyse the CO oxidation both in the calcined and reduced catalyst. In fact the reduced catalyst is having a room temperature activity with 85% conversion at 300 °C. Even without any catalyst regeneration step the core shell catalyst was able to give improved catalytic activity, showing the significance of porous silica support in preventing the widely reported sintering issue owing to the poor metal support interaction in Au-silica systems. Finally, the addition of an oxygen activating species like “Ti” in the silica matrix has further improved the catalytic activity in our core shell Au-Ti-SiO₂ catalyst. The synthesis, characterisation and catalytic activity discussed in section.2c clearly points to the successful incorporation of Ti in the silica matrix creating oxygen vacancies and hence improved oxygen dissociation directly leading to enhanced room temperature activity and 100% conversion. The significance of the overall morphology in catalysis as well as the stability of the catalyst is exemplified by this study since the AST10 catalyst showed poor catalytic activity. On comparison, ultra small gold nanoparticles encapsulated in the channels of mesoporous silica with core shell morphology (Au@SiO₂) with 8-10 nm Au NPs, the core-shell morphology showed much better activity. This has been attributed to the better oxygen activation centres in porous silica spheres. This has been proved by incorporation of Ti, which is expected to produce Ti³⁺ in the Si-O-Ti framework for oxygen activation. Thus it is proved that though Au NPs size is important, O₂ activation is equally important in gold catalysis and if such sites can be provided in an inert support like silica, it can be made room temperature active catalyst beyond the optimum Au NPs size.

2.4. References:

1. G. C. Bond and P. A. Sermon, *Gold Bulletin*, 1973, **6**, 102-105.
2. M. Haruta, *CATTECH*, 2002, **6**, 102-115.
3. M. Valden, X. Lai and D. W. Goodman, *Science*, 1998, **281**, 1647-1650.
4. J. Turkevich, P. C. Stevenson and J. Hillier, *Discussions of the Faraday Society*, 1951, **11**, 55-75.
5. T. K. Sau and C. J. Murphy, *Journal of the American Chemical Society*, 2004, **126**, 8648-8649.
6. X. Zhou, W. Xu, G. Liu, D. Panda and P. Chen, *Journal of the American Chemical Society*, 2010, **132**, 138-146.
7. R. Fenger, E. Fertitta, H. Kirmse, A. F. Thunemann and K. Rademann, *Physical Chemistry Chemical Physics*, 2012, **14**, 9343-9349.
8. S. Hebié, K. B. Kokoh, K. Servat and T. W. Napporn, *Gold Bulletin*, 2013, **46**, 311-318.
9. C.-Y. Chiu, P.-J. Chung, K.-U. Lao, C.-W. Liao and M. H. Huang, *The Journal of Physical Chemistry C*, 2012, **116**, 23757-23763.
10. S. D. Lin, M. Bollinger and M. A. Vannice, *Catalysis Letters*, 1993, **17**, 245-262.
11. W. Yan, B. Chen, S. M. Mahurin, E. W. Hagaman, S. Dai and S. H. Overbury, *The Journal of Physical Chemistry B*, 2004, **108**, 2793-2796.
12. M. Daté, Y. Ichihashi, T. Yamashita, A. Chiorino, F. Boccuzzi and M. Haruta, *Catalysis Today*, 2002, **72**, 89-94.
13. P. M. Arnal, M. Comotti and F. Schüth, *Angewandte Chemie International Edition*, 2006, **45**, 8224-8227.
14. L. M. Liz-Marzán, M. Giersig and P. Mulvaney, *Langmuir*, 1996, **12**, 4329-4335.
15. M. Feyen, C. Weidenthaler, R. Güttel, K. Schlichte, U. Holle, A.-H. Lu and F. Schüth, *Chemistry – A European Journal*, 2011, **17**, 598-605.
16. A. J. Majewski, J. Wood and W. Bujalski, *International Journal of Hydrogen Energy*, 2013, **38**, 14531-14541.
17. S. H. Joo, J. Y. Park, C.-K. Tsung, Y. Yamada, P. Yang and G. A. Somorjai, *Nat Mater*, 2009, **8**, 126-131.
18. D. Zhao, P. Yang, N. Melosh, J. Feng, B. F. Chmelka and G. D. Stucky, *Advanced Materials*, 1998, **10**, 1380-1385.
19. A. K. Prashar, R. P. Hodgkins, J. N. Chandran, P. R. Rajamohanam and R. N. Devi, *Chemistry of Materials*, 2010, **22**, 1633-1639.
20. T. Sakai and P. Alexandridis, *The Journal of Physical Chemistry B*, 2005, **109**, 7766-7777.
21. D. Zhao, J. Feng, Q. Huo, N. Melosh, G. H. Fredrickson, B. F. Chmelka and G. D. Stucky, *Science*, 1998, **279**, 548-552.
22. M. D. Donohue and G. L. Aranovich, *Journal of Colloid and Interface Science*, 1998, **205**, 121-130.
23. Y.-S. Chi, H.-P. Lin and C.-Y. Mou, *Applied Catalysis A: General*, 2005, **284**, 199-206.
24. C.-W. Chiang, A. Wang and C.-Y. Mou, *Catalysis Today*, 2006, **117**, 220-227.
25. H. Zhu, C. Liang, W. Yan, S. H. Overbury and S. Dai, *The Journal of Physical Chemistry B*, 2006, **110**, 10842-10848.
26. B. Yoon, H. Häkkinen, U. Landman, A. S. Wörz, J.-M. Antonietti, S. Abbet, K. Judai and U. Heiz, *Science*, 2005, **307**, 403-407.
27. E. Rombi, M. G. Cutrufello, C. Cannas, M. Casu, D. Gazzoli, M. Occhiuzzi, R. Monaci and I. Ferino, *Physical Chemistry Chemical Physics*, 2009, **11**, 593-602.

28. N. R. G. Jana, L.; Murphy, C. J., *Langmuir* 2001, , **17**, , 6782-6786.
29. K. Qian, W. Huang, J. Fang, S. Lv, B. He, Z. Jiang and S. Wei, *J.Catal*, 2008, **255**, 269-278.
30. K. Qian, H. Sun, W. Huang, J. Fang, S. Lv, B. He, Z. Jiang and S. Wei, *Chem. Eur. J.*, 2008, **14**, 10595-10602.
31. K. Qian, L. Luo, H. Bao, Q. Hua, Z. Jiang and W. Huang, *Catalysis Science & Technology*, 2013.
32. J. Gabaldon, M. Bore and A. Datye, *Top Catal*, 2007, **44**, 253-262.
33. Z. Ma and S. Dai, *Nano Research*, 2011, **4**, 3-32.
34. M. Okumura, S. Nakamura, S. Tsubota, T. Nakamura, M. Azuma and M. Haruta, *Catal. Lett*, 1998, **51**, 53-58.
35. Y. S. Chi, H. P. Lin and C. Y. Mou, *Appl. Catal. A - General*, 2005, **284**, 199-206.
36. E. Rombi, M. G. Cutrufello, C. Cannas, M. Occhiuzzi, B. Onida and I. Ferino, *Phys.Chem.Phys.Chem*, 2012, **14**, 6889-6897.
37. R. Guttel, M. Paul and F. Schuth, *Catalysis Science & Technology*, 2011, **1**, 65-68.
38. S. Eustis and M. A. El-Sayed, *Chemical Society Reviews*, 2006, **35**, 209-217.
39. J. A. Chang, M. Vithal, I. C. Baek and S. I. Seok, *Journal of Solid State Chemistry*, 2009, **182**, 749-756.
40. E. Rombi, M. G. Cutrufello, C. Cannas, M. Casu, D. Gazzoli, M. Occhiuzzi, R. Monacia and I. Ferino, *Physical Chemistry Chemical Physics*, 2009, **11**, 593-602.
41. A. Keshavaraja, V. Ramaswamy, H. S. Soni, A. V. Ramaswamy and P. Ratnasamy, *Journal of Catalysis*, 1995, **157**, 501-511.
42. G. Petrini, A. Cesana, G. Dealberti, F. Genoni, G. Leofanti, M. Padovan, G. Paparatto and P. Roffia, in *Catalyst Deactivation 1991*, 1991, vol. 68, pp. 761-766.
43. T. Blasco, A. Corma, M. T. Navarro and J. P. Pariente, *Journal of Catalysis*, 1995, **156**, 65-74.
44. P. Ratnasamy, D. Srinivas and H. Knozinger, in *Advances in Catalysis, Vol 48*, eds. B. C. Gates and H. Knozinger, 2004, vol. 48, pp. 1-169.
45. G. P. M. Taramasso and B. Notari, *US Patent*, 1983, 4410501.
46. A. J. M. deMan and J. Sauer, *Journal of Physical Chemistry*, 1996, **100**, 5025-5034.
47. G. Deo, A. M. Turek, I. E. Wachs, D. R. C. Huybrechts and P. A. Jacobs, *Zeolites*, 1993, **13**, 365-373.
48. A. Labouriau, T. J. Higley and W. L. Earl, *Journal of Physical Chemistry B*, 1998, **102**, 2897-2904.
49. A. S. Kovalenko, V. G. Il'in and A. P. Filippov, *Theoretical and Experimental Chemistry*, 2000, **36**, 123-145.
50. M. D. Alba, Z. Luan and J. Klinowski, *The Journal of Physical Chemistry*, 1996, **100**, 2178-2182.
51. G. Moretti, A. M. Salvi, M. R. Guascito and F. Langerame, *Surface and Interface Analysis*, 2004, **36**, 1402-1412.
52. A. Y. Stakheev, E. S. Shpiro and J. Apijok, *The Journal of Physical Chemistry*, 1993, **97**, 5668-5672.
53. I. Grohmann, W. Pilz, G. Walther, H. Kosslick and V. A. Tuan, *Surface and Interface Analysis*, 1994, **22**, 403-406.
54. S. B. Waghmode, R. Vetrivel, S. G. Hegde, C. S. Gopinath and S. Sivasanker, *Journal of Physical Chemistry B*, 2003, **107**, 8517-8523.
55. L. Lv, F. Y. Lee, J. Zhou, F. Su and X. S. Zhao, *Microporous and Mesoporous Materials*, 2006, **96**, 270-275.
56. S. Imamura, S. Ishida, H. Tarumoto, Y. Saito and T. Ito, *Journal of the Chemical Society-Faraday Transactions*, 1993, **89**, 757-762.

57. X. T. Gao and I. E. Wachs, *Catalysis Today*, 1999, **51**, 233-254.
58. L. B. Xiong, J. L. Li, B. Yang and Y. Yu, *Journal of Nanomaterials*, 2012.
59. C. Danumah, S. Vaudreuil, L. Bonneviot, M. Bousmina, S. Giasson and S. Kaliaguine, *Microporous and Mesoporous Materials*, 2001, **44**, 241-247.
60. A. K. Sinha, S. Seelan, S. Tsubota and M. Haruta, *Angewandte Chemie International Edition*, 2004, **43**, 1546-1548.
61. V. N. Shetti, P. Manikandan, D. Srinivas and P. Ratnasamy, *Journal of Catalysis*, 2003, **216**, 461-467.
62. M. S. Chen and D. W. Goodman, *Science*, 2004, **306**, 252-255.
63. I. X. Green, W. Tang, M. Neurock and J. T. Yates, *Science*, 2011, **333**, 736-739.
64. F. Romero-Sarria, J. J. Plata, O. H. Laguna, A. M. Marquez, M. A. Centeno, J. F. Sanz and J. A. Odriozola, *RSC Advances*, 2014, **4**, 13145-13152.

Chapter 3

Au-mesoSiO₂ thin film model surface for catalytic applications

published major conclusions from this chapter,

4. A. C. Sunil Sekhar* and C. P. Vinod*, *Molecules*, 2016, 21, 667(invited article for a special issue "Coinage Metal (Copper, Silver, and Gold) Catalysis)

3.1 Introduction

Single crystals surface are used for the better understanding of the catalytic reaction mechanism using surface science tool.¹⁻³ Though these methods open up a great number of scientific conclusions, the major controversy lies in the face that an actual catalyst is far away from these single crystals and this difference is widely understood as the material gap in surface science studies which resides as a major hurdle even now.⁴ In this respect composite thin film surface has emerged as s novel materials, mimicking the chemical properties of the actual catalysts and having almost similar properties of a single crystal surface.⁵⁻⁷ To realise this, efforts have been taken by many groups in developing ordered mesoporous materials coupled with metal nanoparticles.⁷⁻⁸ Model systems like oxide films incorporated with metal nanoparticles are considered to be a promising tool for surface science techniques as they avoid many of the complexities associated with bulk powder materials/catalysts. Ordered mesoporous thin films are ideal choice for the application of catalytic support like their bulk counterpart in catalytic owing to their large surface area, tunable pore size and the presence of ample surface hydroxyl groups.⁹⁻¹⁰ These types of film casting mainly depends on the solvent evaporation rate if wet chemical methods are employed depending on the physical and chemical interactions involved in the sol-gel mixture. Thus the self organisation of the organic-inorganic hybrid under the fast evaporation step is necessary to design crack free porous thin films in different length scale. Templating approach is identified as the successful strategy owing to their variable micellar shape and size under optimum kinetic and thermodynamic conditions allowing the used to fine tune the shape, orientation and size of the pore channels in the final porous thin films. The major challenge in making porous thin film catalytic supports lies in the formation of pore channels oriented perpendicular to the surface of the substrate. Stabilising open pore channel in a perpendicular orientation is based on the surface free energy contributions. It is well know that the low surface free energy contribution from the parallel assembly of the pore channels makes the synthesis of porous thin films with perpendicular pore channels on the substrate difficult. For the catalytic community the essential criterion for a good porous material is that the pore channels have to be accessible to the reactants to favour the reaction kinetics and to avoid any mass transfer limitations. Further, such a perpendicular orientation is necessary if one try to make use of these materials as a support for metal nanoparticle incorporation for nanocatalysis. For thin film casting spin coating and dip coating are the widely used methods though many available methods are there like spry coating. Out of these methods, spin coating is having the

advantage over other methods in its simplicity, ease of use where one can specifically coated on the desired side of the substrate. Once coupled with sol-gel synthesis method, the spin coating method can be visualised as the best tool for developing crack free thin films. These thin films once incorporated with metal nanoparticles could effectively act as catalytic materials, if one could fine tune the nanoparticle size, shape and a better metal support interaction.

Gold nanoparticles are well known for their surface plasmon resonance as well as the catalytic applicability over a wide range of chemical reactions.¹¹ The surface plasmon resonance in the visible region makes the gold nanoparticles a better choice for the surface enhanced Raman scattering (SERS) studies and hence a huge of volume of literature results is available on gold colloid systems.¹²⁻¹⁶ Yet, the lower stability as well as the presence of capping agent on these colloidal systems cause severe concern about the reproducibility of the observed SERS activity. The capability to distinguish between the components in a mixture without their separation gives an upper hand for SERS analysis above other similar spectroscopic techniques though it is associated with the smaller molecular cross section for analysis. Hence, developing a model surface which could sense as well as catalyze an analyte or reaction is of chemical interest. These systems once coupled with operando surface science techniques could pave a way for the mechanistic understanding of many of the catalytically significant reactions.

3.2 Raman Spectroscopy

It is one of the widely used tools to give finger print features of the molecules based on the interaction/scattering of light. The principle behind the Raman analysis is the inelastic scattering of monochromatic light with the molecule under observation. During this interaction the scattered radiation will either loose energy or gain energy and this difference will corresponds to a spectrum when directed towards a suitable detector. The monochromatic light unaffected after scattering is called Rayleigh scattering, the scattered light with increased energy is called anti-stokes lines and the one with lesser energy is called stokes lines. Change in polarizability of a bond is the thumb rule for any species to show Raman Effect under a suitable monochromatic light source. Heterogeneous catalysis is all about surface phenomenon like adsorption and desorption in determining the catalytic activity of the material. Hence, Raman technique can be used to track the catalytic reaction

since the mode of adsorption varies during effective catalysis. The influence of surface enhanced Raman scattering is so profound that single atom detection are possible now.¹⁷⁻²⁰

3.3 Surface Enhanced Raman Scattering (SERS)

The technique utilizes the surface plasmon resonance of the metal NPs to overcome the weak signals in the conventional Raman spectroscopic measurement hindered by the very low efficiency of inelastic photon scattering by molecules.²¹ The colloidal metal nanoparticles are well established SERS materials, but these are often associated with the poor reproducibility of the results. This limitation of SERS substrates hindered the development of Raman scattering as a useful analytical technique for decades. Hence there is a huge scope for the development of easily synthesizable, stable SERS substrates for various applications. There are two widely accepted mechanisms for the SERS signal amplification phenomenon: (a) electromagnetic enhancement and (b) chemical enhancement. The electromagnetic enhancement results in 10^7 - 10^{10} Raman signal enhancement as a result of the amplification of the electromagnetic field of the metal by the surface plasmon resonance; larger nanoparticles as well as rough nanostructures are believed to give enhancement based on this mechanism. In the Chemical enhancement mechanism, the analyte is considered as directly bonded to the metal nanoparticles and thus a change in polarizability of the molecule which leads to the amplification of SERS intensity up to 10^2 - 10^3 . Most of the time electromagnetic enhancement mechanism is kept in mind while synthesizing metal nanoparticles for SERS applications. But for catalysis, generally the smaller nanoparticles or the under co-ordinated atoms in these nanoparticles catalyze the reactions. Hence synthesis of smaller nanoparticles incorporated porous thin film can do catalysis as well as signal enhancement in SERS analysis (based on chemical enhancement mechanism) theoretically, which can sort out the mechanistic aspects of the reaction in one shot.

The inherent surface plasmon resonance of metal nanoparticles offers wide application of them as SERS active substrates in various fields²²⁻²⁵. Among all the metal NPs gold finds its unique place in this field because of its UV-visible absorption, normally falling in the region which is commonly used for Raman spectroscopy. Gold NPs colloids though shows high signal enhancement in SERS but have their inability to give reproducible results in the colloidal state mainly due to the instability of colloidal NPs in solution or due to the masking

of the active surface with the capping agents. Therefore fabrication of such colloidal particles on various substrates becomes mandatory for better results as well as for the repeated use²⁶. Solid SERS active surfaces are an efficient alternative for reproducible and reliable SERS results.

3.4 Gold mesoporous silica thin film model surfaces as nanocatalysts

The concept of thin film model surfaces came up since the single crystalline surfaces are too idealistic to compare with a composite bulk catalyst. To explore the mechanistic understanding of a particular reaction under operando conditions, an elegant approach will be to make composite thin film materials as model surfaces and use it for catalytic insitu and exsitu studies. Gold mesoporous silica offers an ideal candidate for these kinds of applications owing to the wide catalytic application of this system. Further, the surface plasmon resonance of the gold nanoparticles makes it a Raman active substrate which can give Raman scattering signals based on the mode of adsorption of the interacting molecules on the nanoparticle surface. Therefore such materials could potentially catalyze a chemical reaction by simultaneously giving the Raman signals under a Raman spectrometer while shining with a suitable laser source. The ease of accessibility of pore channels is necessary to avoid any mass transfer limitation during catalysis. For that reason researchers are always interested to make porous thin films with pores oriented perpendicular to the surface. The simplicity of sol-gel synthesis method and Spin coating technique makes it a promising route for making homogeneous and flat nanoparticle incorporated thin films. Many of the triblock polymers such as P123, F127 etc; are known as structure directing agents for mesoporous silica synthesis as well as reducing agents for noble metal nanoparticles for decades, yet literature speaks very less about the application of these block copolymers as reducing and structure directing agents within the same system²⁷⁻²⁸. Hence making use of the ability of a structure directing agent as the reducing agent during the synthesis of a composite material can bring down the complexity of the synthesis procedure. Sol-gel method of synthesis followed by spin coating, ageing and calcination is identified as the best protocol for the current study and the major deliverable set for this work are (i) the synthesis of a small gold incorporated mesoporous silica thin films using a simple sol-gel method coupled with spin coating technique (ii) testing the applicability of such a substrate for SERS effects (iii) Using the model thin film surface and the surface enhancement effects to probe the reaction pathway by monitoring the functional group using Raman spectroscopy (iii) correlating the

catalytic activity of the ultra small gold nanoparticles with their enhancement factor in the SERS activity.

A detailed account of the synthesis methodology used along with the characterization and catalytic studies using Raman spectroscopic technique is given in the following sections.

3.5 Synthesis of Au-mesoSiO₂ thin film catalysts (GSM-23F)

The synthesis of the thin film (hereafter GSM-23F) involves three parts,

- (a) pretreatment of substrate
- (b) Synthesis of the silica gold sol-gel and sol ageing
- (c) Spin coating , ageing and high temperature calcinations

3.5.a. Pretreatment of the substrate, Si (100)

The Si (100) wafer 1 x 1 cm² is hydroxylated in boiling water and then calcined at 750 °C for 24 hrs to generate native silica layer on the substrate surface. This calcination will avoid any possible formation of silicides or carbides in the final stage. The native silica layer formed substrate is again hydroxylated to generate a better hydrophilicity for the substrate. The Si (100) wafer disc is purchased from sigma Aldrich and used after the above mentioned pretreatment.

3.5.b. Silica gold sol - gel synthesis

A modified procedure of Stucky et al²⁹ discussed in chapter 2a. is used here for one pot synthesis of Au-silica thin films. Tetra ethyl orthosilicate (Aldrich) is used as the silica source and HAuCl₄.3H₂O (99.99%; Aldrich) as the precursor for gold nanoparticles synthesis. In a typical synthesis 1 ml TEOS is added into a mixture of 8 ml ethanol, 3 ml DI water and 2 ml of HCl (ph=2) and stirred for half an hour at 50 – 80 °C. Then 5ml of 0.1M HAuCl₄ is added and the sol is stirred for another 3 hrs at room temperature. The sol is further kept still at room temperature for another 13 hrs for ageing.

3.5.c. Film casting on the hydroxylated Si (100)

The 13 hr aged gold silica sol is then spin coated on a previously calcined and hydroxylated silicon (100) wafer. Spinning speed is maintained at 1200 rpm for 40s while casting the sol

and then at 3200 rpm again for 40s. The wafers are kept at room temperatures for another two days for film ageing followed by calcinations at 540 °C for 4 hrs in a muffle furnace with a ramping rate of 2°C/minute.

3.6 Results and Discussion

3.6.a. Structural characterisation

Wide angle XRD analysis of the thin film (GSM-23F) gives peaks corresponding to the formation of fcc gold nanoparticles within the mesoporous silica support (Fig.3.1a). Periodicity of the mesoporous silica films were unable to confirm by low angle XRD because of the absence of any low angle peak in the spectrum. Bakshi et al.³⁰ previously reported a detailed study on the reduction mechanism of gold by triblock copolymers such as F127, P123 etc; where they showed the efficient reduction of gold nanoparticles by the PEO surface cavities and the uninterrupted nucleation without any structure transition. Alongside Stucky et al.³¹ elaborated the applicability of P123 for the synthesis of different mesophases of silica films. The applicability of P123 as a reducing agent in our synthesis condition as well as structure directing agent for silica synthesis is detailed in Chapter.2a. The solid state UV-Vis analysis of the film coated on a FTO plate gave a small broad peak at 510 nm indicating the formation of small gold nanoparticles within the system (Figure.3.1b).

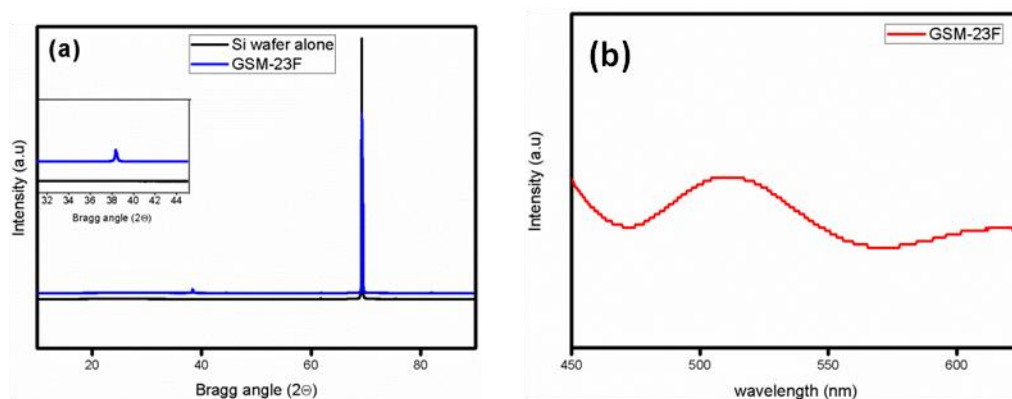


Figure.3.1 the structural characterization of the GSM-23F film (a) wide angle X-ray diffraction analysis of the calcined sample spin coated on a silicon substrate, (b) solid state UV-Vis spectra of the sample spin coated on an FTO plate

The absence of low angle peak in the small angle X-ray diffraction is reported in the past by J. Shi et al.³² in a system similar to GSM-23F though their synthesis strategy which involves surface modification of silica films. Hence, the incorporation of gold nanoparticles within

the mesochannels could be the reason for the lack of any low angle peak in our case. Further, the intended loading of 25wt% is achieved from the ICP-AES analysis.

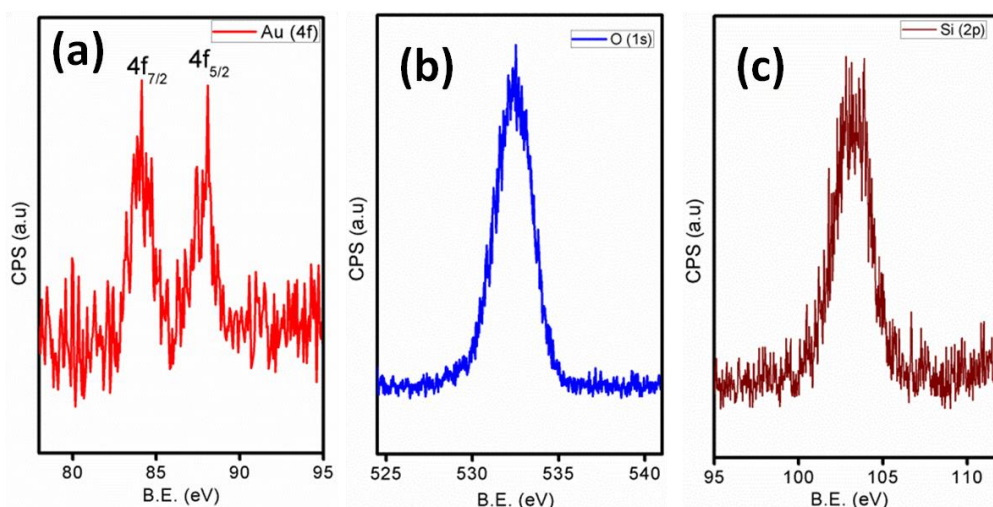


Figure.3.2 XPS data of the GSM-23F thin film after calcination

To explore the chemical composition of the active nanoparticles, XPS analysis of our samples have been carried out and the results are represented in Figure.3.2. The results clearly indicate the existence of gold in the zero valent state with a Au ($4f_{7/2}$) feature at 84 eV. The O1s and Si (2p) binding energy value are also consistent with the silica values.

3.6.b Microscopy analysis

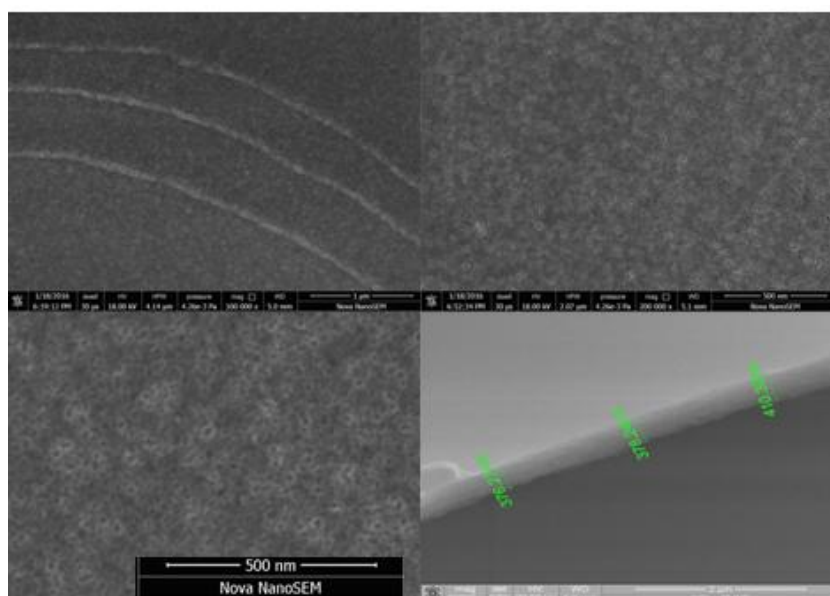


Figure.3.3 Scanning electron microscopy images of the thin film GSM-23F on various magnifications and the cross sectional analysis of such a thin film

In order to understand the three dimensional morphology of the thin films formed on Si (100) substrate FESEM analysis is carried out. Formation of crack free films in macroscopic level is clearly observable in the low resolution FESEM image. In addition to that accessible pore channels oriented perpendicular to the substrate is evident from the FESEM images at higher resolutions (Figure.3.3).

The elemental mapping analysis done on thin film samples further exemplifies the distribution of small gold nanoparticles in a uniform manner on the pore channels (Figure.3.4). The easily accessible pore channels for reactants to reach active gold nanoparticles make it a live template for catalytic reactions. Moreover the well separated ultra small gold nanoparticles can generate hot spots under suitable conditions to become an important analytical tool for SERS analysis.

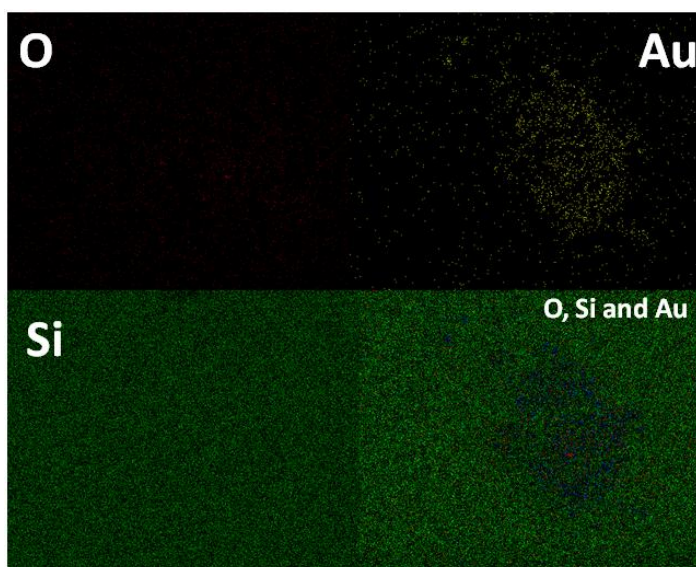


Figure.3.4 Elemental mapping of the GSM-23F thin film done under scanning electron microscope

The high resolution TEM images Figure.3.5 (a and b) clearly show the presence of mesoporosity, yet it is really difficult to distinguish between gold nanoparticles and the empty pores which left us to believe that small Au particles are trapped inside the channels. The rough estimate of pore size from TEM image is 3.5 nm. The high resolution TEM images exemplify the success of the synthesis procedure as most of the pores are filled with gold nanoparticles.

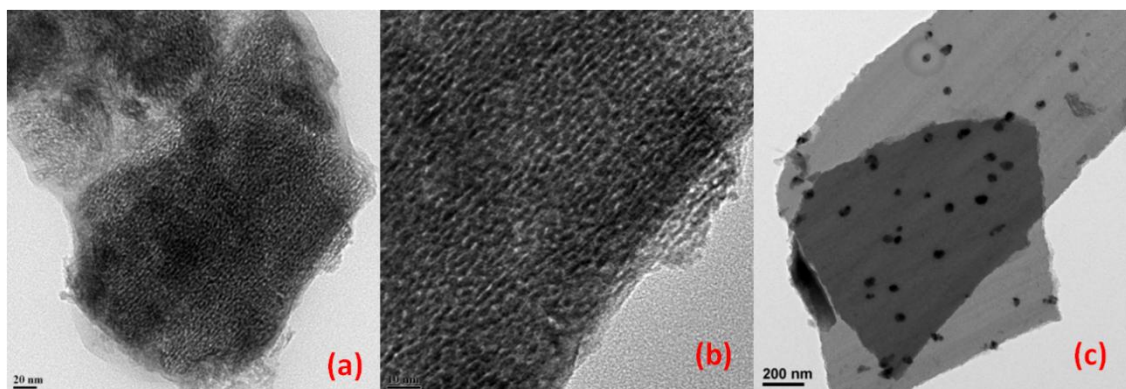


Figure.3.5 High resolution TEM images of GSM-23F under various magnifications (a) 20 nm, (b) 10 nm and (c) 200 nm

SAED analysis while doing TEM also failed to give any signature for the lattice parameters for gold; this discrepancy between XRD and TEM could mainly be because of the signal averaging used in XRD analysis. We do observe some bigger gold nanoparticles on the amorphous silica regions in the TEM analysis (figure.3.5c) which are possibly formed due to agglomeration of the particles which are not trapped inside the channels. Interestingly these regions containing gold nanoparticles with size ranging from 20-60 nm showed no observable porosity on silica matrix. Robertson et al.³³ previously reported that the silica thin films spin cast on gold coated glass slides gave insulating films without any observable pores. Their synthesis did not involve any porogen whereas in our case P123 is used as the structure directing agent for mesoporous silica synthesis. Therefore P123 along with the ultra small gold nanoparticles are the reasons for maintaining observable mesoporosity in our case.

The properties of an ideal catalytic system in our GSM-23F thin film are evident in all the above mentioned characterizations. The high porosity observed in the TEM and SEM (Fig.3.5 and Fig.3.3) directly points to the ease of access of the reactants/products during the catalytic reaction. Similarly, signal amplification can be expected while analysing the SERS of the probe molecules RhodamineB based on chemical enhancement mechanism. Making use of a catalytic system for the SERS analysis could potentially result in the development of multi tasking materials which could sense the analyte in a mixture and can easily catalyse the reaction towards the direction of the desired product. A detailed understanding of the SERS and catalytic application of our GSM-23F thin film is discussed in the following section,

3.7 Experimental: SERS and catalytic reaction

The SERS studies are done using 10^{-8} M aqueous solution of Rhodamine B. Typically, 1×1 cm² silicon wafer coated with GSM-23F thin film is completely dipped in 2 ml of the 10^{-8} M Rhodamine B for 1 hour. The film is then washed with distilled water to remove excess dye from the surface and dried at 60 deg for 1 hour prior to Raman analysis using 633 nm laser sources. The same protocol is followed for the bare silicon wafer as well as the Silica thin film coated Si wafer for comparison.

For the catalytic reduction of 4-nitrophenol (PNP) to 4-aminophenol (PAP), a 1×1 cm² silicon wafer coated with GSM-23F is dipped in a small glass open reactor and sodium borohydride is added in order to start the reaction. Periodically Raman data is collected and analyzed for understanding the reaction progress. Typically, 20 microliter 0.1 M PNP is added to a thin film placed in the glass reactor followed by the addition of 2.5 ml 1 M NaBH₄ and the progress of the reaction is monitored using a raman instrument equipped with CCD detector and 514/633 nm laser source. Normal Raman spectra of the standard compounds are analyzed using a 633 nm laser source.

3.8 GSM-23F as a robust SERS substrate

The incorporation of ultra small gold nanoparticles within the mesopores of the silica matrix can develop hot spots, which on the application of suitable resonance frequency will act as SERS probes. The large Raman cross section along with ample number of references in the literature³⁴⁻³⁶ made us to select Rhodamine B as the probe molecule for the enhancement study with our GSM-23F. Therefore any change in the Raman spectrum could be attributed to the interaction of the SERS substrate with the adsorbed probe molecule. As expected our system is able to give an enhancement of 10^3 with Rhodamine B (10^{-8} M). In the case of gold there are reports saying that as particle size increases the enhancement factor also increases.³⁵ A large ordered super lattice structures in these bigger particles develop strong inter particle plasmon coupling thereby higher SERS enhancement. The ultra small nanoparticles in GSM-23F produces chemical enhancement in the present study which leads to significant enhancement in signal intensity for Rhodamine B even at a concentration as low as 10^{-8} M. One could barely see any signature of Rhodamine B when a silica film without gold nanoparticles is used as the substrate (Figure.4.6).

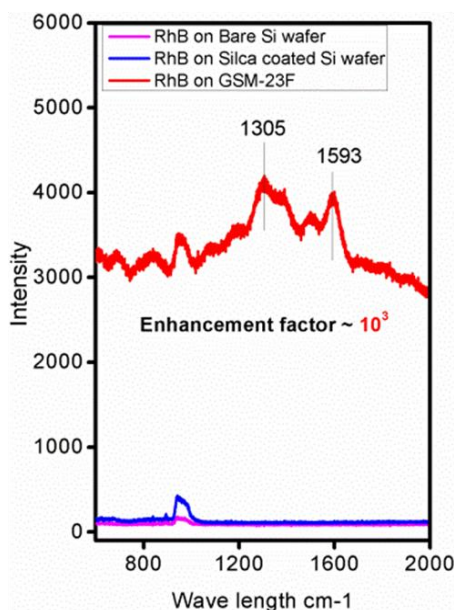


Figure.3.6 SERS spectra of Rhodamine B on GSM-23F thin film and the bare silicon substrate

Figure.3.6 clearly express the enhanced intensity, and the enhancement in intensity is calculate by comparing the peak intensity at 1305 cm⁻¹ in the silica alone system and GSM-23F. As the gold nanoparticles are well separated by the mesopore walls of silica the electromagnetic enhancement towards SERS activity cannot be expected. More over the lesser affinity of silica towards gold nanoparticle avoids any charge transfer interaction towards signal enhancement.³⁷ Thus, approximately three orders of magnitude of enhancement observed in our case is mainly due to chemical enhancement theory which explains the relatively smaller enhancement observed here. It is worth mentioning at this point that these materials are primarily developed for catalytic applications and there nanoparticles separation from one another is rule of thumb for better activity.

3.9 GSM-23F as a catalytically active model surface

The catalytic applicability of the synthesised model surface in catalysis is tested by doing the reduction of the nitro group to amino group by sodium borohydride under a Raman microscope using monochromatic light source. Conversion of aromatic nitro compounds to amino compounds is an important class of reaction in pharmaceutical industries. It is well known that gold can catalyse the reduction of p-nitrophenol to p-aminophenol using sodium

borohydride and is tracked using UV-Vis spectroscopy owing to the inherent visible light absorption property of the molecules. To begin such a catalytic study probed by Raman spectroscopic technique, the Raman cross section of the molecule is a major factor; hence the Raman spectra of all the standard molecules have been checked initially using a 633 nm source (Figure.3.7).

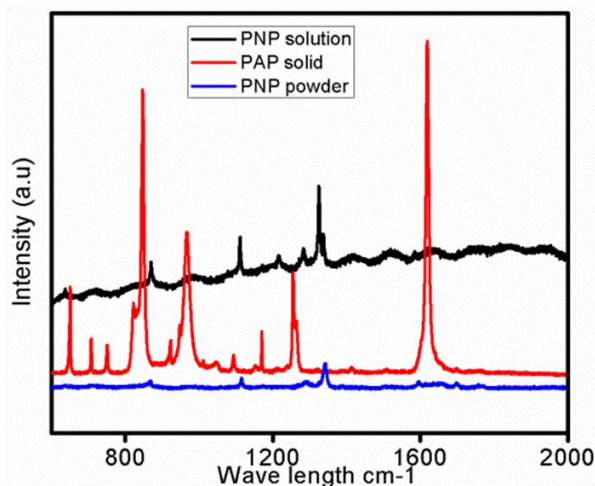


Figure.3.7 Raman spectra of the organic molecules under consideration using 633 nm laser source, namely p-nitrophenol (PNP) and p-aminophenol (PAP) in solid and aqueous phase

It is evident from figure.3.7 that p-nitrophenol and p-aminophenol both are giving distinct spectra in the solid and aqueous phase, yet the Raman scattering cross section was very limited in the case of p-aminophenol in the aqueous phase.

Recently Sun et al.³⁸ reported the conversion of p-nitrophenol to p-aminophenol using silver microflower and used Raman spectroscopy for insitu monitoring of the reaction pathways. Here, the features corresponding to the p-nitrophenol in their Raman spectra were not observed. Contradictory to that our experiments gave intense peaks in the spectra of p-nitrophenol and could clearly show the decrease in intensity as time progresses and the complete absence of the peak corresponding to $-\text{NO}_2$ group after the completion of reaction. The lower scattering cross section of the amino group or the weaker interaction between the gold NPs and p-aminophenol could be the reason for the absence of the peak corresponding to amino group in our Raman spectra. Since the synthesis strategy used for the composite thin film resembles that of Au@silica discussed in chapter.2a, the presence of catalytically active ultra small gold nanoparticles in the present system is also anticipated and hence 514 nm laser source is used for the catalytic studies first. The literature claims the existence of

different vibrational bands in the Raman spectra of PNP as 869 (C-H out of plane bending), 1120 (C-H in plane bending mode) and 1341 cm^{-1} ($-\text{NO}_2$ as-symmetric stretching mode)³⁹. In our case the prominent peak positions were 1341 cm^{-1} (for Solid 4-nitrophenol), 1324 cm^{-1} (for 4-nitrophenol solution in water) and 1256 and 1621 cm^{-1} (for solid 4-aminophenol) under a 633 nm laser source in normal Raman spectra (Figure.3.7). Whereas the prominent peak of the nitro group on the thin film catalysts under the reaction condition is slightly shifted to 1292 cm^{-1} under the 514 nm laser source and the addition of the reducing agent sodium borohydride bring about the reduction reaction as observed in the intensity of the corresponding nitro group over a period of 100 minutes and it vanishes completely in 120 minutes (Figure.3.8). A similar observation is reflected when the laser source is changed from 514 nm to 633 nm, indicating the versatility of the synthesised thin film catalyst for catalysis as well as Raman studies.

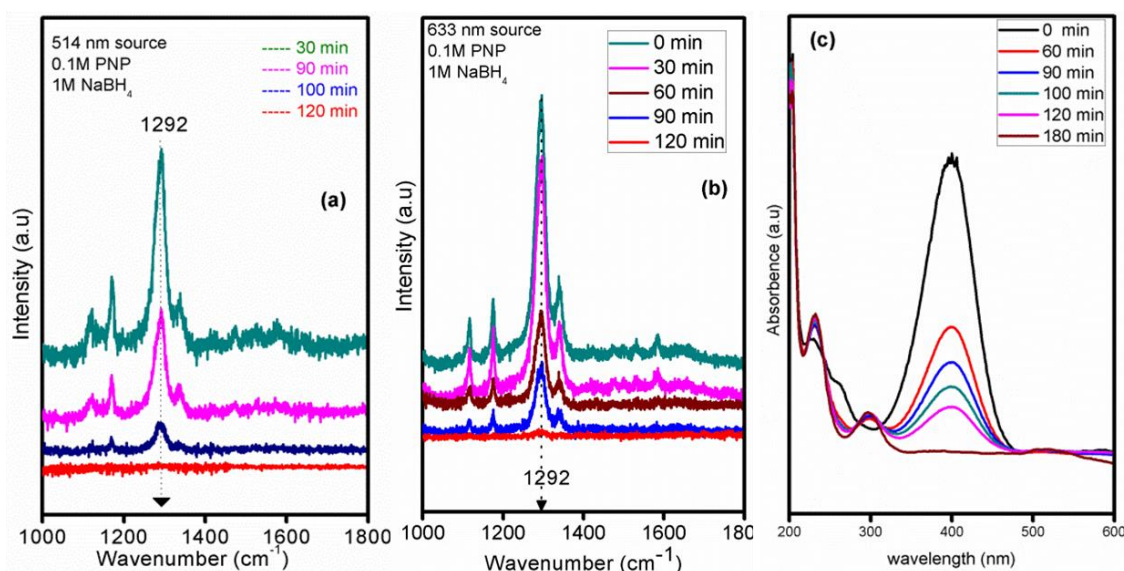


Figure.3.8 p-nitrophenol (PNP) to p-aminophenol (PAP) conversion on the GSM-23F thin film catalyst using sodium borohydride as the reducing agent monitored using a Raman spectrometer with a laser source of wavelength (a) 514 nm and (b) 633 nm. The same reaction is probed using (c) UV-Vis spectrophotometer under identical condition to Raman analysis to show the formation of PAP (peak at 300 nm in figure c)

The absence of any signature peak corresponding to $-\text{NH}_2$ group in the Raman spectra after the reaction (though the $-\text{NO}_2$ peak is completely vanished), PAP formation is further confirmed by UV-Vis spectra (Figure.3.8c). This experimental condition of UV-Vis and Raman analysis were same; hence there will not be any ambiguity in comparing the results. Emergence of a peak at 300 nm with time and the decrease in the peak intensity at 400 nm

clearly validate the reduction of PNP with sodium borohydride in presence of GSM-23F. To validate our assumption of lower cross section of PAP as a reason not to show any signature features in our experimental conditions under the Raman spectrometer, an SERS experiment with a similar concentration of PAP solution is intended to do our a gold colloid solution (CTAB capped gold nanoparticles of size 8-12 nm). In a colloidal system the widely explained SERS mechanism is based on electromagnetic enhancement and in such systems the literature claims an enhancement of the order of 10^4 - 10^7 . The SERS signal from the PAP solution obtained is shown in figure.3.9 and is clearly evident that the enhancement is lesser based on the electromagnetic enhancement mechanism. This gives us the positive impact that, our assumption regarding the lower cross section can be reason for the absence of any signal corresponding to the NH_2 group in the Raman spectra.

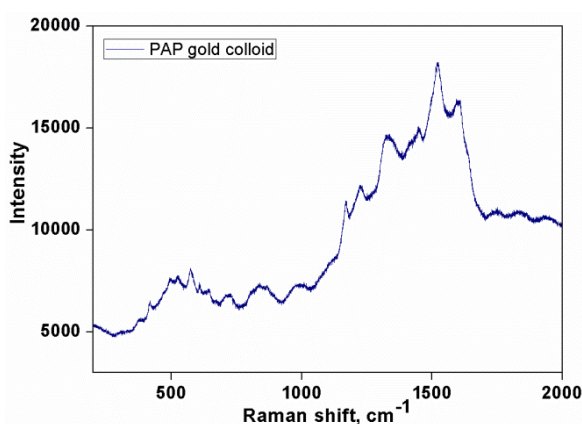


Figure.3.9 Raman spectral data of 4-aminophenol with Au nanoparticle colloid (CTAB capped 8-12 nm Au NPs) under 633 nm laser source

Thus the synthesised materials showed promising catalytic activity for the p-nitrophenol reduction to p-aminophenol which is tracked using Raman spectroscopy as well as UV-Vis spectrophotometer. These initial results could pave the road towards the applicability of composite thin films in understanding the reaction mechanisms in heterogeneous catalysis. For the present reaction, more studies are needed to improve the sensitivity of the GSM-23F for amplifying the signal intensity while doing catalysis, so that the product p-aminophenol generation can also be tracked irrespective of its smaller Raman cross section. The smaller SERS enhancement factor compared to other colloidal or fabricated NPs systems is most likely due to the chemical enhancement mechanism. Since the synthesised NPs are ultra small as well as they are separated by porous silica walls, the electromagnetic enhancement

mechanism is ruled out in our GSM-23F. The equally spaced gold NPs while shining with the laser can generate some plasmonic hot spots in close proximity and thus amplify the SERS signal intensity.

3.10 Conclusions

An easy and convenient way for making gold incorporated porous silica thin films is successfully designed by utilising a sol-gel methodology followed by spin coating. The characterization revealed that the films are crack free with perpendicular pore channels. These gold incorporated silica thin films are demonstrated to show SERS property. Further, p-nitrophenol reduction reaction was used and monitored using Raman spectroscopy as a test reaction and proved the usefulness of the thin film as catalytically active substrate for model surface science studies. This approach can be used for making other catalytically relevant metal nanoparticle-silica systems for fundamental as well as insitu surface science studies.

3.11 Reference

1. D. W. Goodman, *Chemical Reviews*, 1995, **95**, 523-536.
2. G. Rupprechter, in *Surface and Interface Science*, Wiley-VCH Verlag GmbH & Co. KGaA, 2016, pp. 459-528.
3. B. E. Bent, *Chemical Reviews*, 1996, **96**, 1361-1390.
4. G. Prieto and F. Schüth, *Journal of Catalysis*, 2015, **328**, 59-71.
5. C. R. Henry, *Surface Science Reports*, 1998, **31**, 231-325.
6. G. A. Somorjai, R. L. York, D. Butcher and J. Y. Park, *Physical Chemistry Chemical Physics*, 2007, **9**, 3500-3513.
7. M. Bowker, P. Stone, P. Morrall, R. Smith, R. Bennett, N. Perkins, R. Kvon, C. Pang, E. Fourre and M. Hall, *Journal of Catalysis*, 2005, **234**, 172-181.
8. M. Sterrer and H.-J. Freund, *Catalysis Letters*, 2013, **143**, 375-385.
9. P. Innocenzi and L. Malfatti, *Chemical Society Reviews*, 2013, **42**, 4198-4216.
10. P. Innocenzi, L. Malfatti and G. J. A. A. Soler-Illia, *Chemistry of Materials*, 2011, **23**, 2501-2509.
11. M. Pan, A. J. Brush, Z. D. Pozun, H. C. Ham, W.-Y. Yu, G. Henkelman, G. S. Hwang and C. B. Mullins, *Chemical Society Reviews*, 2013, **42**, 5002-5013.
12. R. Que, M. Shao, S. Zhuo, C. Wen, S. Wang and S.-T. Lee, *Advanced Functional Materials*, 2011, **21**, 3337-3343.
13. W. Lee, S. Y. Lee, R. M. Briber and O. Rabin, *Advanced Functional Materials*, 2011, **21**, 3424-3429.
14. M. Pradhan, J. Chowdhury, S. Sarkar, A. K. Sinha and T. Pal, *The Journal of Physical Chemistry C*, 2012, **116**, 24301-24313.
15. C. Muehlethaler, M. Leona and J. R. Lombardi, *Analytical Chemistry*, 2016, **88**, 152-169.
16. F. Laura, *Journal of Optics*, 2015, **17**, 114002.
17. E. C. L. Ru and P. G. Etchegoin, *Annual Review of Physical Chemistry*, 2012, **63**, 65-87.
18. P. Garg and S. Dhara, *AIP Conference Proceedings*, 2013, **1512**, 206-207.
19. Y. Wang and J. Irudayaraj, *Philosophical Transactions of the Royal Society B: Biological Sciences*, 2013, **368**, 20120026.
20. K. Kneipp, Y. Wang, H. Kneipp, L. T. Perelman, I. Itzkan, R. R. Dasari and M. S. Feld, *Physical Review Letters*, 1997, **78**, 1667-1670.
21. E. C. Le Ru and P. G. Etchegoin, in *Principles of Surface-Enhanced Raman Spectroscopy*, Elsevier, Amsterdam, 2009, pp. 1-27.
22. C. J. Orendorff, A. Gole, T. K. Sau and C. J. Murphy, *Analytical Chemistry*, 2005, **77**, 3261-3266.
23. S. Nie and S. R. Emory, *Science*, 1997, **275**, 1102-1106.
24. M. A. El-Sayed, *Accounts of Chemical Research*, 2001, **34**, 257-264.
25. F. Castillo, E. De la Rosa and E. Perez, *European Physical Journal D*, 2011, **63**, 301-306.
26. M. Roca and A. J. Haes, *J. Am. Chem. Soc.*, 2008, **130**, 14273-14279.
27. B. Gawel, K. Lambrechts, K. Gawel and G. Oye, *Microporous and Mesoporous Materials*, 2012, **164**, 32-37.
28. E. Pedrueza, J. L. Valdes, V. Chirvony, R. Abargues, J. Hernandez-Saz, M. Herrera, S. I. Molina and J. P. Martinez-Pastor, *Advanced Functional Materials*, 2011, **21**, 3502-3507.

29. D. Zhao, P. Yang, N. Melosh, J. Feng, B. F. Chmelka and G. D. Stucky, *Advanced Materials*, 1998, **10**, 1380-1385.
30. P. Khullar, V. Singh, A. Mahal, H. Kaur, T. S. Banipal, G. Kaur and M. S. Bakshi, *Journal of Physical Chemistry C*, 2011, **115**, 10442-10454.
31. P. C. A. Alberius, K. L. Frindell, R. C. Hayward, E. J. Kramer, G. D. Stucky and B. F. Chmelka, *Chemistry of Materials*, 2002, **14**, 3284-3294.
32. F. M. Cui, Z. L. Hua, X. Z. Cui, L. M. Guo, C. Y. Wei, W. B. Bu and J. L. Shi, *Dalton Transaction*, 2009, 2679-2682.
33. J. W. Robertson, M. Cai and J. E. Pemberton, *Advanced Materials*, 2001, **13**, 662-667.
34. J. H. Shen, Y. H. Zhu, X. L. Yang, J. Zong and C. Z. Li, *Langmuir*, 2013, **29**, 690-695.
35. C. Shen, C. Hui, T. Yang, C. Xiao, J. Tian, L. Bao, S. Chen, H. Ding and H. Gao, *Chemistry of Materials*, 2008, **20**, 6939-6944.
36. J. P. Xie, Q. B. Zhang, J. Y. Lee and D. I. C. Wang, *Acs Nano*, 2008, **2**, 2473-2480.
37. A. P. Budnyk, A. Damin, G. Agostini and A. Zecchina, *The Journal of Physical Chemistry C*, 2010, **114**, 3857-3862.
38. B.-B. Xu, R. Zhang, X.-Q. Liu, H. Wang, Y.-L. Zhang, H.-B. Jiang, L. Wang, Z.-C. Ma, J.-F. Ku, F.-S. Xiao and H.-B. Sun, *Chemical Communications*, 2012, **48**, 1680-1682.
39. M. K. Khaing Oo, Y. Guo, K. Reddy, J. Liu and X. Fan, *Analytical Chemistry*, 2012, **84**, 3376-3381.

Chapter 4

Engineering the porous architecture of Pt-alumina and its environmental catalysis

4.1 Introduction

The interest in designing functional porous oxide materials originates from their immense applications in the field of adsorption/separation,¹⁻³ catalysis,⁴⁻⁶ drug delivery,⁷⁻¹¹ optics,¹²⁻¹⁵ electrochemistry and energy related areas.¹⁶⁻¹⁹ In this regard, much research is dedicated towards developing ordered porous materials in different length scales. Of which mesoporous materials are widely used as catalysts as well as catalytic supports in many catalytic applications. The inexpensive nature along with the high thermal stability and moderate lewis acidity makes alumina as one of the finest choice of non-siliceous porous materials in the industrial perspectives, as evident from the potential application in the petrochemical industry as well as the automobile emission control systems.²⁰⁻²³ Herein, the study will be devoted to the design of Pt/Alumina architectures and its application to an important environmental reaction in aqueous phase: nitrite removal

Water pollution, as a consequence of the agricultural and industrial development of our society, hazards one of our most precious and scarce resources. In this line, the removal of nitrates and nitrites from drinking and waste waters will be required in the near future to meet the demands in water of an expanding 21st century world population. Stringent environmental protection guidelines²⁴ have resulted in the development of various biological and physico-chemical treatment technologies (e.g., biological processes, reverse osmosis, nanofiltration, ion exchange, electrodialysis, chemical and catalytic hydrogenation)²⁵⁻²⁶ for the denitrification of surface as well as ground water. The latter catalytic process has recently emerged as a promising technology for the elimination of these compounds as it possesses advantages like easier operational control, higher conversion rate and the absence of any secondary pollutant.²⁷ This technology is based on a two-step process involving the successive hydrogenation of nitrate into nitrite and nitrite into nitrogen.²⁸ Nitrate was found to be hydrogenated only by bimetallic catalysts, whereas nitrite can be reduced on monometallic catalysts.²⁹ With hydrogen as reducing agent, nitrite can be converted to nitrogen as a main product and ammonium ions as undesired by-product. In this line, one important barrier to practical application of heterogeneous catalysts is the selectivity control which remains crucial in the optimisation of the materials properties. Hence, catalysts with greater selectivity for N₂ over ammonium ions are highly desirable for the denitrification reaction where internal diffusion phenomena easily occur. Generally, a common experimental approach for optimizing catalytic systems consists in studying the influence of the active phase properties (support composition effect, dispersion, size, morphology)³⁰⁻³¹ and/or

reactor design³²⁻³³ on catalytic performances, whereas theoretical methods help in optimizing the porous structure toward mass transport properties of species.³⁴ Strukul et al. first shed light on the importance of mass transport phenomena in the catalytic removal of nitrites.³⁵ By lowering the mesopore size of Pd/SnO₂ catalytic materials, they were able to observe an increase of ammonia production which may be caused by the slower diffusion of OH⁻ ions from narrow mesopores of the catalyst to the solution. Later on, Lefferts et al. showed that the use of thin layer of carbon-nano-fibres led to improved mass transfer properties thanks to the high textural porosity as well as low tortuosity of the catalytic material.³⁶ Albeit demonstrating the importance of active site accessibility, the above mentioned catalytic systems exhibit weakly defined porosity (inter particle voids) and limited pore connectivity which affect mass transfer and pore blocking to some extent. Taking advantage of the recent development of mesostructuration³⁷ and macrostructuration³⁸ routes giving well-defined structural pore systems, hierarchically structured macroporous mesoporous materials are now preferably investigated in heterogeneous catalysis.³⁹ Many examples highlight the superior mass transport properties of hierarchical catalysts with respect to mesoporous counterparts,⁴⁰⁻⁴¹ but to our knowledge, much less research is conducted on how the reaction selectivity can be controlled through the careful modification of macropore properties, particularly for alumina systems.

Efforts have been devoted from many of the research groups in tailoring the properties of the porous alumina utilising different methodologies. A cross sectional analysis through the literature results will show us the widely used methods as sol-gel,⁴²⁻⁴⁴ hydrothermal,⁴⁵⁻⁴⁶ liquid crystal templating methods, evaporation induced self assembly methods⁴⁷ etc. General focus has been given on improving active phase access (i.e. nano-Pt particles) through the fine tuning of the porosity ; since textural properties is one of the fundamental factor contributing towards many of the basic properties of alumina, like catalytic performance and adsorption properties. The limited range of mesoporosity/microporosity (<5 nm) of the alumina systems has limited its applications to some extent; but surfactant templating has taken up the opportunity to increase the surface area as well as tunable pore size when compared with bulk alumina. Larger pore size is always welcomed by catalytic as well as industrial communities as it enhances the diffusion properties of the material. Replicating the ordered arrangements of the templates has been chosen as one of the best methods for the synthesis of mesoporous materials in the past. Soft templating, hard templating and a combination of soft and hard templating is successful in generating a wide array of pore size distribution and greater surface area. The flexibility of

the soft templating approach always gives an up hand for such methodology when compared with hard templating approach. In the soft templating approach one can easily tune the size and shape of the micelle assembly by varying the concentration as well as the nature of the solvent/temperature conditions. Here, the inorganic precursor will grow around such micellar assembly having specific orientations like hexagonal, lamellar, cubic etc under ideal conditions and finally develops identical pore systems in the material once the surfactant/template is removed from the growing matrix. Whereas, in the hard templating approach the inorganic precursor will grow within the voids of the network such as silica spheres, Spherical polymer beads, hexagonal SBA-15 like systems and replicates a similar organised pore networks once the hard templates is removed. A combination of the hard-soft templating approach is envisaged as a better protocol since it gives the flexibility of the soft templating approach as well as intact ordering of a hard templating approach to different pore length scale. The proper tuning of the synthesis conditions will thus generate materials with a co-operative assembly of interconnected pore networks within the same bulk system; a much invited possession of a catalytic material, ordered dual porosity. Yet, there are scares literature results showing the direct influence of these kinds of dual pore systems in the conversion as well as selectivity of any catalytic reactions. In catalysis one of the major challenges is the heat and mass transfer limitations of the catalysts during the actual catalysis. The interconnected micro, meso and macro pore systems are considered as the best choice since it can avoid the above said limitations to a considerable extent within the catalytic regime without compromising much of the materials catalytic property.

Though surfactant templating can be adapted in any of the conventional porous material synthesis like sol-gel, hydrothermal, co-precipitation, evaporation induced self assembly (EISA) etc; the self assembly approach is considered superior if one uses alkoxides as inorganic precursors during synthesis, since its hydrolysis/condensation and growth can easily be tuned. Self assembly is the process by which the spontaneous organisation of the material occurs through non-covalent interactions without any external interventions. Literature results show the efforts taken by the catalytic fraternity in utilising the various methodologies for porous alumina synthesis in the past. Stein et al⁴⁸ first materialized macroporous alumina with periodically interconnected pore networks using latex beads. Similarly, Cai et al⁴⁹ has reported in the past the synthesis of mesoporous alumina by a soft templating approach with variable pore size as well as metal-support interactions. Yuan and co-workers⁵⁰ has reported a combined approach by using non-ionic copolymer and

polyurethane foam in the development of macroporous-mesoporous alumina monoliths with crystalline nature. A dual templating approach using pluronic as well as latex beads has been previously reported by Dacquin et al⁵¹, where they were able to show hexagonally ordered mesopores within macroporous walls throughout the alumina framework. These materials once anchored with active catalytic components can be effective in fine tuning the product selectivity based on the textural property of the support. Specifically, in case of metal nanoparticles, the conventional wet impregnation methodology is considered as the best when very small metal loading is intended, though there are a number of methods like colloidal impregnation, deposition-precipitation, co-precipitation method etc. available. A correlation of the catalytic activity and selectivity with pore properties on alumina has previously been reported by Čejka et al⁵², indicating the significant role of controlling the synthesis parameters in order to tailor the structural as well as textural properties.

Evaporation induced self assembly approach is widely accepted as one of the best method in the tailored synthesis of meso-ordered materials, though it is time consuming. Playing around with the surfactant assembly is the major challenge involved in this type of synthesis. Generally large organic molecules are introduced into the solution phase along with the surfactant in order to generate large mesopores in silica based materials and reported in the past.⁵³⁻⁵⁴ Making use of the hydrophobic interaction of the organic swelling agent 1,3,5-trimethylbenzene with the surfactant template, Zhao et al⁵⁵ recently made hierarchically ordered mesoporous alumina with 2D hexagonal pore structure. Recently Li et al⁵⁶ reported the synthesis of microporous to large mesoporous alumina with higher specific surface area by a dual templating approach. These literature results along with our basic understanding of alumina as a heterogeneous support provoked us to develop convenient and simple protocol for the synthesis of alumina with proficiency of ordered multimodal pore systems. Further, a close observation of the literature result shows the presence of a huge vacuum when it comes in the case of hierarchical macro-mesoporous alumina using a single hard template. Hence, our goal is to explore this vacuum by the careful optimisation of the synthesis parameters and choosing the best templating agent to make hierarchical macroporous-mesoporous material in an easy way. Such materials are expected to show lower diffusion limitations in liquid phase reactions; especially reactions like denitrification of ground water, where the local pH around the active centre is going to decide the selectivity of the overall reaction.⁵⁷ Solvothermal conditions are widely adapted in the synthesis of porous oxide materials from centuries, since it improves some of the essential properties like hydrothermal stability, higher pore size and pore volume of the resulting materials. Likewise, a soft ageing treatment (SAT) within a

closed container is also expected to generate autogenous pressure within the synthesis medium. Thus the autogenous pressure developed inside the vessel helps in the organisation of the inorganic precursor or the micellar assembly to develop a particular morphology in the case of metal nanoparticles and hierarchical ordering in the case of porous oxides. This methodology has been widely utilised for the synthesis of mesoporous and macroporous-mesoporous materials. Yet, very little efforts are visible since most of the works directly deal with different type of supports and for different reactions. Thus a huge gap can be nullified if one can utilise this methodology to develop porous materials by suitably coupling with templated synthesis to correlate the influence of soft ageing treatment (SAT) on textural property of the material. Further, such a study could enrich the widely discussed structure-property relationship with precise and accurate data by directly drawing information's when these materials are applied as catalytic supports in diffusion limited reactions. One of the widely accepted modal reactions for studying diffusion limited catalysis in liquid phase reactions is the catalytic hydrogenation of nitrites into dinitrogen in aqueous medium.

All these efforts by different groups points to the fact that there is the necessity of an exact correlation between the influences of textural porosity of the support in tuning the activity/selectivity of a catalytic reaction by modifying the local environment around the active catalytic component. Hence, efforts have been taken to directly correlate the influence of pore network in deciding the final catalytic activity for nitrite hydrogenation by choosing amorphous porous alumina as the heterogeneous support and Pt NPs as the active catalytic phase.

To begin with, three types of porous alumina is identified for this study; specifically mesoporous, macroporous and macroporous-mesoporous alumina as supports and conclusion have made directly by correlating the physico-chemical properties of the catalysts with activity/selectivity for hydrogenation and discussed in detail in the section.4a. For further understanding the influence of textural morphology on catalytic activity, all the above discussed materials are synthesised under a soft ageing treatment (SAT, for the present study the specific SAT condition used is 80°C for different time interval; details are given in section 4b.) and used as catalysts for the same reaction under identical conditions. The material characterisations and the catalytic results are discussed in details in the section.4b. In both the section.4a and 4b conventional wet impregnation methodology is utilized for the deposition of catalytically active Pt NPs and is mentioned in the respective sections separately.

The broad classification of the work discussed in chapter.4 is as follows,

4a. Synthesis and Characterization of mesoporous, macroporous and macro-mesoporous Pt/alumina architectures and the impact of these pore systems on the catalytic hydrogenation of nitrites on a Pt/alumina catalyst

4b. Impact of the soft ageing treatment (to be defined as ageing treatment in a closed vessel at 80°C) on the textural properties of alumina and its catalytic activity for the hydrogenation of nitrites on a Pt/alumina catalyst

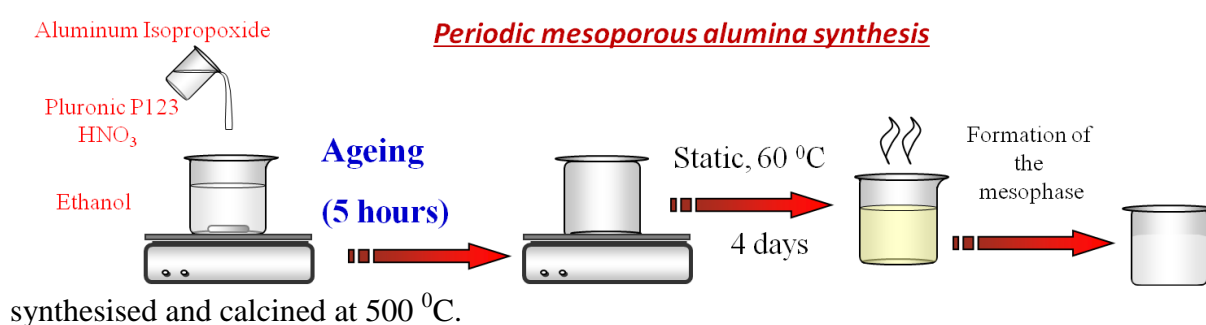
4a. Synthesis and Characterization of mesoporous, macroporous and macro-mesoporous Pt/alumina architectures and the impact of these pore systems on the catalytic hydrogenation of nitrites on a Pt/alumina catalyst

A detailed account of the various experimental conditions applied in the porous alumina synthesis, major conclusions drawn out from the support as well as Pt impregnated support and the inferences obtained after the catalytic study is presented in the following segment of the current chapter.

4a.1 Experimental Methods

4a.1.1 Periodically ordered mesoporous alumina synthesis (PMA):-

Mesoporous alumina synthesis is carried out using the evaporation induced self assembly strategy (EISA), where P123 (Sigma Aldrich) is used as the structure directing agent and aluminium isopropoxide (Sigma Aldrich) as the aluminium source. The hydrolysis and condensation rate is the pH of the solution mediated by nitric acid and the overall reaction is preceded in absolute ethanol (Sigma Aldrich). Typically, 3.12 gm of P123 is dissolved in 60 ml anhydrous ethanol followed by the addition of 4.5 ml Con. HNO₃ (69%). Once the solution becomes homogenous, 6.12 gm of Aluminium isopropoxide is added and the stirring is continued for another 5 hours. The solution is then kept in static condition at 60 °C for 4 days for ageing before calcination at 650 °C for 8 hours. Further, in order to understand the optimum calcination temperature for amorphous alumina synthesis, a representative sample is



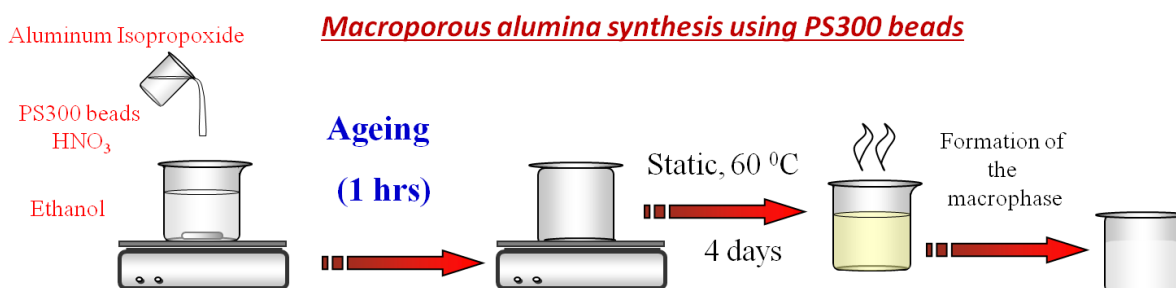
Scheme.4a.1 Periodic mesoporous alumina (PMA) synthesis by evaporation induced self assembly (EISA) methodology using P123 as the soft template

4a.1.2 Macroporous alumina synthesis (MA):-

Laboratory made polystyrene beads of dimension 300 nm is used for the synthesis of alumina with macroporous network. A detailed description of the polymer bead synthesis is given in section 4a.1.2a. Typically, for the macroporous alumina synthesis 6.12 gm of Aluminium isopropoxide is dissolved in a premixed solution of 60 ml of anhydrous ethanol and 4.5 ml Con. HNO₃ by vigorous stirring for the 1 hour. To this homogenous solution 6.2 gm of polystyrene beads are added and stirring continued for another 30 minutes. Further static condition is applied at 60 °C for 4 days of ageing before calcination at 650 °C for 8 hours.

4a.1.2a. Synthesis of monodisperse polystyrene beads (PS-300):-

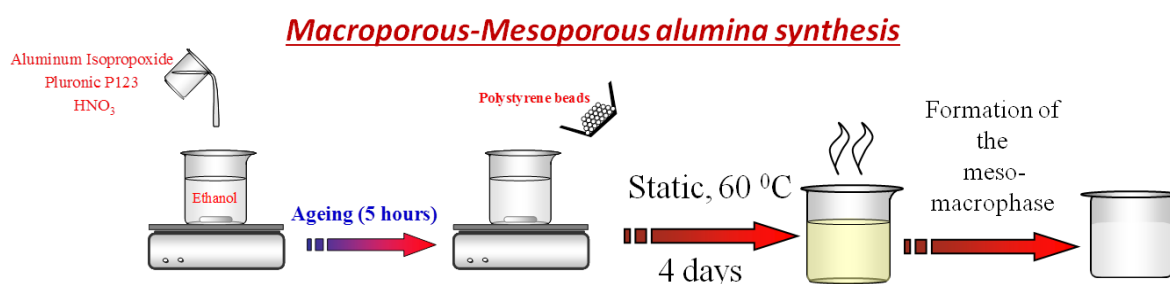
Polystyrene beads of average diameter 300 nm (PS-300) are made by adapting a previously reported procedure. Here emulsifier free emulsion polymerisation is utilised using potassium persulphate as the free radical initiator and the polymerisation is carried out at 70 °C for 15 hours. Typically, the polymerisation is carried out in a three neck round bottom flask using styrene as the monomer in aqueous medium under argon atmosphere; divinylbenzene is used as the cross linker for making compact spherical polystyrene beads. Prior to polymerisation process the styrene monomer (25 ml, Merk) mixed with divinylbenzene (4.5 ml, Sigma Aldrich) is washed with 0.1M NaOH (100 ml) and then with water (100 ml). The washed mixture then transferred into the RB flask with 240ml of distilled water at 70 °C. The mixture is stirred for 1 hr with moderate speed (250 rpm) and then potassium persulphate solution is added (83 mg dissolved in 10ml distilled water; Sigma Aldrich), and stirring continued for another 15 hrs. The beads recovered by filtration and dried at 80 °C overnight and used as the hard template for the hierarchical alumina synthesis.



Scheme.4a.2 Macroporous alumina (MA) synthesis by evaporation induced self assembly (EISA) methodology using polystyrene beads of dimension 300 nm as the hard template

4a.1.3 Macroporous-mesoporous alumina synthesis (MMA):-

For the synthesis of macroporous-mesoporous alumina, the previously reported procedure is slightly modified and used.⁵¹ Typically, 3.2 gm Pluronic P123, 4.5 ml Con.HNO₃, 6.12 gm of aluminium isopropoxide is added respectively into 60 ml anhydrous ethanol and stirred for 5 hours. 6.2 gm of polystyrene beads are added followed by vigorous stirring for 30 minutes. Then the solution is aged for 4 days at 60 °C in static conditions before calcination at 650 °C for 8 hours.



Scheme.4a.3 Periodic macroporous-mesoporous alumina (MMA) synthesis by evaporation induced self assembly (EISA) methodology using P123 as well as polystyrene beads of dimension 300 nm in a co-templating strategy

4a.2. Pt impregnated meso, macro and macro-mesoporous alumina

The conventional wet impregnation method is used for the impregnation of the active metal, Pt in the amorphous alumina synthesized and tested the catalytic activity for denitrification reactions. Typically, 1 wt% of the Pt metal is impregnated by the slow evaporation of an aqueous solution of the hexachloroplatinic acid (Sigma Aldrich) on the support using a rotary evaporator under controlled conditions starting from 50 °C and 80 mbar pressure to 60 °C and 60 mbar pressure over a period of 3 hrs. Then it is dried and calcined at 400 °C for 8 hours under static air. Prior to catalytic test, the samples are reduced under 5% hydrogen diluted with helium for 4 hours at 450 °C with a ramping rate of 2 °/min.

4a.3 Catalytic test: - Nitrite Hydrogenation using Hydrogen gas as reducing agent

The catalytic nitrite reduction is carried out at 24 ±0.5 °C in a three neck round bottom flask. Ultrapure water degassed for 1 hour is used throughout the experiment for preparing the standards as well as making eluents in order to avoid the influence of any residual ions on the activity and selectivity measurement of the current study. In a typical test, 75 mg of the catalysts with grain size 100-250 micrometer is charged into the reaction vessel connected

with the hydrogen inlet, and pure hydrogen gas is passed over the catalyst for 1 hr at 25 ml/min under magnetic stirring of 330 rpm. Then 40 ml of the degassed ultra pure water is added (caution:- hydrogen flow should be stopped to avoid any accidents) stirred at 800 rpm and the whole solution is purged with pure hydrogen gas at 100 ml/min for another 2 hours to remove any remnant dissolved oxygen in the water. To this, 10 ml of the Potassium nitrite (Sigma Aldrich) solution is added to maintain an initial nitrite concentration of 100 ppm in the reaction medium. At periodic time intervals samples removed from the medium and analysed using ion chromatography for the nitrite (NaOH and Na₂CO₃ eluents) and ammonium ions (HNO₃ as eluent) in the samples. The catalyst performance was evaluated by following the time dependent variation in the concentration of the nitrite and ammonium ions using the following equations,

$$\text{NO}_2^- \text{ conversion (\%)} \quad X_{\text{NO}_2^-} = \{([\text{NO}_2^-]_i - [\text{NO}_2^-]_t) / [\text{NO}_2^-]_i\} \times 100$$

$$\text{Selectivity towards NH}_4^+ \text{ (\%)} \quad S_{\text{NH}_4^+} = \{[\text{NH}_4^+]_t / ([\text{NO}_2^-]_i - [\text{NO}_2^-]_t)\} \times 100$$

$$\text{Selectivity towards N}_2 \text{ (\%)} \quad S_{\text{N}_2} = \{([\text{NO}_2^-]_i - [\text{NO}_2^-]_t - [\text{NH}_4^+]_t) / ([\text{NO}_2^-]_i - [\text{NO}_2^-]_t)\} \times 100$$

4a.4 Results and discussions:-

4a.4.1. Amorphous alumina (PMA, MA and MMA) support characterisations

4a.4.1a. Thermogravimetric analysis

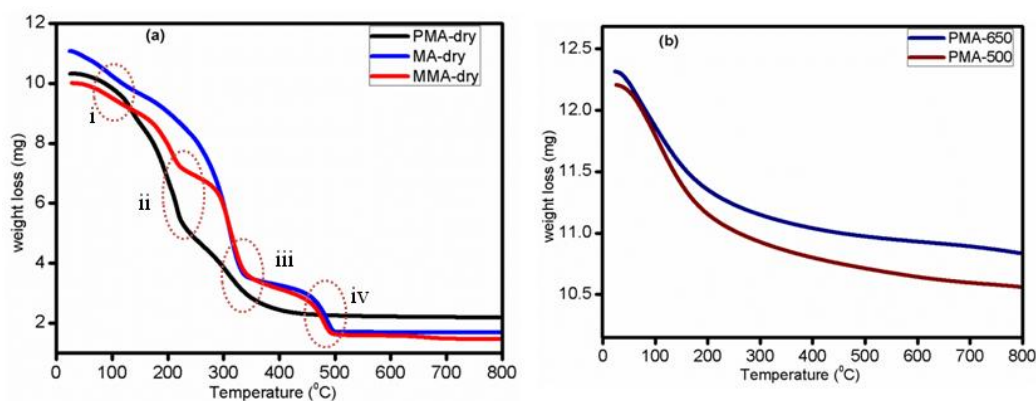


Figure.4a.1 Thermogravimetric analysis of the as-synthesised samples (a) and the comparison of the thermal stability of the periodic mesoporous alumina calcined at two different temperatures (b)

The synthesised material is having higher thermal stability as indicated by the absence of any weight loss at higher temperature (Figure.4a.1). Further, the weight loss at higher temperature for MA indicates the complete removal of the polystyrene beads from the alumina matrix. Similarly, there is the contribution of both the hard and soft templates in the weight loss of the macro-mesoporous counterpart MMA synthesised at lower temperature as well as the higher temperature. The TGA graph 4a.1a. can be divided into four regions based on the weight loss; region i corresponds to the adsorbed moisture/impurities, region ii corresponds to the weight loss from the soft template P123, regions iii and iv are from the weight loss from the hard templated polystyrene used in the synthesis. It can be noted that the region i is present in the all the samples analysed for TGA irrespective of the components used. Region ii is present only where the soft template P123 is used in the synthesis strategy, namely PMA and MMA samples. Likewise the weight loss corresponding to polystyrene beads removal in region iii and iv is present only in the MA and MMA samples. The TGA analysis also justifies the higher temperature calcination which is used in the current study. From the TGA analysis one can easily conclude a calcination temperature of 500 °C is sufficient for our reference material, PMA; where as a slightly higher temperature will be appreciable for the macroporous and macro-mesoporous alumina. Yet, the TGA analysis of the reference material PMA calcined at two temperatures specifically at 500 (PMA-500) and 650 °C (PMA-650) will self explain the necessity of the high temperature calcination used in the current study. The higher initial weight loss from PMA-500 could be the removal of the carbonaceous content trapped inside the porous alumina material during the low temperature calcination under static conditions. Still it should be interesting to note that the overall weight loss during the TGA analysis was approximately 15 % for the PMA samples calcined at different temperatures. Since open porosity is a necessary attribute for any catalytic support, the higher temperature calcination is continued throughout for our meso, macro and meso-macroporous assembly of materials in this study.

4a.4.1b. X-ray diffraction Analysis:-

The amorphous nature of the synthesised material is clearly evident from the wide angle spectra of all the synthesised materials, as there is complete absence of any diffraction peak from the crystalline alumina phase. At the same time, considerable amount of periodicity is maintained in the samples, which is indicative from the low angle XRD spectra for the high temperature calcined sample namely PMA-650 (Figure.4a.2).

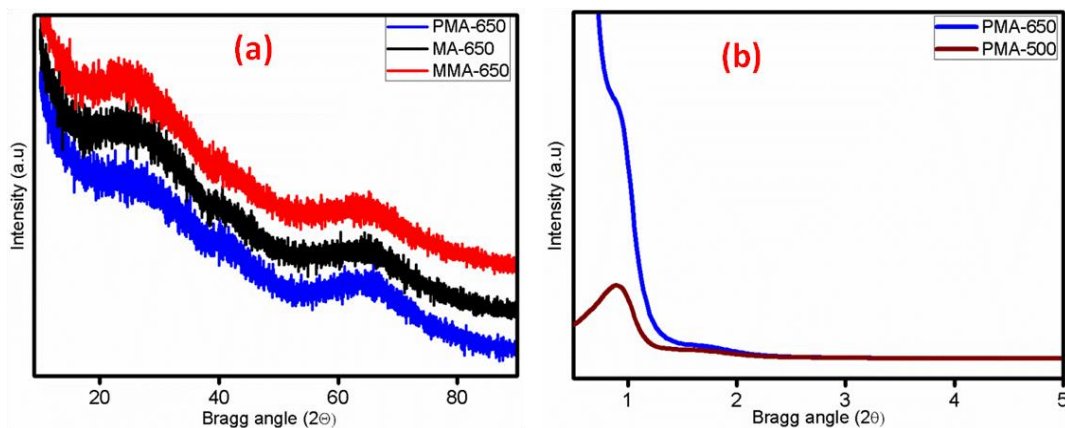


Figure.4a.2 Wide angle X-ray diffraction pattern of alumina synthesised by different methods (a) and (b) the small angle xrd of the mesoporous alumina calcined at two different temperatures

The macro and macro-mesoporous alumina materials calcined does not show any diffraction peak in the small angle x-ray diffraction analysis as expected due to the lack of periodic ordering in their mesoporosity. Physisorption method can tell more about the extent of porosity of the synthesised materials, hence analysed using N_2 as the probe molecule and the discussion is as follows,

4a.5.1c. Surface area analysis by nitrogen physisorption method:-

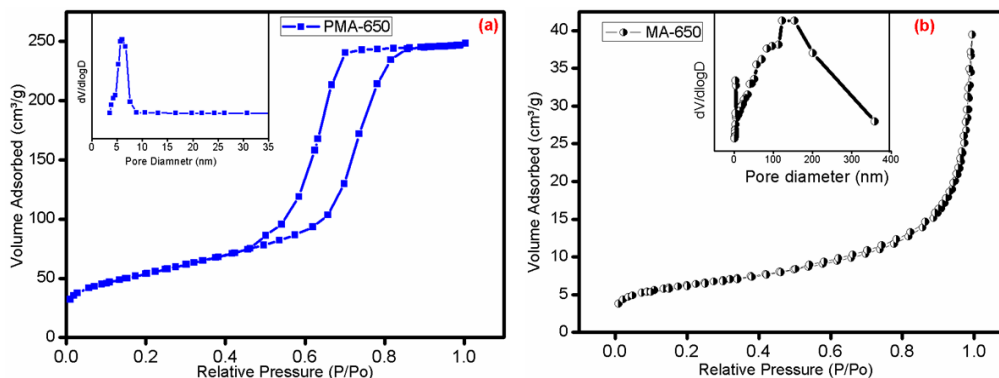


Figure.4a.3 N_2 adsorption desorption isotherm of the different types of calcined alumina samples as well as the pore size distributions (a) PMA-650 and (b) MA-650

Structural as well as textural porosity of all the synthesised materials are clearly shown in Figure.4a.3. The mesoporous material calcined at $650^\circ C$ shows type IV isotherm with H1 type of hysteresis loop, indicative of the presence of uniform type of mesopores in the material.⁵⁸ At the same time, the MA-650 almost linear for a wide range of relative pressures and there is minimum uptake of the adsorbate at relatively higher pressure region and showing a surface area of $20\text{ m}^2/\text{g}$ compared to that of the PMA-650 as $222.27\text{ m}^2/\text{g}$. The

pore size distribution data obtained from the desorption branch of the BJH analysis revealed the existence of large mesoporous windows in an otherwise pure macroporous material (more discussions later on SEM). It is interesting to note that there is a smaller fraction of mesopores generated in the MA-650 samples other than the larger macroporous windows when compared with the pure mesoporous counterpart PMA-650.

Table 4a.1 The physico-chemical properties for various alumina support after calcination at 650 °C

No.	Sample Name	BET surface area (m ² /g)	Average Pore diameter* (nm)	Pore volume (cc/g)
1.	PMA-650	222.27	6.26	0.51
2.	MA-650	20	13	0.06
3.	MMA-650	195	5.2	0.49

*Calculated from the desorption branch of the BJH analysis

The large mesoporous windows generated can be considered as the advantage of the evaporation induced self assembly approach, as the segregation of the polymer beads during the synthesis can develop large intra particle spaces. A careful tuning of the synthesis time, temperature and precursor to polymer ratio are very essential in order to generate such a close packing in solution phase. The high temperature controlled calcination after the ageing process has resulted in the complete removal of the polystyrene beads (see SEM, Figure.4a.5), leaving the inter particle spacing in an organised way in between the macroporous alumina framework. Thus a careful optimisation of the synthesis condition helps to generate an extended level of porosity in our macroporous material. This kind of interconnected pore network is expected to enhance the catalytic dynamics by reducing the mass transfer limitations when tested in realistic conditions, thus positively contributing towards the applicability as well as the recyclability of the catalytic systems under considerations.

4a.4.1d. Microscopy analysis:- Scanning Electron Microscopy

The synthesised polystyrene beads have been characterised using a scanning electron microscope to verify the monodispersity as well as the bead size, so that introduction of macroporosity can be easily understood in terms of the polystyrene beads size and shape. It is

very clear from Figure 4a.4 that the polystyrene beads are monodisperse with spherical shape and particle size 300 nm.

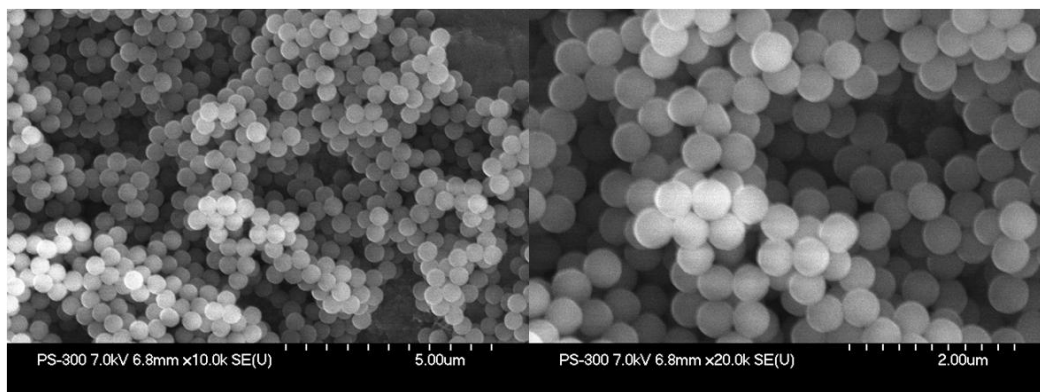


Figure.4a.4 SEM analysis of the Polystyrene beads synthesised with various magnifications

Similarly, in order to understand the three dimensional morphology of the synthesised macroporous alumina (MA-650), scanning electron microscopy analysis is carried out. It is evident from the Figure.4a.5 the presence of large mesoporous windows connecting the macropores, which is matching with the pore size distribution graph (Figure.4a.3) discussed earlier. The ordered arrangement of the polystyrene beads during the EISA approach has generated inter particle spacing around which alumina is grown in micro meter dimensions. A controlled calcination step resulted in the removal of the template leaving the structural frame work intact. An easy transport of the reactants and products can be visualised in such a material, making it an ideal candidate for liquid phase catalysis as a catalytic support.

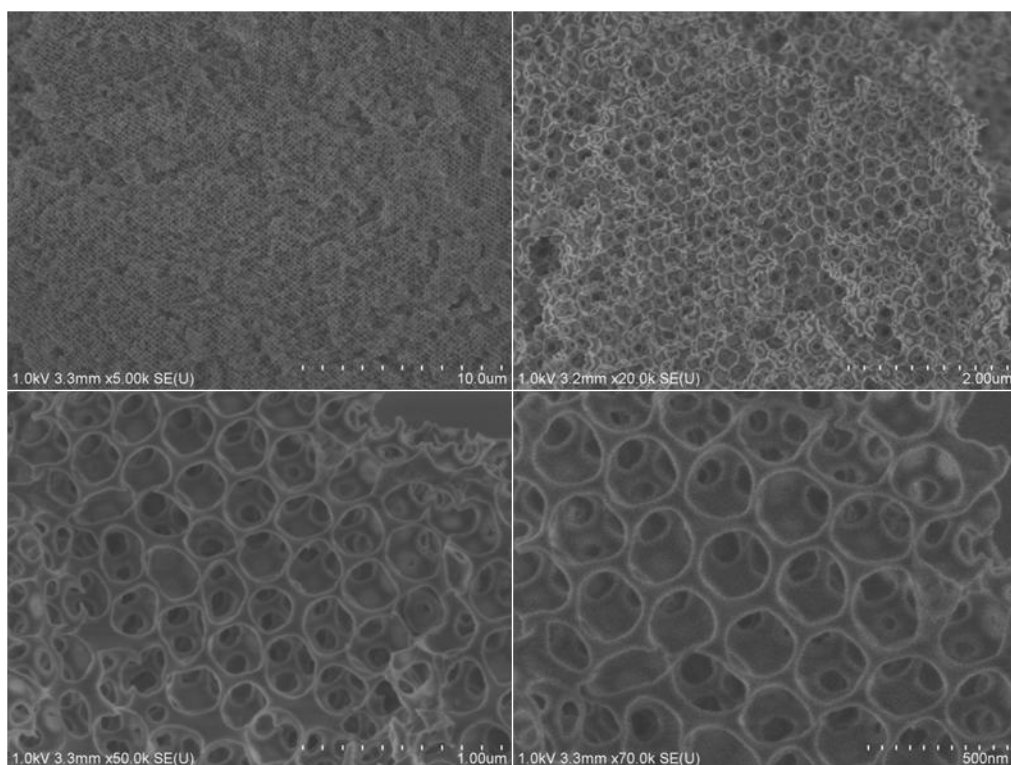


Figure.4a.5 SEM images of the MA-650 at different magnifications

Similarly the MMA-0 sample also shows a hierarchical order in 3D under a scanning electron microscope and the presence of mesoporous walls on the macroporous system is more visible under a transmission electron microscope and is discussed in the following section.

4a.4.1e. Transmission Electron Microscopy analysis

The mesoporous nature of the walls is well established in the case of the MMA-650 sample as well as the PMA-650 sample under the transmission electron microscope. The soft template P123 assembles in a hexagonal fashion during the EISA strategy used in the current study and results in the formation of hexagonally oriented mesopores in the case of PMA-650; more over the ordered arrangement in the pore network is reflected in the small angle x-ray diffraction analysis of the mesoporous alumina (PMA-650) system (see Figure.4a.2). In the MMA-650 system such an extent of mesoporous ordering is not observed, yet the high resolution TEM analysis helps to conclude the existence of mesopores on the macroporous walls after the high temperature calcination (Figure.4a.6).

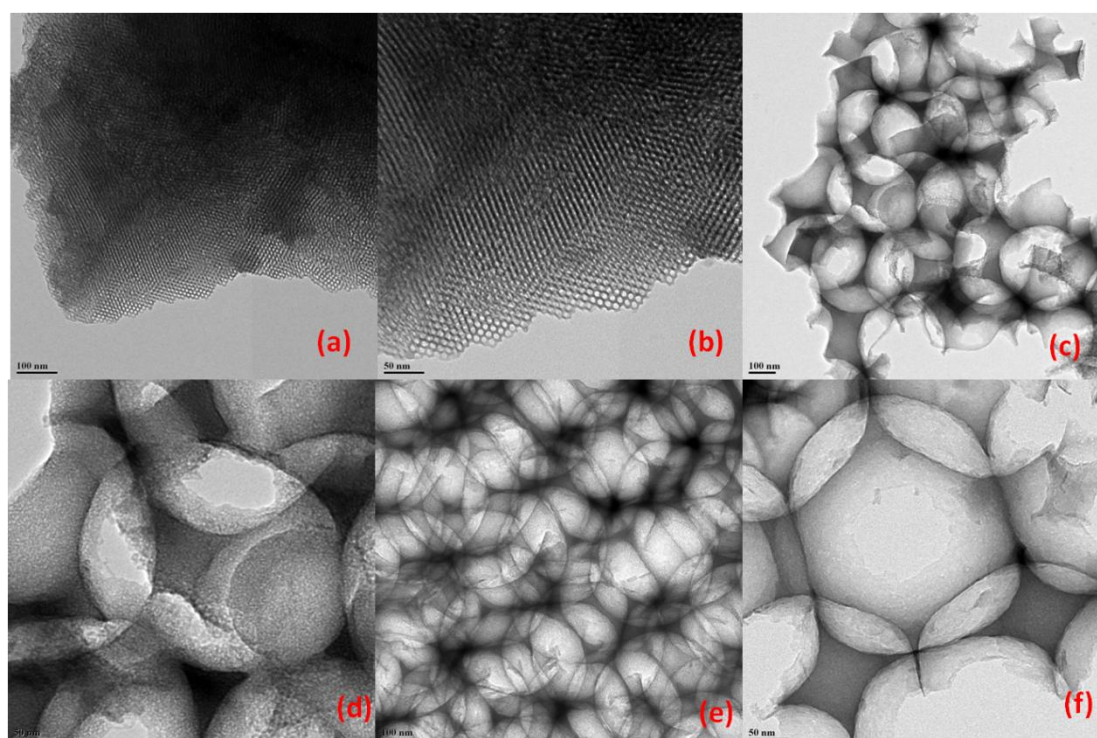


Figure.4a.6. Transmission electron microscopy images of calcined samples PMA-650 (a and b), MMA-650 (c and d) and MA-650 (e and f) samples

The presence of interpenetrating voids is clearly visible in the TEM analysis of the sample MA-650 (Figure.4.6e and f), directly supporting the N_2 porosimetry analysis where mesoporous windows are observed. Thus a minute amount of the mesoporosity is also expected in the MA-650 material as per the TEM as well as textual analysis data.

4a.4.2. 1 wt% Pt supported catalyst (Pt-PMA, Pt-MA and Pt-MMA) characterisations

4a.4.2a. X-ray diffraction analysis

The impregnated samples xrd pattern doesn't show any characteristic features of Pt in the material for all the samples, which is quiet expected since the intended metal loading was only 1 wt% indicative of the fairly good dispersion as well as smaller crystallite size for the impregnated Platinum. The broad diffraction peaks in the Pt-PMA and Pt-MMA (Figure.4a.7) can be due to the transformation of the some of the alumina crystallites into the gamma alumina structure (JCPDF #75-0921) during the impregnation followed by calcination at 400 °C. Such a phase transition from amorphous to partially crystalline nature at lower temperature calcination after wetting is previously been reported by many groups in case of alumina synthesised by non-hydrolytic sol gel route,⁵⁹ a method almost similar to our synthesis protocol. Still the single hard templated Pt-MA sample retains complete x-ray

amorphous nature after the impregnation, though it also showed the increase in surface area like the other two samples. The reduced samples also showed a similar xrd pattern without any characteristic peak for platinum indicating the fine dispersion as well as smaller particle size of the dispersed platinum nanoparticles even after the high temperature reduction for 4 hrs.

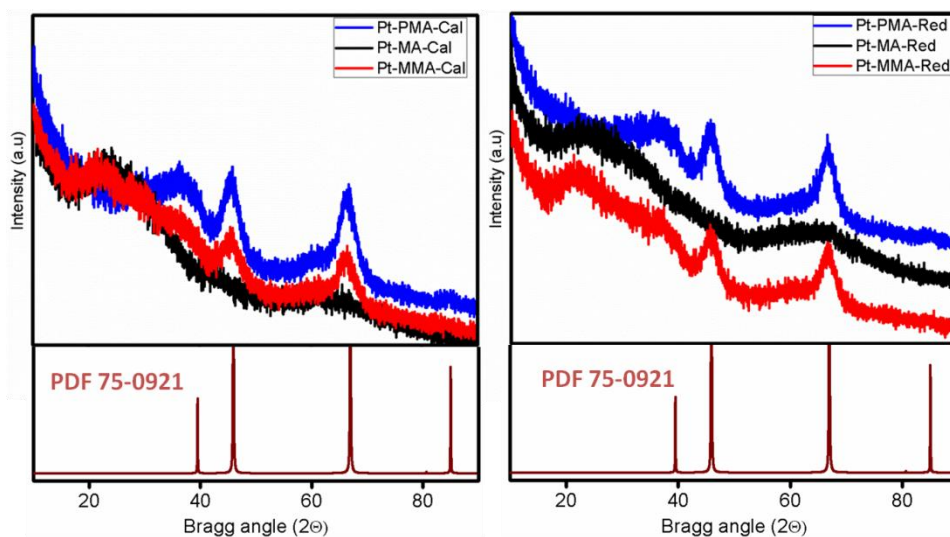


Figure.4a.7 wide angle X-ray diffraction patterns of the pt impregnated alumina samples after calcination at 400 °C (left) and the samples reduced at 450 °C after calcination (right). γ -alumina (PDF 75-0921) xrd pattern is appended in the same graph for clarity in understanding the diffraction peaks

4a.4.2b. N₂ physisorption analysis

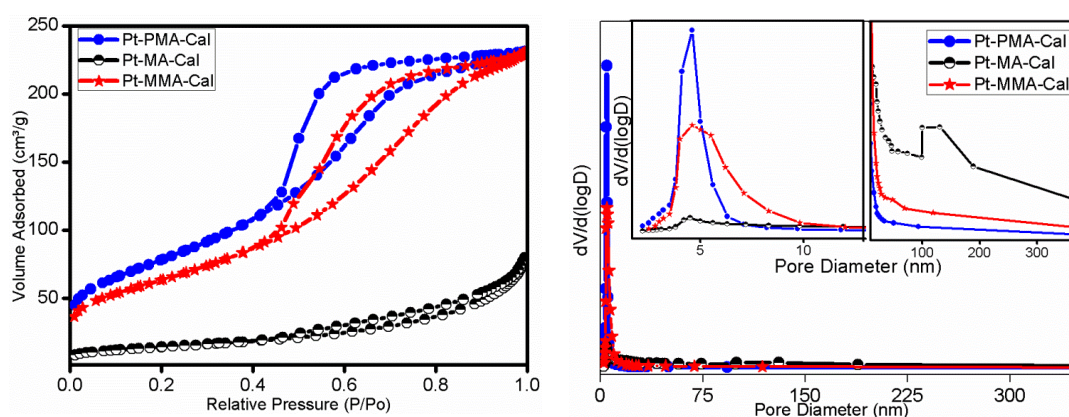


Figure.4a.8 Surface area (left) and pore size distribution analysis (right) of the materials after Pt impregnation and calcination. For a better understanding of the hierarchical pore system in the single hard templated alumina see inset of the figure.

The surface area analysis of the impregnated samples all exhibited capillary condensation, a phenomenon commonly observed in the mesoporous materials.⁵⁸ Pt-MA-Cal samples showed very weak capillary condensation and showed very less surface area when compared to the other two standard references used in this study. Still the pore size distribution analysis from the desorption branch of the BJH analysis indicates the presence of large porous windows connected to the smaller mesopores in the case of our hierarchical macro-mesoporous alumina even after Pt impregnation (Figure.4a.8). A close observation of the physisorption analysis data shows an increase in the surface area along with the decrease in the pore size distribution of all the synthesized samples. A similar trend is observed by Grader and co-workers during their study on the solvent treatment⁶⁰ on alumina, but in our case the increase in surface area was 25% and above. A more detailed study is needed to completely understand the actual reason for this increase in surface area, yet the one possible explanation could be the widely discussed dissolution- reprecipitation phenomenon of the alumina as the reason for the increase in the surface area. The remnant organic burn off which is considered as the alternate reason for the increase in surface area after impregnation and subsequent calcination can be neglected based on our TGA data, dealt in the previous section 4a.4.1a.

Table.4a.2. Physisorption analysis results of the support and Pt impregnate samples after calcination.

No.	Sample Name	BET surface area (m ² /g)	Average diameter* (nm)	Pore	Pore volume* (cc/g)
1.	PMA-650	222.27	6.26		0.51
2.	MA-650	20	13		0.06
3.	MMA-650	195	5.92		0.49
4.	Pt-PMA-650	284.83	4.00		0.43
5.	Pt-MA-650	50.58	8.06		0.13
6.	Pt-MMA-650	230.10	4.71		0.43

*Calculated from the desorption branch of the BJH analysis

4a.4.2c. Microscopy analysis

The Pt incorporated samples showed almost similar structural morphology when compared with the alumina support before impregnation in the case of PMA-650 and MA-650 samples.

4a.5 Catalytic test results:-

The 1 wt% Pt loaded samples are tested for its applicability as a catalyst for the hydrogenation of nitrite using molecular hydrogen as a reducing agent in aqueous medium. It

was found that all the samples are active for this particular reaction, but the most desirable product the dinitrogen selectivity varies based on the textural morphology of the support. It is evident from Figure.4a.9 that the co-operative assembly of mesoporosity with macroporosity can essentially change the selectivity for any diffusion limited reactions in liquid phase catalysis. In the present nitrite hydrogenation reaction it is well documented that the higher pH near the active phase Pt NPs can influence the kinetics of the overall reaction. It is evident from Figure.4a.9b that even though the Pt-MA-650 sample which is expected to show small mesoporous windows (see Figure.4a.5, 4a.6e. and 4a.6f) as well as in the surface area analysis, the nitrogen selectivity is lesser when compared to its mesoporous counterpart Pt-PMA sample. Similarly from Figure.4a.9a it is evident that the conversion is also dependent on the textural property of the support alumina as Pt-MMA-650 is more active and selective after the reduction treatment at 450 °C.

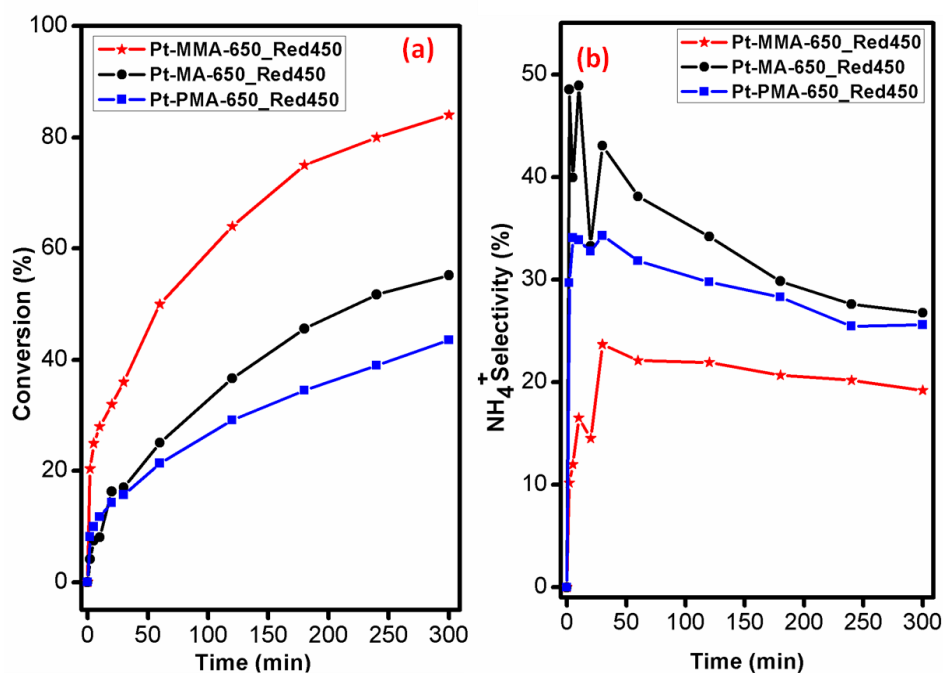


Figure.4a.9 The time dependent catalytic activity results for the nitrite reaction using the various Pt supported alumina catalysts under 1 bar hydrogen at room temperature. (a) Conversion and (b) ammonia selectivity

Here, the higher activity of the Pt-MMA-650 can be attributed to the co-operative existence of the macroporous and mesoporous nature of the support alumina. The larger macroporous windows help in the easy diffusion of the reactant as well as products whereas the mesopores helps in the stabilisation of the smaller Pt NPS along with better exposure of the active centres for reactions. Thus the current study helps one to directly observe the experimental

evidence to prove the much acclaimed concept; influence of support morphology on catalytic activity/selectivity.

4b. Impact of the soft ageing treatment (to be defined as ageing treatment in a closed vessel at 80°C) on the textural properties of alumina and its catalytic activity for the hydrogenation of nitrites on a Pt/alumina catalyst

A complete description of the soft ageing treatment (SAT) carried out on porous alumina synthesis, its comprehensive characterisation details and its catalytic applicability as heterogeneous support for Pt NPs in fine tuning the selectivity is given in the following segment of the current chapter.

4b.1 Experimental Methods

4b.1.1 Hierarchical macroporous and macroporous- mesoporous alumina synthesis

4b.1.1a. Hierarchical Macroporous alumina synthesis by using PS-300 beads as a hard template:-

Laboratory made polystyrene beads of dimension 300 nm is used for the synthesis of macroporous alumina with hierarchical pore network. A detailed description of the polymer bead synthesis is given in the previous section 4a.1.2a. Typically, for the macroporous alumina synthesis 6.12 gm of aluminium isopropoxide is dissolved in a premixed solution of 60 ml of anhydrous ethanol and 4.5 ml Con. HNO₃ by vigorous stirring for the 1 hour. To this homogenous solution 6.2 gm of polystyrene beads are added and stirring continued for another 30 minutes. A soft ageing treatment along with sedimentation aggregation method is utilised further to arrange the polystyrene beads in the solution phase for the development of alumina oligomers on the surface of the organised beads. Depending on the soft ageing treatment time the materials are labelled as MA-X, where X varies from 0 to 48 hrs. Further static condition is applied at 60 °C for 4 days of ageing before calcination at 650 °C for 8 hours.

4b.1.1b. Hierarchical macroporous-mesoporous alumina synthesis using a dual templating strategy with P123 as soft template and PS-300 beads as hard template

For the synthesis of macroporous-mesoporous alumina, literature reported method⁵¹ is slightly modified and used. Typically, 3.2 gm Pluronic P123, 4.5 ml Con.HNO₃, 6.12 gm of aluminium isopropoxide is added respectively into 60 ml anhydrous ethanol and stirred for 5 hours. 6.2 gm of polystyrene beads are added followed by vigorous stirring for 30 minutes. A soft ageing treatment coupled with sedimentation aggregation method is utilised further to arrange the polystyrene beads in the solution phase for the development of alumina oligomers on the surface of the organised beads. Depending on the SAT ageing time the materials are labelled as MMA-X, where X varies from 0 to 48 hrs. Then the solution is aged for 4 days at 60 °C in static before calcination at 650 °C for 8 hours.

4b.1.2. Pt impregnation on the above synthesised supports

The conventional wet impregnation method is used for the impregnation of the active metal in the amorphous alumina synthesized and tested the catalytic activity for denitrification reactions. Typically, 1 wt% of the metal is impregnated by the slow evaporation of an aqueous solution of the hexachloroplatinic acid (Sigma Aldrich) on the support using a rotary evaporator under controlled conditions starting from 50 °C and 80 mbar pressure to 60 °C and 60 mbar pressure over a period of 3 hrs. Then it is dried and calcined at 400 °C for 8 hours under static air. Prior to catalytic test, the samples are reduced under 5% hydrogen diluted with helium for 4 hours at 450 degC with a ramping rate of 2 deg/min.

4b.2. Catalytic test:- Nitrite hydrogenation reaction

The catalytic nitrite reduction is carried out at 24 ±0.5 °C in a three neck round bottom flask. Ultrapure water degassed for 1 hour is used throughout the experiment for preparing the standarder as well as making eluents in order to avoid the influence of any residual ions on the activity and selectivity measurement of the current study. In a typical test, 75 mg of the catalysts with grain size 100-250 micrometer is charged into the reaction vessel connected with the hydrogen inlet, and pure hydrogen gas is passed over the catalyst for 1 hr at 25 ml/min under magnetic stirring of 330 rpm. Then 40 ml of the degassed ultra pure water is added (caution:- hydrogen flow should be stopped to avoid any accidents) stirred at 800 rpm and the whole solution is purged with pure hydrogen gas at 100 ml/min for another 2 hours to remove any remnant dissolved oxygen in the water. To this, 10 ml of the Potassium nitrite (Sigma Aldrich) solution is added to maintain an initial nitrite concentration of 100 ppm in the reaction medium. At periodic time intervals samples removed from the medium and

analysed using ion chromatography for the nitrite (NaOH and Na₂CO₃ eluent) and ammonium ions (HNO₃ as eluent) in the samples. The catalyst performance was evaluated by following the time dependent variation in the concentration of the nitrite and ammonium ions using the following equations,

$$\text{NO}_2^- \text{ conversion (\%)} \quad X_{\text{NO}_2^-} = \{([\text{NO}_2^-]_i - [\text{NO}_2^-]_t) / [\text{NO}_2^-]_i\} \times 100$$

$$\text{Selectivity towards N}_2 \text{ (\%)} \quad S_{\text{N}_2} = \{([\text{NO}_2^-]_i - [\text{NO}_2^-]_t - [\text{NH}_4^+]_t) / ([\text{NO}_2^-]_i - [\text{NO}_2^-]_t)\} \times 100$$

4b.3. Results and discussions

4b.3.1. Hierarchical macroporous alumina (MA-X) synthesised by soft ageing treatment method and its catalytic activity

4b.3.1a. Thermogravimetry and XRD analysis of the macroporous alumina synthesised by hard templating approach (The MA-X series)

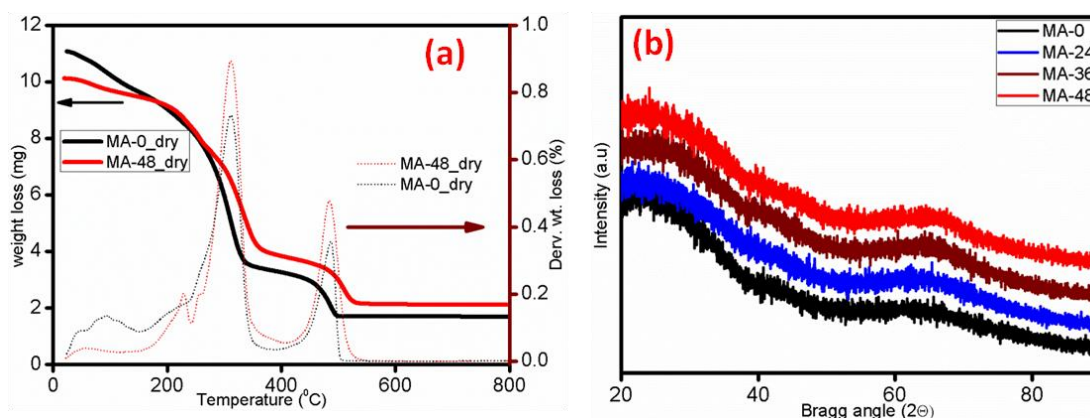


Figure.4b.1 Thermogravimetry analysis of the samples made with and without soft ageing treatment, MA-X (X is the SAT ageing time) (a) and the wide angle xrd analysis of the sample (b)

In the thermogravimetry analysis of the samples with extremely different synthesis condition is compared in Figure.4b.1a, showing two sharp weight losses even though only single hard template is used during the synthesis. Further, the TG-DTA result supports our high temperature calcination during the support alumina synthesis. The higher temperature removal of polystyrene can be considered as the strong interaction with the alumina oligomers during the synthesis stage, though there is not much change in the decomposition temperature as a function of hydrothermal ageing time. It should be noted that the synthesised materials are amorphous as seen from the wide angle x-ray analysis represented in

Figure.4b.1b. The high temperature calcination at 650 °C under static air is based upon the TGA analysis as well as our previous experience with alumina synthesis discussed in chapter 4a.

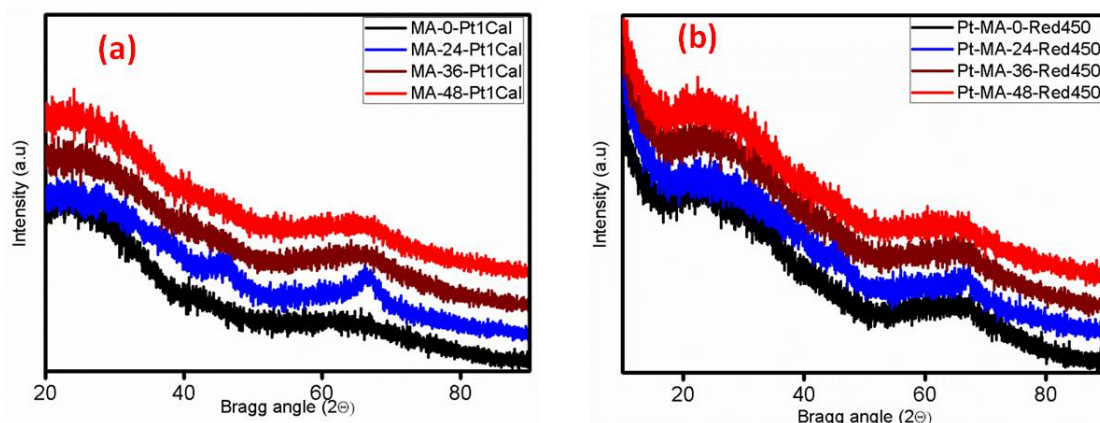


Figure.4b.2 Wide angle xrd pattern of the macroporous alumina after Pt impregnation followed by calcination (a) and Reduction at 450 °C (b)

Further, the stability of the material is exemplified by the x-ray diffraction analysis of the Pt impregnated calcined as well as reduced samples (Figure.4b.2). The absence of any observable Pt feature in the x-ray analysis indirectly points to smaller crystallite size as well as better dispersion of Pt nanoparticles on various macroporous alumina synthesised.

4b.3.1b. Surface area analysis

All the synthesised materials showed the phenomenon of capillary condensation exemplifying the existence of mesoporosity in them, which is further supported by the pore size distribution analysis. As the soft ageing treatment time at 80 °C increases, there is a considerable increase in the pore size of the materials from MA-0 to MA-48. Simultaneously there is a decrease in the density of the large macroporous windows from 105 nm in MA-0 to 0 nm in MA-48. The increase in the mesoporous diameter as the soft ageing treatment time increases can be correlated to the ordered arrangement of the polystyrene beads under the autogenous pressure generated in the autoclave/polypropylene bottle over a period of 0 to 48 hrs. An increase in the ageing time results in the close packed arrangement of the of the PS beads covered with the alumina oligomers which leads to the formation of interpenetrating alumina walls after the higher temperature calcination (Scheme.4b.1). This phenomenon

contributes the formation of large unimodal mesopores from 4.2 to 16.5 nm from MA-0 to MA-48 at the cost of the macroporosity.

Table.4b.1. Physico-chemical properties of the support as well as Pt-impregnated and calcined catalysts

Samples	BET surface area (m ² .g ⁻¹)	Macropore size (nm)	Window size (nm)	Mesopore size (nm)	Pore Volume (cm ³ .g ⁻¹)	Morphology
MA-0	20	252	105	-	0.06	Ordered Honeycomb
MA-24	22	20	72	4.2	0.10	Disordered Honeycomb
MA-36	122	-	-	7.7	0.50	Aggregates
MA-48	183	-	-	11.9	0.92	Aggregates
Pt-MA-0	50	241	98	4.3	0.13	Ordered Honeycomb
Pt-MA-24	55	201	82	4.2	0.12	Disordered Honeycomb
Pt-MA-36	182	-	-	6.1	0.44	Aggregates
Pt-MA-48	350	-	-	5.9	0.65	Aggregates

This decrease in the number density of the large mesopores/macropores windows will have profound impact on the overall mass transfer during any catalytic cycles. It is clearly observable that there is an increase in the surface area of all the materials after Pt impregnation and calcination irrespective of the soft ageing treatment time. The increase in surface area is resulted from the increase in the mesoporosity which is evident from the pore size distribution graph in Figure.4b.4.

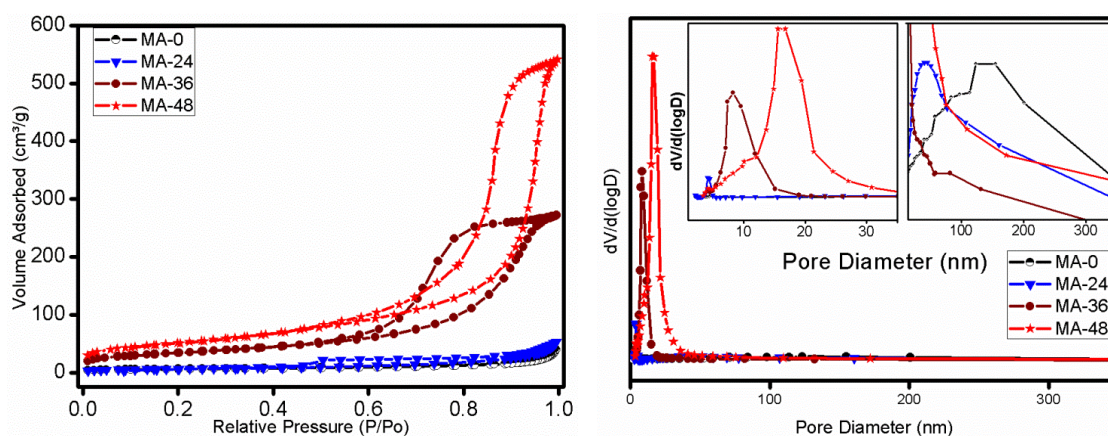


Figure.4b.3 Surface area analysis of the hierarchical macroporous alumina with varying soft ageing treatment time MA-X (X is the SAT time) (left) and the corresponding pore size distribution graph (for clarity the small mesopores and large pores windows are shown in inset) (right)

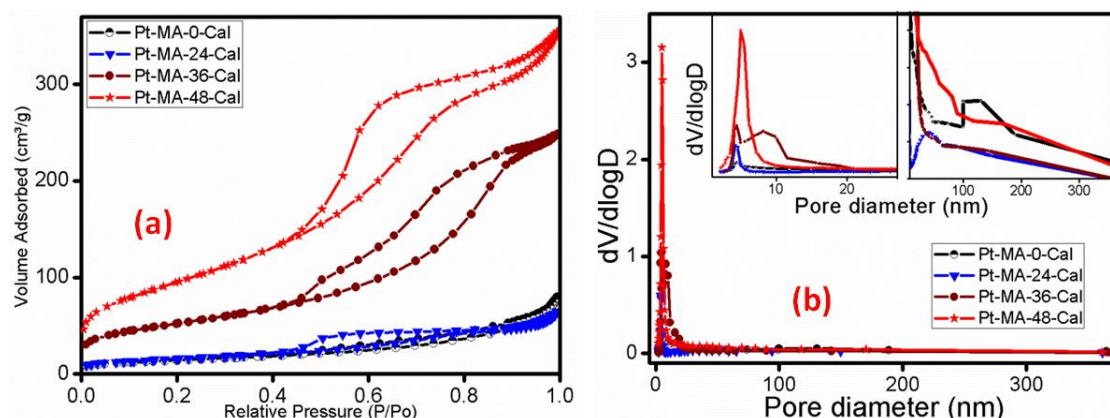


Figure.4b.4. Surface area (a) and pore size distribution (b) analysis of the hierarchical macroporous alumina after Pt impregnation and calcination

4b.3.1c. Scanning Electron Microscopy analysis of the MA-X samples

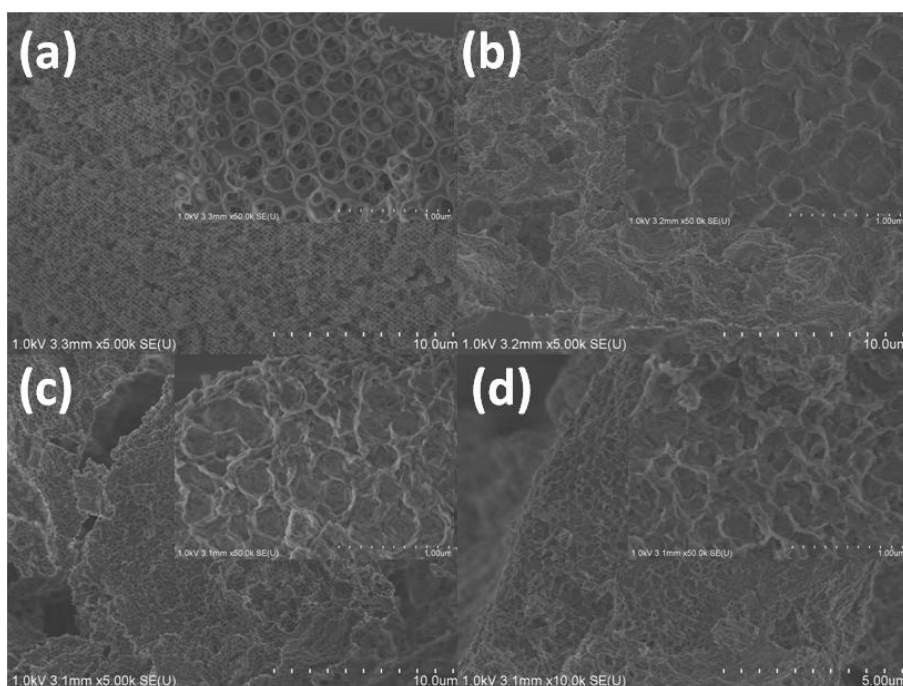
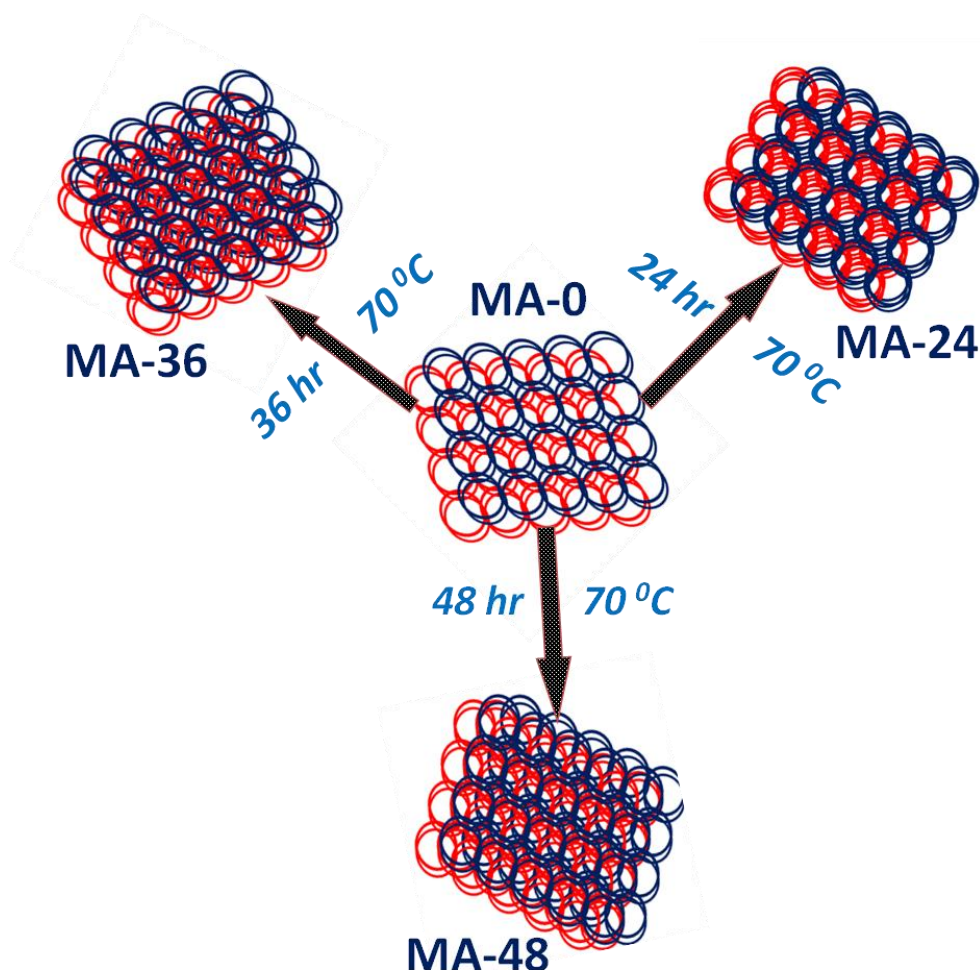


Figure.4b.5. Scanning electron microscopy image of the (a) MA-0 (b) MA-24 (c) MA-36 and (d) MA-48 samples (high resolution images are shown in the inset of each figure)

The influence of Soft ageing treatment on the surface morphology of the materials is characterised by Scanning electron microscopy shown in Figure.4b.5. The interconnected pores windows are clearly visible in the MA-0 materials and which loses with SAT time. The change in surface morphology from macroporous to highly rough surface is clearly

observable from the SEM analysis and in the case of MA-48 samples a complete loss of the macro structural ordering is visible.

The development of the interpenetrating arrangement of the polystyrene beads with the increase in soft ageing treatment time can be visualised from the surface area as well as pore size distribution curve, Figure.4b.3. A correlation of the SEM images with the N₂ physisorption analysis results leads to the conclusion that there is a collapse of the macroporous structure yielding larger mesoporous character in an otherwise perfectly macroporous material as the SAT time increases (Scheme.4b.1). The improved mesoporous character with the loss of macroporous nature and its impact on the catalytic activity is discussed in detail in the catalytic test results.



Scheme.4b.1 Evolution of mesoporous nature in the hierarchical macroporous-mesoporous alumina by varying soft ageing treatment time

4b.3.1d. Transmission Electron Microscopy analysis of the MA-X samples

In order to understand the microscopic change in the surface morphology of the support material MA-X as well as to understand the geometric change in the active component Pt NPs, transmission electron microscopy analysis of the samples has been done after Pt impregnation. A representative image for the TEM analysis of the samples were Pt supported on extremely different soft ageing treated MA-X (Pt-MA-0 and Pt-MA-48) samples is shown in Figure.4b.6.

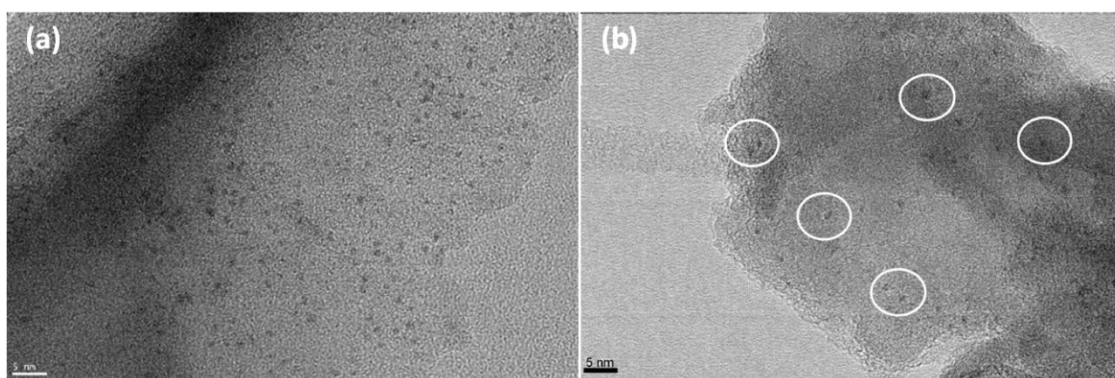


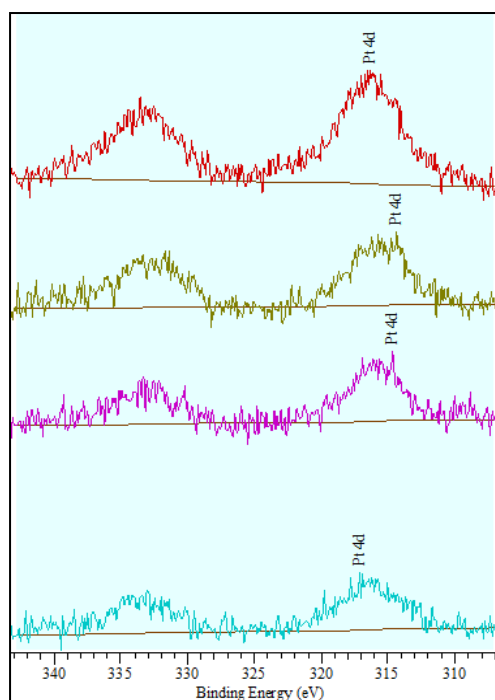
Figure.4b.6 Transmission electron microscopy analysis of (a) Pt-MA-0-Red450 and (b) Pt-MA-48-Red450 samples under a high resolution TEM

It is very evident from the TEM images that, the Pt particles size is more or less same in both the samples and indicating that if Pt NPs are the only decisive factor for nitrite hydrogenation, then both the above samples are expected to give similar catalytic activity and selectivity. Further, checking the surface composition of Pt NPs in all these catalysts are done to understand any effective change that the soft ageing treatment results in the stabilisation of the Pt NPs during impregnation by using x-ray photoelectron analysis studies.

4b.3.1e. X-ray photoelectron spectroscopy analysis of Pt-MA-X samples

The metallic nature of the Pt NPs on the alumina support is identified by the XPS analysis. Due to the overlapping between Pt 4f and Al 2p photopeaks, Pt 4d photopeak as core level is selected to examine the Pt-MA series under the photoelectron spectrometer throughout the study. All samples showed a 4d binding energy ranging between 315.4 to 315.9 eV indicating the existence of preferentially Pt²⁺ on the surface, which is shown in Figure 4b.7. Further the Pt⁰/Pt²⁺ surface composition also elucidated from the XPS analysis and is found that Pt²⁺

composition is more when compared to Pt⁰ on the surface (Table.4b.2). It will be most likely due to the storage of the exsitu reduced samples under ambient conditions before the XPS analysis. At this point it will be worth noting that before the actual catalytic test these materials will be reduced insitu under pure hydrogen and therefore the surface Pt²⁺ species which is observed in XPS measurements may not be crucial in defining the catalytic activity of our samples.



Catalysts	Relative surface composition	
	Pt ⁰	Pt ²⁺
Pt-MA0	29	71
Pt-MA24	42	58
Pt-MA36	41	59
Pt-MA48	30	70

Table 4b.2 Relative surface composition of Pt species on amorphous alumina

Figure.4b.7. X-ray photoelectron spectroscopic data for the MA-X samples reduced exsitu before the analysis at 450 °C

4b.3.1f. Temperature programmed reduction (TPR) analysis:-

Hydrogen temperature-programmed reduction (H₂-TPR) and Hydrogen chemisorption were carried out in a Micromeritics Autochem II 2920 apparatus (5 vol.% H₂/Ar). Typically, the sample (100 mg) was treated in flowing Ar at 150°C for 1 hour. After cooling in flowing Ar the H₂-TPR measurement was performed in 5 vol.% H₂/Ar (50 mL min⁻¹) up to a temperature of 450°C (5°C min⁻¹). The TPR profile for all the Pt supported alumina samples is represented in Figure.4b.8 and is self explanatory that two H₂ consumption domains are there for Pt species deposited on alumina.

The lower temperature reduction peak corresponds to the weakly anchored Pt and the high temperature domain for strongly anchored Pt species on these solvothermally treated alumina support. Further, the TPR profile supports the reduction temperature (450 °C) chosen for the current study; so that all the available Pt species will be completely reduced to metallic state during reduction and will theoretically act as active phase for catalytic reduction of nitrites using molecular hydrogen as reductant.

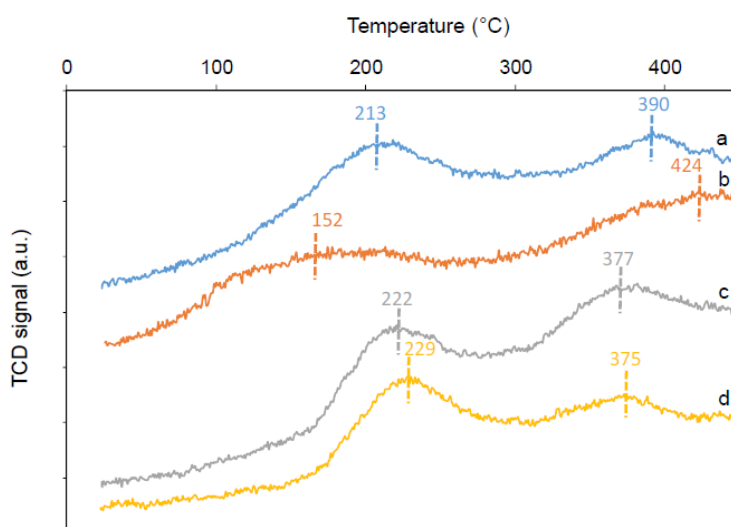


Figure.4b.8 Temperature programmed reduction (TPD) profile for various Pt/alumina samples

4b.3.1g. Chemisorption analysis results

The chemisorption analysis results gave a fairly descent dispersion for the Pt nanoparticles on the surface of the various amorphous alumina samples synthesised by soft ageing treatment. The dispersion range varies from 29% to 33% on different supported alumina catalyst. A correlation of the H/Pt ratio obtained from chemisorption with other structural characterisation is represented in Table.4b.3

H₂-chemisorption protocol:

The sample (100 mg) is in-situ reduced at 450°C under pure hydrogen (30 mL/min) during one hour. After degassing in flowing Ar at 400°C during one hour, the sample is cooled at ambient temperature. A series of pulses (5% H₂/Ar corresponding to 20 μL) is performed on the sample at ambient temperature until saturation

4b.3.1h Catalytic test results:-

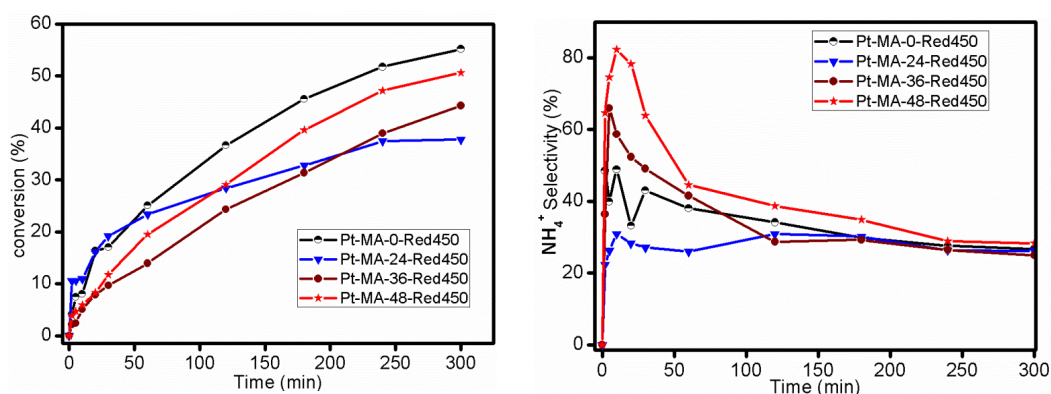


Figure.4b.9. Catalytic activity test results of Pt impregnated and reduced macroporous (MA-X) alumina samples

The Pt-MA-0 and Pt-MA-24 samples with larger macro structure ordering exhibited higher conversion of nitrites with lesser ammonia selectivity when compared to the other counterparts (Figure.4b.9). The larger ammonia selectivity in the case of Pt-MA-48-Red450 can be due to the complete loss of the macroporous nature and thereby an increase in the diffusion resistance in the pore network/ at the vicinity of the active metal nanoparticle centres. Literature results claims the formation of larger extent of undesired product ammonia when the local pH is alkaline near the active centres, such an enhanced local alkaline pH can be expected in our MA-48 system with lesser macroporous network.³⁵ A steady increase in the conversion along with a decrease in ammonia selectivity can be observed in our experimental conditions; it should be noted that the overall reaction is carried out in the absence of any buffering agent, generally used to maintain a neutral pH and improve the selectivity towards nitrogen. Therefore, the observe trend in similar ammonia selectivity for all the supported catalysts after 240 minutes can be considered to be due to the presence of the excess basicity in the reaction vessel developed by the formation of OH⁻ ions during the catalytic hydrogenation of nitrites. The conversion and ammonia selectivity shown here is a direct evidence for the resistance free mass transfer of the reactants and the products during catalysis in our hierarchically macroporous mesoporous alumina based material MA-0 as well as MA-24. The turnover frequency shown by all these Pt/alumina catalysts is represented in Table.4b.3

Table.4b.3 Turnover frequency represented in terms of Pt surface composition and particle size

Catalyst reduced at 450°C	Binding Energy (eV)	Pt/Al ratio	Bulk comp. (wt.%Pt)	H/Pt ratio	Pt particle size from TEM	r_0 (mol/h/g)	TOF (min^{-1})
Pt-MA-0	315.9	0.017	0.96	0.33	0.9-1.5	$2.20 \cdot 10^{-2}$	24.6
Pt-MA-24	315.4	0.016	0.94	0.29	0.6-1.3	$2.24 \cdot 10^{-2}$	23.8
Pt-MA-36	315.5	0.012	0.97	0.37	0.7-1.1	$0.93 \cdot 10^{-2}$	8.4
Pt-MA-48	315.9	0.009	0.92	0.29	0.8-1.5	$0.80 \cdot 10^{-2}$	7.8

4b.3.2. Hierarchical macroporous-mesoporous alumina (MMA-X) synthesised by soft ageing treatment method and its catalytic activity

4b.3.2a. Thermogravimetry analysis and XRD analysis of the macroporous-mesoporous alumina (MMA-X)

The TGA and DTG of the samples after the soft ageing treatment under 80 °C for different time intervals look similar to that of the simple MMA-0 sample where no such treatment was done during the synthesis/ageing stage. A representative TGA/DTG graph is represented in Figure.4b.10a.

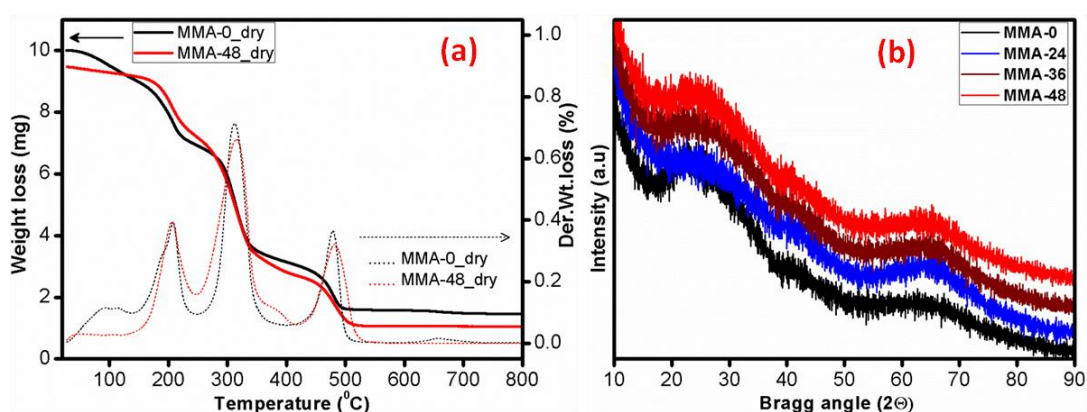


Figure.4b.10. TGA/DTG analysis of the soft ageing treated and non treated sample(a) and the wide angle x-ray diffraction (b) of the series of the samples MMA-X, where X-is the soft ageing treatment time

Further, the amorphous nature of all the synthesised samples even after high temperature calcination is evident from the wide angle x-ray diffraction analysis shown in Figure.4b.10b. Similarly the Pt incorporated samples also showed x-ray amorphous nature and like the macroporous alumina system discussed in the previous section, here also no visible signature for the presence of Pt NPs in the system is observed in the wide angle x-ray analysis. The Pt impregnated, calcined and reduced samples x-ray analysis data is represented in Figure.4b.11.

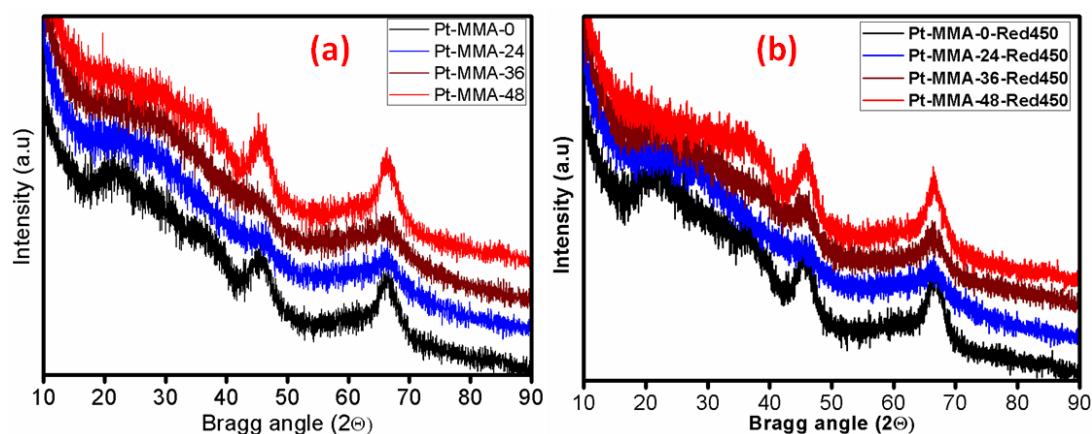


Figure.4b.11 The wide angle x-ray diffraction analysis of (a) 1wt% Pt impregnated and calcined and (b) Pt impregnated, calcined and reduced at 450 °C MMA-X samples (were X-soft ageing treatment time)

Form Figure.4b.11. it is very clear that the mesoporous macroporous alumina had under gone some structural transformation after impregnation since some of the aluminium oxyhydroxide features are present in the XRD spectra. Yet, there is complete absence of the Pt diffraction throughout the analysis range indirectly pointing to the better dispersion as well as the smaller crystallites of Pt NPs on the amorphous alumina support.

4b.3.2b. Surface area analysis of the Pt/MMA-X samples

All the supported catalysts showed Type IV isotherm with H₂ hysteresis loop.

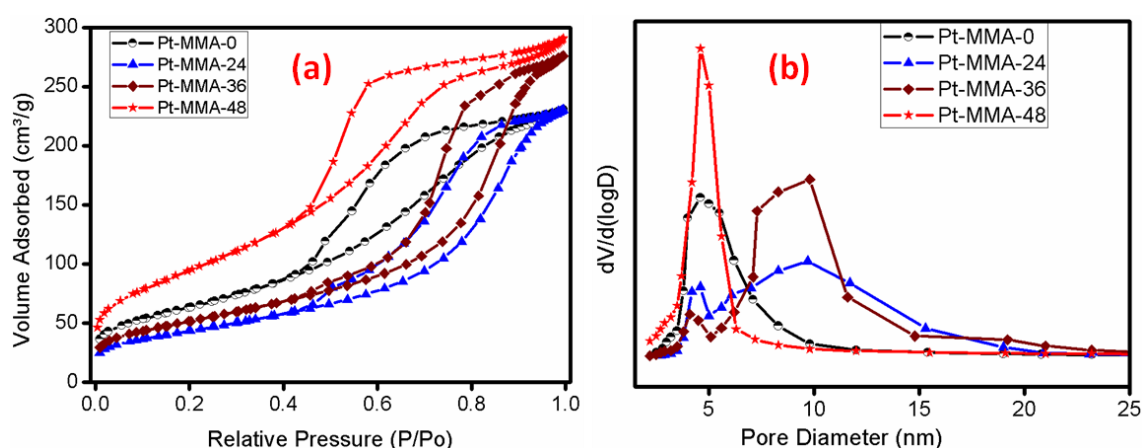


Figure.4b.12 The surface area (a) and pore size distribution (b) analysis data for the various Pt/MMA-X samples

It is very evident from the surface area analysis (Figure.4b.12) that the soft ageing treatment during the support synthesis has resulted in multimodal pore systems; it can be based on the interpenetration of the PS300 beads during the soft ageing treatment and can be explained as the same mechanism as that of the MA-X series. A close observation of the textural analysis data reveals the presence of large windows of approx 50 nm in the case of Pt-MMA-0 and Pt-MMA-24, whereas such large windows are missing in both Pt-MMA-36 and Pt-MMA-48. One could see that substantially large mesopores of size 10 nm is predominating in the Pt-MMA-36 sample at the expense of smaller mesopores and larger windows; a similar observation can be obtained from the Pt-MMA-48 sample also.

4b.3.2c. Catalytic Test Results

The applicability of the synthesised Pt/MMA-X samples as a catalyst is tested for the hydrogenation of nitrites and is found that the selectivity towards the most desired product dinitrogen is influence by the textural property of the support like the Pt-MA-X samples discussed in the previous section.

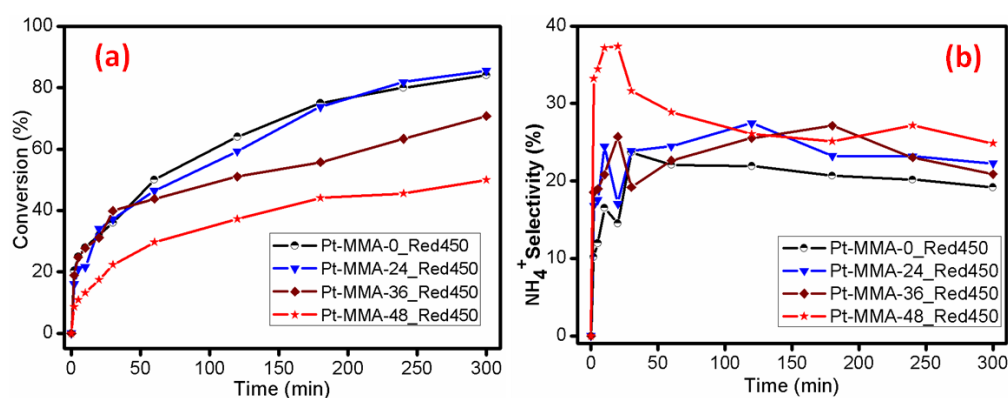


Figure.4b.13 Catalytic test results of various Pt-MMA-X samples (a) conversion and (b) ammonia selectivity at room temperature under 1 Bar hydrogen pressure (X- soft ageing treatment time)

When compared the activity as well as selectivity of the material towards the nitrite hydrogenation it is clearly visible from Figure.4b.13 that the conversion decreased as the soft ageing treatment (SAT) time of the support alumina increased. It will be worth mentioning at this point that From Pt-MMA-0 to Pt-MMA-36 samples, there is the presence of larger windows or mesopores evident from the surface area analysis, the conversion rate is almost similar in the initial 1 hour indicating the significance of interconnected pore networks in this

kind of diffusion limited reactions. Further, the ammonia selectivity in the initial period of the reaction is also influenced by the pore system by considering that all other parameters like particle size, oxidation state and dispersion remains more or less same (like the Pt-MA-X case) for the active Pt NPs in all the materials compared for this part of the study. The almost similar ammonia selectivity towards the end of the reaction can be attributed to the increase in the pH of the medium during the course of the reaction as since the entire reaction is carried out in the absence of any buffering agent (final pH=11).

4.2. Conclusions

Alumina with tunable pore size and hierarchical structure has been synthesised by utilising evaporation induced self assembly strategy as well as soft ageing treatment (SAT) methodology in a templated synthesis protocol. The complete characterisation of these materials showed variable porosity starting from well ordered mesoporosity (PMA-650), Macroporosity (MA-650) and co-existence of macroporous-mesoporous (MMA-650) in nature. From the surface area analysis as well as the high resolution scanning electron microscopy revealed the presence of large macroporous windows interconnected with mesopores in a single hard templated synthesised MA-0 sample. On Pt impregnation, all these materials showed nitrite hydrogenation capability under room temperature conditions. Yet, the selectivity towards the most desirable product dinitrogen gas is largely dependent on the surface/textural property of the support material in our current study. As discussed in section.4a, it is very evident that the co-operative assembly of interconnected mesoporosity with macroporosity could effectively tune the catalytic activity towards nitrogen with a selectivity of 85% within the first 30 minutes of the reaction in our Pt-MMA catalyst when compared to the macroporous (Pt-MA) and the mesoporous (Pt-PMA) counterpart. There was a two fold increase in the overall catalytic activity of the Pt-MMA catalyst even though no buffering agents were used in the current study. Our experimental data gives direct evidences for the influence of the textural property of the heterogeneous support in tuning the activity/selectivity of any chemical reaction, specifically catalytic hydrogenation of nitrites in the present case.

The results and discussions from Section.4b directly points to the importance of synthesis methodology in deciding the final catalytic activity of a heterogeneous catalyst. From the data, one could clearly see the improvement in surface morphology in terms of the surface area and pore size on introducing soft ageing treatment (SAT) into the EISA strategy. Further, the complete characterisation of the Pt-MA series catalysts, showing similar particle

size, almost equal dispersion and identical chemical state directly helps us to correlate the observed catalytic activity with the textural property of the support used, namely macroporous alumina. It is evident in the case of Pt-MA-0 and Pt-MA-24 in the surface area analysis results that this two material contains interconnected large mesopores and small mesopores when compared to the perfectly mesoporous Pt-MA-36 and Pt-MA-48 sample, even though our synthesis protocol involves a single hard template (PS-300 beads, 300 nm sized spherical polystyrene beads). The fundamental question about the role of support in catalysis other than the primary role of acting as heterogeneous support is dealt here without changing the surface functionality in alumina. Yet, a fine tuning in the alumina support resulted in drastic change in the catalytic activity regardless of Pt being the active phase in all Pt-MA catalysts. Similar observations can be seen in our Pt supported on alumina (Pt-MMA) catalysts synthesised through soft ageing treatment (SAT) also. In this case the purposeful introduction of mesoporosity along with macroporosity by applying dual templating synthesis protocol helps in avoiding mass transfer limitations during actual catalysis. This will ultimately enhance the in and out supply of the reactants and product in the local environment of the Pt NPs. The results drawn from our studies can help in designing new functional catalysts for catalytic reaction under industrially challenging conditions using stable and porous support materials.

4.3. References:-

1. K. M. Thomas, *Catalysis Today*, 2007, **120**, 389-398.
2. P. Nugent, Y. Belmabkhout, S. D. Burd, A. J. Cairns, R. Luebke, K. Forrest, T. Pham, S. Ma, B. Space, L. Wojtas, M. Eddaoudi and M. J. Zaworotko, *Nature*, 2013, **495**, 80-84.
3. S. J. Yang, T. Kim, J. H. Im, Y. S. Kim, K. Lee, H. Jung and C. R. Park, *Chemistry of Materials*, 2012, **24**, 464-470.
4. X. S. Zhao, X. Y. Bao, W. Guo and F. Y. Lee, *Materials Today*, 2006, **9**, 32-39.
5. S. Wannakao, T. Maihom, M. Probst, J. Limtrakul and K. Kongpatpanich, *The Journal of Physical Chemistry C*, 2016, **120**, 19686-19697.
6. R. Takahashi, S. Sato, T. Sodesawa and M. Yabuki, *Journal of Catalysis*, 2001, **200**, 197-202.
7. M. Vallet-Regí, F. Balas and D. Arcos, *Angewandte Chemie International Edition*, 2007, **46**, 7548-7558.
8. P. Horcajada, C. Serre, M. Vallet-Regí, M. Sebban, F. Taulelle and G. Férey, *Angewandte Chemie*, 2006, **118**, 6120-6124.
9. J.-F. Chen, H.-M. Ding, J.-X. Wang and L. Shao, *Biomaterials*, 2004, **25**, 723-727.
10. P. Horcajada, A. Rámila, J. Pérez-Pariente, R. Vallet, amp, x and M., *Microporous and Mesoporous Materials*, 2004, **68**, 105-109.
11. P. Horcajada, T. Chalati, C. Serre, B. Gillet, C. Sebrie, T. Baati, J. F. Eubank, D. Heurtaux, P. Clayette, C. Kreuz, J.-S. Chang, Y. K. Hwang, V. Marsaud, P.-N. Bories, L. Cynober, S. Gil, G. Férey, P. Couvreur and R. Gref, *Nat Mater*, 2010, **9**, 172-178.
12. L. L. Beecroft and C. K. Ober, *Chemistry of Materials*, 1997, **9**, 1302-1317.
13. B. J. Scott, G. Wirnsberger and G. D. Stucky, *Chemistry of Materials*, 2001, **13**, 3140-3150.
14. Q. Yao, A. Bermejo Gómez, J. Su, V. Pascanu, Y. Yun, H. Zheng, H. Chen, L. Liu, H. N. Abdelhamid, B. Martín-Matute and X. Zou, *Chemistry of Materials*, 2015, **27**, 5332-5339.
15. J. W. Kemling, A. J. Qavi, R. C. Bailey and K. S. Suslick, *The Journal of Physical Chemistry Letters*, 2011, **2**, 2934-2944.
16. J. Lee, S. Yoon, T. Hyeon, S. M. Oh and K. Bum Kim, *Chemical Communications*, 1999, 2177-2178.
17. D.-W. Wang, F. Li, M. Liu, G. Q. Lu and H.-M. Cheng, *Angewandte Chemie*, 2008, **120**, 379-382.
18. S. Han, D. Wu, S. Li, F. Zhang and X. Feng, *Advanced Materials*, 2014, **26**, 849-864.
19. C. Largeot, C. Portet, J. Chmiola, P.-L. Taberna, Y. Gogotsi and P. Simon, *Journal of the American Chemical Society*, 2008, **130**, 2730-2731.
20. R. Prins, V. H. J. De Beer and G. A. Somorjai, *Catalysis Reviews*, 1989, **31**, 1-41.
21. C. Márquez-Alvarez, N. Žilková, J. Pérez-Pariente and J. Čejka, *Catalysis Reviews*, 2008, **50**, 222-286.
22. N. Bejenaru, C. Lancelot, P. Blanchard, C. Lamonier, L. Rouleau, E. Payen, F. Dumeignil and S. Royer, *Chemistry of Materials*, 2009, **21**, 522-533.
23. H. Liu, G. Lu, Y. Guo, Y. Wang and Y. Guo, *Catalysis Communications*, 2009, **10**, 1324-1329.
24. WHO Guidelines for Drinking water, *Fourth Edition*, 2011, http://www.who.int/water_sanitation_health/publications/2011/dwq_guidelines/en/.

25. A. Kapoor and T. Viraraghavan, *Journal of Environmental Engineering*, 1997, **123**, 371-380.
26. S. Hörold, K. D. Vorlop, T. Tacke and M. Sell, *Catalysis Today*, 1993, **17**, 21-30.
27. N. Barrabés and J. Sá, *Applied Catalysis B: Environmental*, 2011, **104**, 1-5.
28. U. Prüsse, M. Hähnlein, J. Daum and K.-D. Vorlop, *Catalysis Today*, 2000, **55**, 79-90.
29. U. Prüsse and K.-D. Vorlop, *Journal of Molecular Catalysis A: Chemical*, 2001, **173**, 313-328.
30. M. Al Bahri, L. Calvo, M. A. Gilarranz, J. J. Rodriguez and F. Epron, *Applied Catalysis B: Environmental*, 2013, **138–139**, 141-148.
31. J. K. Chinthaginjala, A. Villa, D. S. Su, B. L. Mojet and L. Lefferts, *Catalysis Today*, 2012, **183**, 119-123.
32. N. Jarrah, J. G. van Ommen and L. Lefferts, *Catalysis Today*, 2003, **79–80**, 29-33.
33. H. C. Aran, J. K. Chinthaginjala, R. Groote, T. Roelofs, L. Lefferts, M. Wessling and R. G. H. Lammertink, *Chemical Engineering Journal*, 2011, **169**, 239-246.
34. G. Wang, E. Johannessen, C. R. Kleijn, S. W. de Leeuw and M.-O. Coppens, *Chemical Engineering Science*, 2007, **62**, 5110-5116.
35. M. D'Arino, F. Pinna and G. Strukul, *Applied Catalysis B: Environmental*, 2004, **53**, 161-168.
36. J. K. Chinthaginjala, J. H. Bitter and L. Lefferts, *Applied Catalysis A: General*, 2010, **383**, 24-32.
37. C. T. Kresge, M. E. Leonowicz, W. J. Roth, J. C. Vartuli and J. S. Beck, *Nature*, 1992, **359**, 710-712.
38. A. Imhof and D. J. Pine, *Nature*, 1997, **389**, 948-951.
39. C. M. A. Parlett, K. Wilson and A. F. Lee, *Chemical Society Reviews*, 2013, **42**, 3876-3893.
40. J. Dhainaut, J.-P. Dacquin, A. F. Lee and K. Wilson, *Green Chemistry*, 2010, **12**, 296-303.
41. C. M. A. Parlett, P. Keshwala, S. G. Wainwright, D. W. Bruce, N. S. Hondow, K. Wilson and A. F. Lee, *ACS Catalysis*, 2013, **3**, 2122-2129.
42. Y. Tokudome, K. Fujita, K. Nakanishi, K. Miura and K. Hirao, *Chemistry of Materials*, 2007, **19**, 3393-3398.
43. K. Niesz, P. Yang and G. A. Somorjai, *Chemical Communications*, 2005, 1986-1987.
44. M. Nguefack, A. F. Popa, S. Rossignol and C. Kappenstein, *Physical Chemistry Chemical Physics*, 2003, **5**, 4279-4289.
45. W. L. Suchanek, *Journal of the American Ceramic Society*, 2010, **93**, 399-412.
46. Y. Li, C. Peng, L. Li and P. Rao, *Journal of the American Ceramic Society*, 2014, **97**, 35-39.
47. S. Ghosh, P. Bose, S. Basak and M. K. Naskar, *Journal of Asian Ceramic Societies*, 2015, **3**, 198-205.
48. B. T. Holland, C. F. Blanford, T. Do and A. Stein, *Chemistry of Materials*, 1999, **11**, 795-805.
49. W. Cai, J. Yu, C. Anand, A. Vinu and M. Jaroniec, *Chemistry of Materials*, 2011, **23**, 1147-1157.
50. L.-L. Li, W.-T. Duan, Q. Yuan, Z.-X. Li, H.-H. Duan and C.-H. Yan, *Chemical Communications*, 2009, 6174-6176.
51. J.-P. Dacquin, J. Dhainaut, D. Duprez, S. Royer, A. F. Lee and K. Wilson, *Journal of the American Chemical Society*, 2009, **131**, 12896-12897.
52. R. Hamtil, N. Žilková, H. Balcar and J. Čejka, *Applied Catalysis A: General*, 2006, **302**, 193-200.

53. P. Schmidt-Winkel, W. W. Lukens, P. Yang, D. I. Margolese, J. S. Lettow, J. Y. Ying and G. D. Stucky, *Chemistry of Materials*, 2000, **12**, 686-696.
54. J. Fan, C. Yu, L. Wang, B. Tu, D. Zhao, Y. Sakamoto and O. Terasaki, *Journal of the American Chemical Society*, 2001, **123**, 12113-12114.
55. Q. Wu, F. Zhang, J. Yang, Q. Li, B. Tu and D. Zhao, *Microporous and Mesoporous Materials*, 2011, **143**, 406-412.
56. Y. Li, J. Su, J. Ma, F. Yu and R. Li, *Materials Letters*, 2015, **153**, 165-167.
57. S. D. Ebbesen, B. L. Mojet and L. Lefferts, *The Journal of Physical Chemistry C*, 2011, **115**, 1186-1194.
58. G. Leofanti, M. Padovan, G. Tozzola and B. Venturelli, *Catalysis Today*, 1998, **41**, 207-219.
59. X. Liu, Y. Guo, W. Xu, Y. Wang, X. Gong, Y. Guo, Y. Guo and G. Lu, *Kinetics and Catalysis*, 2011, **52**, 817-822.
60. G. S. Grader, G. E. Shter, D. Avnir, H. Frenkel, D. Sclar and A. Dolev, *Journal of Sol-Gel Science and Technology*, 2001, **21**, 157-165.

Chapter 5

Summary and Conclusions

Engineering materials in various active forms like powders, nanostructures and composite thin films with well defined physical and chemical properties are the prime focus of the modern day heterogeneous catalyst synthesis. Composite bulk materials are well known for their applicability as catalysts in heterogeneous catalysis from centuries. The optimum activity is primarily bound to the availability and accessibility of the active sites as well as the heat and mass transfer properties of the material. Hence engineering catalytically relevant materials with better diffusion properties have interested the catalytic fraternity for the last few decades. Similarly one of the prime advantages of the heterogeneous catalysis, the so called recyclability of the catalyst also depends on the stability of the materials under reaction conditions. Hence efforts are devoted towards engineering catalytically relevant materials with high thermal stability, improved functionalities (Au@silica nanostructures) and better diffusion property (Pt-hierarchical alumina) have been engineered and utilised under challenging reaction conditions. This thesis work took efforts to minimise the material gap existing in insitu surface science studies by developing composite Au@silica composite thin films. The major conclusions drawn out of the basic observations are summarised as;

Chapter.1: This chapter explores the status of the heterogeneous catalysis in Au@silica catalysts in the environmentally significant CO oxidation reaction as well as hierarchical Pt-alumina systems in liquid phase reactions. The fundamentals of heterogeneous catalysis and nanocatalysis are detailed here. Starting from the nomenclature to the various synthesis methods for the porous materials is elaborated. The basics, the significance of the reactions carried out and the material properties are portrayed with the help of ample literature references. Furthermore the various instruments and techniques used in the present thesis are also mentioned clearly.

Chapter.2: A detailed understanding of the gold catalysis in environmentally significant CO oxidation reaction is demonstrated here by using different Au@silica morphologies. The well accepted concept of anchoring metal nanoparticles inside the porous support, in this case Au@meso-silica is synthesised by utilising the dual functionality of P123 and its CO oxidation capability is tested and reported in chapter.2a. Further to improve the catalytic stability Au@silica core shell morphology has been designed with gold core of 8-12 nm with a highly porous silica shell. The exceptional CO oxidation capability shown by this core shell material has points to the fact that “size dependency” is not the only important reason for catalytic activity in CO oxidation on a Au@silica catalyst (chapter.2b). Additionally efforts have been taken to bring down the onset CO oxidation temperature by incorporating “Ti” in

the Au@silica matrix. By tuning the synthesis condition resulted in the formation of Au@Ti-Silica catalyst which showed remarkable CO oxidation capability with room temperature activity with 100% conversion at 160 °C. The sinter resistance capability of the Au@Ti-Silica is also demonstrated by characterising the spent catalyst (chapter.2c). A careful observation of the discussion in this chapter will help us to understand the bigger nanoparticles of size 8-12 nm well above the optimum size range is able to show a better catalytic activity for CO oxidation reaction in the core shell Au@silica system (chapter 2b) when compared with the ultra small Au NPs deposited silica system discussed in chapter 2a. The presence of oxygen activation site in the porous silica sphere makes the Au@silica core shell catalysts superior to the previous catalyst. Further, the incorporation of the reducible Ti in the silica matrix increases the oxygen activation sites during the CO oxidation catalysis in the case of Au@Ti-SiO₂ catalyst discussed in chapter 2c. Hence on comparison of the three discussed catalysts, one can clearly see the significance of oxygen activation sites which make otherwise inert silica into an active support for Au NPs based CO oxidation reaction.

Chapter.3: By extending the synthesis protocol discussed in chapter 2a, Au-mesoSilica thin film composite catalyst has been synthesised utilising the dual functionality of P123 as structure directing agent as well as reducing agent. A careful optimisation of the synthesis methodology resulted in crack free thin films, which is demonstrated as a robust SERS substrate. The composite thin film material is applied as a catalyst in the P-nitrophenol reduction reaction monitored insitu under a Raman spectrophotometer. Such materials mimicking the real world catalysts are expected to reduce the material gap which currently exists in insitu surface science studies.

Chapter.4: Direct evidences for the influence of pore architecture in fine tuning the selectivity for a chemical reaction is derived and presented in this chapter; by taking Pt supported hierarchical alumina as an example in an environmentally significant denitrification reaction. Various pore morphologies have been engineered for the amorphous alumina support by fine tuning the synthesis procedure as well as varying the template from P123 to polystyrene beads. In the current chapter efforts have been taken to develop mesoporous, macroporous and macroporous mesoporous alumina by the Evaporation induced self assembly strategy (chapter.4a) and a soft ageing treatment coupled with EISA strategy (chapter.4b). The catalytically active Pt nanoparticles have been impregnated in a conventional wet impregnation method on to all the alumina support irrespective of its morphology. It has been observed that a co-operative assembly of macroporous and mesoporous network within the

Pt-alumina catalyst is necessary for improved nitrogen selectivity in the denitrification reaction (chapter.4a). Likewise the soft ageing treatment involved during the support alumina synthesis results in improved textural characteristic, yet poor nitrogen selectivity when attempted for the denitrification reaction using hydrogen gas as the reducing agent (chapter.4b). This result further indicates that the soft ageing treatment hampers the catalytic activity for the current reaction.

List of Publications

1. A. C. Sunil Sekhar* and C. P. Vinod*, Gold Incorporated Mesoporous Silica Thin Film Model Surface as a Robust SERS and Catalytically Active Substrate., *Molecules*, 2016, 21, 667(invited article for a special issue "Coinage Metal (Copper, Silver, and Gold) Catalysis)
2. A. C. Sunil Sekhar, K. V. Ziyad, Y. Soni and C. P. Vinod*, Activity Enhancement upon the Incorporation of Titanium: Au@Ti-SiO₂ Core-Shell Nanocatalysts for the CO Oxidation Reaction., *ChemCatChem*, 2015, 7 (7), 1222-1230
3. A. C. Sunil Sekhar, C. J. Meera, K. V. Ziyad, C. S. Gopinath and C. P. Vinod*, Synthesis and catalytic activity of monodisperse gold-mesoporous silica core-shell nanocatalysts., *Catalysis Science & Technology*, 2013, 3, 1190-1193
4. A. C. Sunil Sekhar, K. Sivaranjani, C. S. Gopinath* and C. P. Vinod*, A simple one pot synthesis of nano gold – mesoporous silica and its oxidation catalysis., *Catalysis Today*, 2012, 198, 92-97

Curriculum Vitae

Mr. Sunil Sekhar A C, son of Chandrasekharan Pillai and Anandakumari Amma, born on 10th May 1984 at the Kollam district, Kerala, India finished his formal schooling at St. Stephen's school, Pathanapuram. Following his Bachelor's degree in Chemistry from St. Stephen's College, Pathanapuram (2001-2004), he moved to St. Gregorious College, Kottarakkara for his Post Graduation Degree in Chemistry (2004-2006). The process of teaching/learning is further understood by him via completing his Bachelor of Education degree (2007) from the Mount Tabor Teachers Training College, Pathanapuram. He then worked as a Lecturer in an Engineering College, Bangalore (2007-2010). After qualifying the UGC-JRF for NET (2011), he joined for PhD program under the guidance of Dr. Vinod. C. Prabhakaran, Sr. Scientist, Catalysis and Inorganic Chemistry Division, CSIR-NCL, Pune. He has carried out his research work in the field of heterogeneous catalysis, focusing on the synthesis of composite porous materials, thin films and their application in industrially and environmentally significant reactions.